



VCU

Virginia Commonwealth University
VCU Scholars Compass

Theses and Dissertations


Graduate School

2016

Fabricating Superhydrophobic and Superoleophobic Surfaces with Multiscale Roughness Using Airbrush and Electrospray

Karam N. Almilaji

Follow this and additional works at: <https://scholarscompass.vcu.edu/etd>

 Part of the [Biological and Chemical Physics Commons](#), [Engineering Physics Commons](#), [Manufacturing Commons](#), [Materials Chemistry Commons](#), and the [Other Mechanical Engineering Commons](#)

© The Author

Downloaded from

<https://scholarscompass.vcu.edu/etd/4460>

This Thesis is brought to you for free and open access by the Graduate School at VCU Scholars Compass. It has been accepted for inclusion in Theses and Dissertations by an authorized administrator of VCU Scholars Compass. For more information, please contact libcompass@vcu.edu.

Copyright © 2016 Karam N. AL-Milaji. All Rights Reserved

**Fabricating Superhydrophobic and Superoleophobic Surfaces with Multiscale Roughness
Using Airbrush and Electrospray**

A thesis submitted in partial fulfillment of the requirements for the Degree of Master of Science
at Virginia Commonwealth University

By

Karam N. AL-Milaji

Director:

Dr. Hong Zhao

Assistant professor

Department of Mechanical and Nuclear Engineering

Virginia Commonwealth University

Richmond Virginia

August 2016

Acknowledgments

Thanks to Almighty God (ALLAH) for his great mercy and accommodation that empowered me to get this work accomplished.

No words can adequately express my sincere gratitude to my advisor Dr. Hong Zhao for her continuous support, guidance, patience, and encouragement. I will always remain grateful for all the dedication and effort she offered throughout this work. My respect for her will always be in my heart.

Besides my Advisor, I would like to thank my committee members Dr. Daren Chen and Dr. Christina Tang not only for their insightful comments and encouragement, but also for the hard questions that motivated me to widen my research area from various perspectives.

I am deeply indebted to Dr. Dmitry Pestov and Dr. Carlos Castano for their useful guidances, precious instructions, and valuable trainings I needed to pursue my degree.

I owe special thanks to our graduate program director Dr. Karla M. Mossi, I warmly appreciate her encouragement and her wonderful support. I am also thankful to my lab mate, Charles Stacy, for his help that enabled me to confront many challenges during this endeavor.

More importantly, a special thanks to the Higher Committee of Educational Development in Iraq (HCED) for their financial support and cooperation that assisted me to chase my dream in the United States.

Last but not least, none of this would have been to succeed without the constant source of love, patience, support, and motivation of my wonderful parents, brother, wife, and daughters.

Table of Contents

Acknowledgments	ii
Table of Contents	iii
Table of Figures	vi
List of Tables	xii
Abstract	xiii
CHAPTER 1 Introduction	1
1.1 Introduction	1
1.2 Motivation	4
1.2.1 Superhydrophobic (SHP) surfaces	4
1.2.2 Superoleophobic (SOP) surfaces	5
1.3 Objectives	6
1.4 Outline	6
CHAPTER 2 Literature Review	8
2.1 Superhydrophobic surfaces	8
2.2 The origin of superoleophobicity	9
2.3 Fabrication of superhydrophobic and superoleophobic with random surfaces roughness..	12
2.3.1 Electrospinning and electrospray	12
2.3.2 Spray coating	15

2.3.3 Layer by layer deposition	16
2.4 Fabrication of superhydrophobic and superoleophobic with regular textured surfaces.....	18
CHAPTER 3 Fabricating Superhydrophobic and Superoleophobic Surfaces Using	
Airbrush.....	21
3.1 Introduction to airbrushing.....	21
3.2 Materials and methods to fabricate textured surfaces	22
3.3 Contact angle measurements and surface morphology characterization	25
3.4 Results and discussion.....	26
3.4.1 Effect of silicon dioxide concentration on surface morphology and wettability.....	26
3.4.2 Effect of silicon dioxide agglomerate particle size on surface wettability.....	32
3.4.3 Surface transparency.....	36
3.5 Conclusion.....	38
CHAPTER 4 Superhydrophobic and Superoleophobic Surfaces by Mask-assisted	
Electrospray.....	39
4.1 Introduction	39
4.2 Material and methods	40
4.2.1 Apparatus setup	40
4.2.2 Materials and textured surface fabrication	41
4.2.3 Contact angle measurements and surface morphology characterization.....	44
4.3 Results and discussion.....	45

4.3.1 Superhydrophobic and superoleophobic surfaces with random hierarchical roughness	45
4.3.2 Superhydrophobic and superoleophobic surfaces with patterned multiscale roughness	54
4.4 Conclusion	62
CHAPTER 5 Modeling of Textured Surface Formation in Mask-assisted Electrospray	63
5.1 Introduction	63
5.2 Simulation domains and mesh geometry	63
5.3 Electric field and charged particle dynamics	65
5.4 Simulation of the electric field	68
5.5 Simulation of the trajectory of charged particles	71
5.6 Conclusion	76
CHAPTER 6 Concluding Remarks	77
6.1 Review of results and conclusions	77
6.2 Comparison of air spray and electrospray	78
6.3 Modeling of mask-assisted electrospray deposition	79
6.4 Future works	81
References	84
Appendix A: Modeling Instructions	96
Appendix B: Vita	119

Table of Figures

Figure 1.1: Wetting behavior of a droplet on solid substrates: (a) liquid droplet on a smooth surface, (b) Wenzel state, (c) Cassie-Baxter state.....	2
Figure 1.2: (a) a 5 μL water droplet tilted at 45°, (b) an illustration of tilting angle.....	3
Figure 1.3: (a) advancing contact angle during contact line advancing, (b) receding contact angle during contact line receding.	3
Figure 2.1: Dual surface roughness of lotus leaves: (a) lotus leaf microstructure, (b) nanostructure of lotus leaves.....	9
Figure 2.2: (a) and (b) SEM pictures of electrospun mat, (c) the alignment illustration of electrospun mat, (d) Cassie-Baxter state provided by re-entrant structure, (e) liquid sagging due to an external applied pressure	10
Figure 2.3: (a) an illustration of formation of liquid-solid-vapor interface of textured surface with re-entrant structure, (b), (c), and (d) SEM images of the fabricated re-entrant structures.....	11
Figure 2.4: (a) SEM image of the wavy side wall pillars, (b) SEM image of the overhang structured pillars.....	11
Figure 2.5: (a) schematic of the overhang structure, (b), and (c) SEM images of the fabricated overhang structure.....	12
Figure 2.6: (a) electrospun micro-beads, (b) electrospun beads-on-strings.....	13
Figure 2.7: (a) electrospray deposition steps of SiO_2 layer with Au nanoparticles producing micro-nano hierarchical structure, (b) high water contact angle after fluorinating the sample	14

Figure 2.8: (a) and (b) SEM pictures of hierarchical textured surface with micro-nanoroughness.....	16
Figure 2.9: An illustration scheme layer by layer deposition.....	17
Figure 2.10: A modified scheme of layer by layer deposition.....	18
Figure 2.11: SEM images of different pillar geometries produced via photolithography.....	19
Figure 2.12: Groove patterning fabricated by Zhao <i>et al</i>	20
Figure 3.1: A schematic of coating procedure.....	22
Figure 3.2: A schematic of spray coating	23
Figure 3.3: Particle size measurement of a SiO ₂ suspension (15 mg/mL) by dynamic light scattering	24
Figure 3.4: SEM images of textured surfaces fabricated with different SiO ₂ concentrations: (a) 8 mg/mL, (b) 15 mg/mL, and (c) 25 mg/mL.....	26
Figure 3.5: Roughness of surfaces fabricated with different SiO ₂ concentrations.....	27
Figure 3.6: LSM 3D images of textured surfaces fabricated with different SiO ₂ concentrations: (a) 8 mg/mL, (b) 15 mg/mL, and (c) 25 mg/mL. Each picture was constructed of at least 360 slices, 1 interval, and 375 μm range	27
Figure 3.7: AFM 3D images of textured surfaces fabricated with different SiO ₂ concentrations: (a) 8 mg/mL, (b) 15 mg/mL, and (c) 25 mg/mL	28
Figure 3.8: (a) apparent contact angles of samples fabricated with different SiO ₂ concentrations, (b) sliding angles of samples fabricated with different SiO ₂ concentrations	29
Figure 3.9: Effect of surface roughness on surface wettability for samples fabricated with different SiO ₂ concentrations	32

Figure 3.10: Agglomerate particle size comparison between the directly-dispersed and surfactant-dispersed suspensions	33
Figure 3.11: SEM images of textured surfaces fabricated with (a) directly-dispersed and (b) surfactant-dispersed suspensions	34
Figure 3.12: Contact angle measurements of textured surfaces fabricated with directly-dispersed and surfactant-dispersed suspensions.	35
Figure 3.13: Sliding angle measurements of textured surfaces fabricated with directly-dispersed and surfactant-dispersed suspensions.	35
Figure 3.14: Cross-section of textured surfaces fabricated with different SiO ₂ concentration: (a) 8 mg/mL, (b) 15 mg/mL, (c) 25 mg/mL.....	37
Figure 3.15: Transparency of textured surfaces fabricated with different SiO ₂ concentrations.	37
Figure 4.1: A schematic of the electrospray experimental setup.....	40
Figure 4.2: Operating window (stable cone-jet region) along with different electrospray modes.	42
Figure 4.3: Electrospray scheme: (a) surfaces with random hierarchical roughness, (b) surfaces with Patterned multiscale roughness.....	42
Figure 4.4: Particle size measurement of a SiO ₂ suspension (15 mg/mL) by dynamic light scattering.....	45
Figure 4.5: SEM images of textured surfaces with hierarchical roughness fabricated at different spray times: (a) and (b) 2 min spray time, (c) and (d) 5 min spray time, (e) and (f) 45 min, (g) and (h) 90 min spray time.	46

Figure 4.6: Roughness of surface with hierarchical multiscale structure fabricated at various electro spray times	47
Figure 4.7: LSM 3D images of samples with random hierarchical roughness sprayed at various spray times: (a) 5 min, (b) 45 min, (c) 90 min.	48
Figure 4.8: AFM 3D images for measuring the nanoscale roughness of silica agglomerates using samples coated with 5, 45, 90 min electro spray time.....	49
Figure 4.9: A schematic of the re-entrant and overhang structures	51
Figure 4.10: SEM images of samples with random hierarchical roughness. (a) Sample fabricated at 2 min spray time. (b) Sample fabricated at 90 min	51
Figure 4.11: (a) Contact angle of 3 μ L DI water droplet using ellipse fitting, (b) Contact angle of 3 μ L DI water droplet using Young-Laplace fitting, (c) Contact angle of 3 μ L hexadecane droplet using ellipse fitting, (d) Contact angle of 3 μ L hexadecane droplet using Young-Laplace fitting	53
Figure 4.12: PTFE coated stainless steel mesh.....	55
Figure 4.13: Shows SEM images of the fabricated pillars using different mesh gaps ranging from 70 to 500 μ m, before addition of the second SiO ₂ layers. The images were taken with 45° tilting angle	55
Figure 4.14: (a) micro-pillars fabricated using 70 μ m gap, (b) micro-pillars fabricated using 140 μ m gap, (c) micro-pillars fabricated using 250 μ m gap, (d) micro-pillars fabricated using 500 μ m gap.....	56
Figure 4.15: LSM 3D images of patterned samples with multiscale roughness fabricated using different mesh gaps: (a) 70 μ m, (b) 140 μ m, (c) 250 μ m, (d) 500 μ m	58

- Figure 4.16:** Pillars' average height of patterned samples with multiscale roughness fabricated using different mesh gaps: (a) 70 μm , (b) 140 μm , (c) 250 μm , (d) 500 μm 58
- Figure 4.17:** (a) pillar patterns by which the solid area fraction is reduced. (b) SEM picture of an individual pillar..... 59
- Figure 4.18:** (a) and (b) are DI water and hexadecane droplets respectively sitting on the fabricated pillars using the 140 μm gap. The pictures were taken on goniometer 59
- Figure 4.19:** (a) stable-jet, (b) skewed-jet..... 61
- Figure 5.1:** A cartoon illustration of domain A and domain B 64
- Figure 5.2:** Contour lines of electric field when 10 kV applied on the needle and 2 V applied on the mesh using the following mesh gaps: (a) 70 μm , (b) 140 μm , (c) 250 μm , (d) 500 μm . The legend indicates voltage applied on the needle and all axes scale in meters..... 69
- Figure 5.3:** (a) contour lines of electric field used for patterned samples when a 10 kV is applied on the needle and a 2 kV is applied on the mesh using the 140 μm mesh gap, (b) contour lines of electric field used for sample with random surface roughness when only 8 kV is applied on the needle. The legend indicates voltage applied on the needle 70
- Figure 5.4:** Streamlines of electric field when 10 kV applied on the needle and 2 kV applied on the mesh using the following mesh gaps: (a) 70 μm , (b) 140 μm , (c) 250 μm , (d) 500 μm . All axes scale in meters 70
- Figure 5.5:** The charged particles deposition on a substrate using different mesh gaps: (a) is 70 μm gap, (b) is 140 μm gap, (c) is 250 μm gap, (d) is 500 μm gap. The legend indicates the velocity of the particle (m/s) and all axes scale in meters. 72

- Figure 5.6:** (a) the streamlines with 2 kV is applied on the mesh with 70 μm gap, (b) the streamlines when no voltage is applied on the mesh using the same mesh gap. Axes scale of the images is in meters..... 73
- Figure 5.7:** Particle deposition difference on mesh and substrate for 70 μm mesh gap: (a) 10 kV applied on the needle and 2 kV is applied on the mesh, (b) 8 kV applied on the needle and no voltage is applied on the mesh. The legend represents the velocity of the particle (m/s) and axes scale of the images is in meters 73
- Figure 5.8:** Charged particle distribution in each fabricated pillar with respect to different mesh gaps..... 75
- Figure 6.1:** (a) microscopic picture of a sample fabricated at 1 mm mesh gap, (b) microscopic picture of a sample fabricated at 780 μm mesh gap 81
- Figure 6.2:** (a), (b), and (c) are pictures of a sample fabricated using 3 $\mu\text{L}/\text{min}$ material flow rate(d), (b), and (c) pictures of a sample fabricated using 10 $\mu\text{L}/\text{min}$ material flow rate. The mesh gap for both sample was 1 mm..... 82

List of Tables

Table 3.1: Contact angle, sliding angle, and contact angle hysteresis of DI water and hexadecane for samples fabricated with different SiO ₂ concentrations.....	31
Table 4.1: Surface wetting properties of samples with random hierarchical roughness using different spray times.	50
Table 4.2: Wetting properties of samples with patterned multiscale roughness.....	60
Table 5.1: Particle input parameters for simulating the particle trajectory.....	68
Table 5.2: Percentages of material deposited on the substrate and the mesh in addition to the loss in raw material.	74

Abstract**FABRICATING SUPERHYDROPHOBIC AND SUPEROLEOPHOBIC SURFACES WITH
MULTISCALE ROUGHNESS USING AIRBRUSH AND ELECTROSPRAY**

By: Karam N. AL-Milaji, MS.

A thesis submitted in partial fulfillment of the requirements for the degree of Master of Science
at Virginia Commonwealth University.

Virginia Commonwealth University, 2016

Major Director: Dr. Hong Zhao, Assistant Professor, Department of Mechanical and Nuclear
Engineering

Examples of superhydrophobic surfaces found in nature such as self-cleaning property of lotus leaf and walking on water ability of water strider have led to an extensive investigation in this area over the past few decades. When a water droplet rests on a textured surface, it may either form a liquid-solid-vapor composite interface by which the liquid droplet partially sits on air pockets or it may wet the surface in which the water replaces the trapped air depending on the surface roughness and the surface chemistry. Super water repellent surfaces have numerous applications in our daily life such as drag reduction, anti-icing, anti-fogging, energy conservation, noise reduction, and self-cleaning. In fact, the same concept could be applied in designing and producing surfaces that repel organic contaminations (e.g. low surface tension liquids). However, superoleophobic surfaces are more challenging to fabricate than superhydrophobic surfaces since the combination of multiscale roughness with re-entrant or overhang structure and surface

chemistry must be provided. In this study, simple, cost-effective and potentially scalable techniques, i.e., airbrush and electrospray, were employed for the sake of making superhydrophobic and superoleophobic coatings with random and patterned multiscale surface roughness. Different types of silicon dioxide were utilized in this work to in order to study and to characterize the effect of surface morphology and surface roughness on surface wettability. The experimental findings indicated that super liquid repellent surfaces with high apparent contact angles and extremely low sliding angles were successfully fabricated by combining re-entrant structure, multiscale surface roughness, and low surface energy obtained from chemically treating the fabricated surfaces. In addition to that, the experimental observations regarding producing textured surfaces in mask-assisted electrospray were further validated by simulating the actual working conditions and geometries using COMSOL Multiphysics.

CHAPTER 1 Introduction

1.1 Introduction

Over the past decade, textured surfaces have been extensively investigated in order to get better understanding of self-cleaning property presented in nature.¹ Considerable efforts have been devoted to imitate the water repellency phenomenon of lotus leaves, which is also recognized as “lotus effect”, through mimicking its surface topography and surface chemistry.^{2,3} Besides lotus leaves, many different kinds of such surfaces are found in nature such as water strider, geckos’ feet, desert beetles, and other different plants that exhibit very low affinity to water.^{2,4,5} The behavior of a water droplet on a surface can be characterized by contact angles generated when the droplet stabilizes and becomes in a mechanical equilibrium with the surface.⁶ In 1805 T. Young first described the contact angle equilibrium (Fig 1.1a) as water, vapor, and solid interface that is expressed by the equation below.⁷

$$\cos \theta = \frac{\gamma_{sv} - \gamma_{sl}}{\gamma_{lv}} \quad (1.1)$$

where θ is the static contact angle, (γ_{sv}) is surface tension of the solid surface, (γ_{sl}) is solid-liquid interfacial tension, and (γ_{lv}) is surface tension of the wetting liquid. In 1936, Wenzel hypothesized that surface roughness plays an important role in increasing the contact angles by increasing the surface area, which in turn affects both the surface wettability and the anti-wettability depending on the nature of the surface.^{8,9} Wenzel wettability theory is expressed by equation (2.1).

$$\cos \theta^* = r \cos \theta \quad (1.2)$$

where (θ^*) is the apparent contact angle, r is the surface roughness factor that is denoted by the ratio of total surface area to the projected area, and θ is the equilibrium contact angle on smooth

surface measured by equation (1.1). According to Wenzel's assumption, the liquid entirely fills the protrusions of the rough surface when they become in contact (Fig 1.1b).

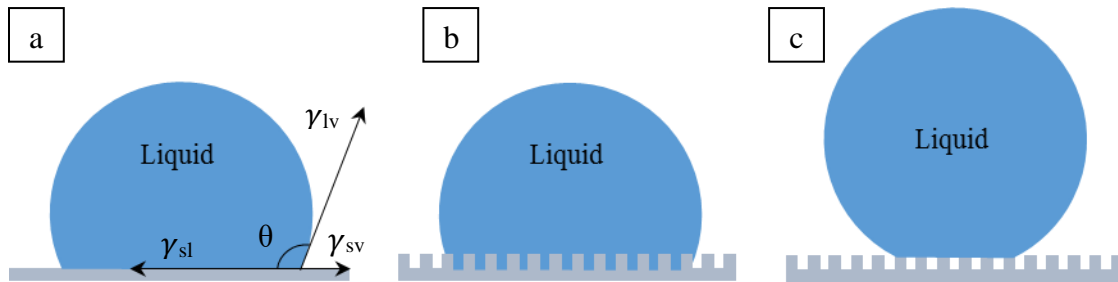


Figure 1.1: Wetting behavior of a droplet on solid substrates: (a) liquid droplet on a smooth surface, (b) Wenzel state, (c) Cassie-Baxter state.

On the other hand, Cassie-Baxter in 1944 came up with another theory, assuming that air pockets could be trapped by a water droplet which enables the droplet to roll off at relatively small angles due to reduction in solid-area fraction and correspondingly wetting area (Fig 1.1c).¹⁰ The apparent contact angle proposed by Cassie-Baxter is given by equation (1.3).

$$\cos \theta_{CB} = f \cdot \cos \theta + (f - 1) \quad (1.3)$$

where θ_{CB} is the Cassie-Baxter contact angle, f is the solid-area fraction, and θ is the contact angle on a smooth surface of the same material.^{6,10}

In addition to the apparent contact angles, liquid droplet behavior on a surface could be characterized by sliding angle and contact angle hysteresis. Sliding angle (Fig. 1.2) gives an indication of droplet's mobility on a surface while contact angle hysteresis (Fig. 1.3), which is the difference between advancing and receding contact angles, depicts the interfacial tension difference between a liquid and a solid during the contact line advancing and receding processes.⁶

Fabricating superhydrophobic surface with contact angle greater than 150° and low contact angle hysteresis (as low as 10°) could be simply made by targeting the micro/nano surface roughness

and the low surface energy.¹¹ However, engineering coatings with same wetting properties against low surface tension liquids such as hexadecane ($\gamma_{lv} = 27$ mN/m), decane ($\gamma_{lv} = 23.8$ mN/m), and octane ($\gamma_{lv} = 21.6$ mN/m) is not possible unless a third factor is added to the surface which is the re-entrant or the overhang structure.^{5,12,13,6,14-17}

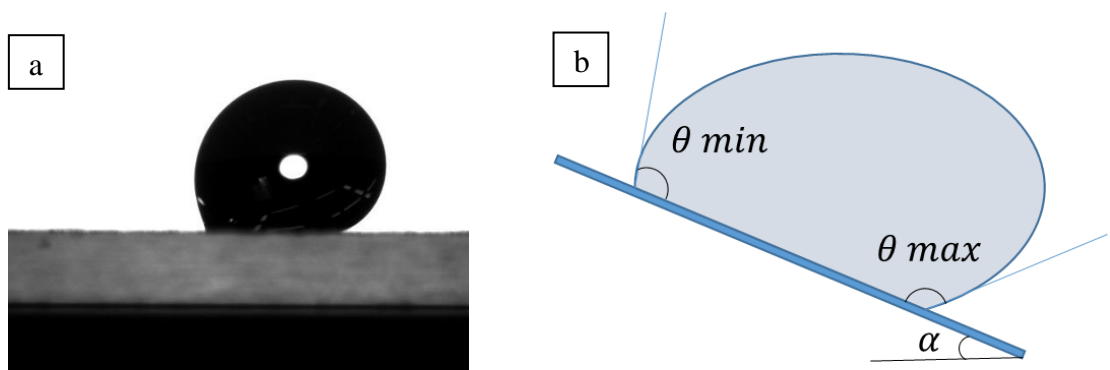


Figure 1.2: (a) a 5 μ L water droplet tilted at 45°, (b) an illustration of tilting angle.

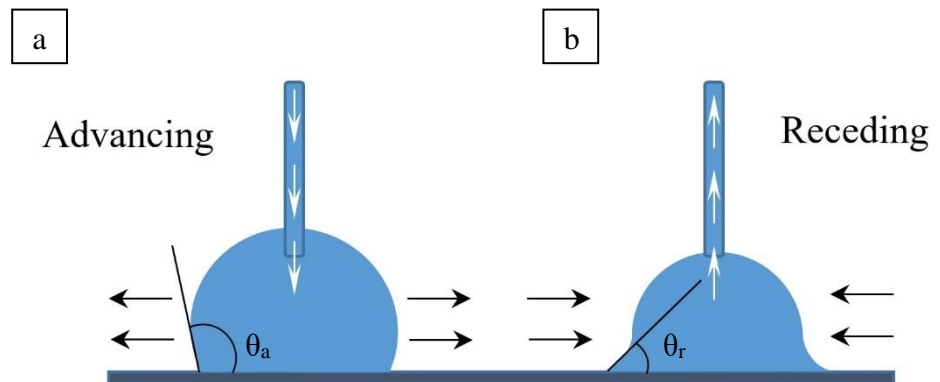


Figure 1.3: (a) advancing contact angle during contact line advancing, (b) receding contact angle during contact line receding.

The main goal of mimicking the lotus leaf structure is to provide a solution to many engineering problems like self-cleaning, anti-fogging, anti-smudge, drag reduction, and oil water separation.¹⁸⁻
²³ However, generalizing the super liquid repellent coatings to a large scale, finding cost-effective fabrication method, providing mechanically robust textures, and preventing the trapped air (air

pockets) from escaping under high pressures, are all obstacles. If solved, they will provide a precious gift to many engineering applications.

1.2 Motivation

1.2.1 Superhydrophobic (SHP) surfaces

Recently, the number of studies regarding the lotus leaf effect offered by nature have been exponentially increased.^{24,25} The water makes a contact angle above 160° and slides at angle as low as 4° , by which all the dirt and the dust particles attached to the lotus leaf could be carried away leaving the surface clean.^{2,6} This observation has appealed a tremendous interest for both fundamental research and practical applications.²⁶ The crucial factors of superhydrophobicity are surface roughness and low surface energy.^{8,10,27-30} Accordingly, Numerous artificial SHP surfaces have been fabricated up to date, in which coatings with random surface roughness and coatings with regular textures were used to mimic the self-cleaning effect of lotus leaves. For instance, super water repellent surfaces were obtained by fabricating pillar arrays where the surface roughness and thus the solid-area fraction under a water droplet could be controlled by pillar height, geometry, and spacing.³¹ SHP surface could be also produced by targeting the random multiscale surface roughness. Ming *et al.* fabricated SHP surfaces with dual scale roughness by having the silica-based raspberry like particles to be covalently bonded with an epoxy-based polymer matrix. After chemically treating the surface, the coating exhibited 165° water contact angle and 3° sliding angle.³² Furthermore, Mammen *et al.* reported that robustness of the SHP surface could be enhanced with retaining the Cassie-Baxter state when the side wall of micropillars are hydrophobized even though the top of the pillars were made of hydrophilic material.³³ However, the SHP surfaces found in nature in addition to the artificial ones don't survive against

contaminants and organic solvents. This shortfall of these surfaces in resisting low surface tension liquids highlighted the strong need for superoleophobic surfaces.

1.2.2 Superoleophobic (SOP) surfaces

While there are several natural and engineered super water repellent surfaces, it is very challenging to find natural SOP surfaces that could survive against the low surface tension liquids such as hexadecane and alcohol.³⁴ Numerous studies have demonstrated that fabricating SHP surfaces with water contact angles greater than 150° and low contact angle hysteresis is relatively a simple process. However, engineering surfaces that show low affinity toward most of the low surface tension liquids like hexadecane is not achievable unless re-entrant or overhang structure in addition to surface roughness and low surface energy are provided.^{5,15,16} Zhao *et al.* utilized photolithography followed by surface treatment of fluoropolymer monolayer to obtain SOP surfaces and further investigated their different wetting properties through changing diameter, height, and side shape of the pillars.^{12,14} After comparing different pillar dimensions and shapes, Zhao *et al.* concluded that the pillar geometry that is represented by the re-entrant structure along with the surface chemistry are major contributors for superoleophobicity. Furthermore, Kota *et al.* elucidated how the developed re-entrant hierarchical structure with multiscale roughness could support the Cassie-Baxter state by displaying high contact angles and low contact angle hystereses with contacting liquids because of the reduction in the contact area between the liquid and the textured surface.¹⁶

Despite the fact that tremendous efforts are dedicated to fabricate surfaces that have high repellency toward different types of liquids especially those with low surface tensions such as hexadecane, heptane, and octane, nothing truly has been proven yet as a rigorous solution to

address the fabrication of SOP surfaces using manufacturing-intend techniques, topology control of SOP surfaces, and generalization of such coatings to large scale applications.

1.3 Objectives

The first research objective of the present study is to investigate SHP and SOP surfaces with multiscale roughness through implementing manufacturing-intend coating techniques such as air spray and electrospray deposition, and to establish processing-structure-property relationships by fabricating such surfaces under various processing conditions. The second objective of this study is to understand the influence of surface topography and surface chemistry on surface wettability. The surface morphology is characterized by scanning electron microscopy (SEM), laser scanning microscopy (LSM), and atomic scanning microscopy (AFM). Surface wettability is characterized by measuring the contact angles and sliding angles of water and hexadecane on those fabricated surfaces. Such surfaces could be employed in many applications e.g. for self-cleaning, anti-smudge, and for drag reduction purposes. As the cost is one of the major concerns in industry field, the silicon dioxide is used in this study to obtain the desired surface roughness since silica is normally inert with most of chemicals, environmentally stable, and is one of the most abundant materials on earth.³⁵

The third objective of this study is to simulate the electrospray deposition process using COMSOL Multiphysics in order to interpret, verify, and support the experimental observations.

1.4 Outline

In this thesis, an extensive study on different types of textured surface including their fabrication processes have been accomplished in order to provide a better understanding of their effect on surface wettability against low surface tension liquids. The chapters of this thesis are organized as follows: Chapter 2 is a literature review regarding SHP and the origin of SOP surfaces

in addition to fabrication methods used to produce those surfaces. Chapter 3 explains the fabrication of super-liquid repellent surfaces with random multiscale roughness using the spray coating of silicon dioxide (SiO_2) powder suspension at various concentrations. Furthermore, surfaces made by SiO_2 suspensions with different agglomerate sizes i.e., directly-dispersed suspension and surfactant-assisted suspension, are discussed in the same chapter. Chapter 4 presents how the electrospray is implemented in engineering SHP and SOP surfaces with micro/nanoscale surface roughness through spraying a well-dispersed (surfactant-assisted) SiO_2 suspension at various time periods. Particularly, mask-assisted electrospray technique has been employed to fabricate SHP and SOP surfaces with much reduced solid-area fraction, and enhanced SHP and SOP properties. The simulation and the validation of experimental findings using COMSOL Multiphysics is given in chapter 5. The last chapter is overall conclusions and recommendations for future work.

CHAPTER 2 Literature Review

In chapter one the concepts of liquid wetting behavior on textured surfaces were introduced according to Wenzel and Cassie-Baxter states. This chapter provides an overview of SHP and SOP surfaces such as self-cleaning property of lotus leaf, origin of superoleophobicity, and fabrication processes used in this arena so that a thorough insight could be obtained about the above-named surfaces.

2.1 Superhydrophobic surfaces

Surfaces with self-cleaning property have been extensively studied during the last decades. The well-known and the most famous super water repellent surface is the lotus leaf. Water makes a contact angle above 160° and slides at angle as low as 4° by which all dirt and dust particles attached to lotus leaf could be carried away leaving the surface clean.^{2,6} This observation has appealed a tremendous interest for both fundamental research and practical applications in order to understand and to identify the important role of the surface topography (hierarchical structure) along with the surface chemistry and their influence on water repellency, contact angle hysteresis, breakthrough pressure, and mechanical properties.^{6,26,36-42} The high degree of water repellency (superhydrophobicity) is characterized by combining low surface energy with hierarchical surface structure. Barthlott and Neinhuis clearly defined the term lotus effect by contact angle measurements, showing that the lotus leaf presents high contact angles and low rolling angles that help the lotus leaf to stay clean.² Barthlott and Neinhuis attributed the reason behind this phenomenon to the presence of hydrophobic surface (cuticle) that is covered by micro-structured epicuticular wax crystalloids with in approximate height of 1-5 μm . Similarly, J. Li *et al.* examined the lotus leaf under the laser scanning confocal microscope (LSCM) and the SEM to investigate the surface morphology. They also asserted that the lotus effect is a result of multiple coupling

contents like the microstructure and the surface energy.⁴³ However, Feng *et al.* discovered later that the lotus leaf has a nanoscale structure on the top of the micro-papillae which is considered a crucial factor behind the excellent water-wetting properties.⁴⁴ Even though superhydrophobicity could be produced by combining surface roughness in micron scale and low surface energy, surface wetting robustness could be further improved by targeting the a hierarchical (multiscale) structured roughness. In 2010, Cha *et al.* explained and underlined the significance of the nanotextures existed on lotus leaves. Cha *et al.* reported that robustness of SHP surfaces against the applied pressure by a liquid droplet could be greatly enhanced when the textured surface is composed of dual roughness (Fig. 2.1).⁴⁵ As the hierarchical surface roughness is proven to enhance the wetting stability against water, it also contributes to high contact angle hysteresis that is theoretically calculated by Liu *et al.*⁴²

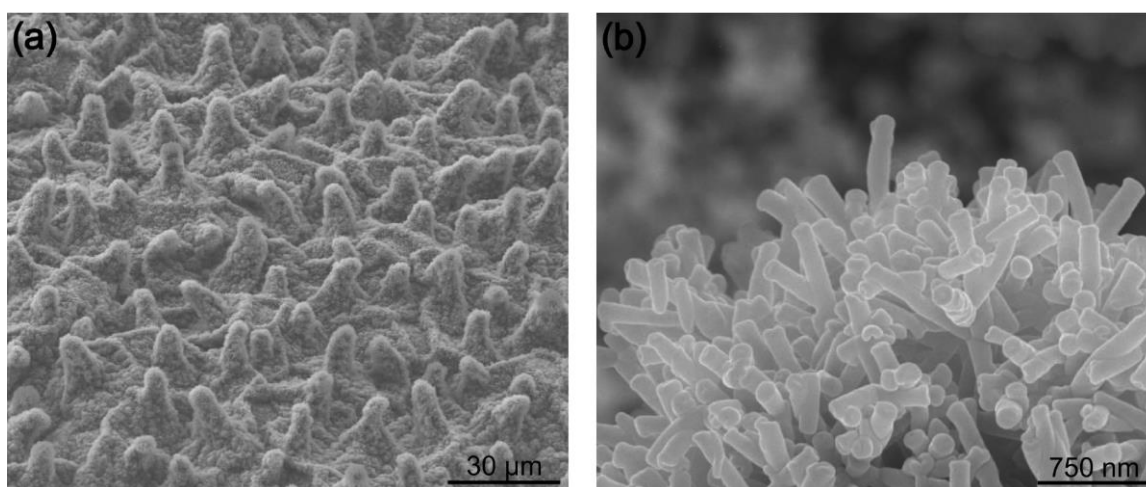


Figure 2.1: Dual surface roughness of lotus leaves: (a) lotus leaf microstructure, (b) nanostructure of lotus leaves.⁴⁵

2.2 The origin of superoleophobicity

As many types of SHP surfaces are provided by nature, it is very challenging to find naturally occurring SOP surfaces that successfully inhibit low surface tension liquids such as

hexadecane ($\gamma_{lv} = 27$ mN/m) from wetting the textured surfaces.^{16,46} Surfaces that resist contaminants and organic solvents could have an impact on a wide range of advantageous applications such as self-cleaning, resistance of biofouling and anti-smudge, reduction of drag, and separation of oil and water.¹⁸ According to Tuteja *et al*, the superoleophobicity is not achievable by only combining surface roughness with surface chemical composition, unless a third factor (i.e., re-entrant curvature) is involved.⁵ Tuteja *et al*. supported their statement by two approaches: Firstly, SOP surfaces were achieved by electrospinning the synthesized hydrophobic 1H,1H,2H,2Hheptadecafluorodecyl (referred to as fluorodecyl POSS) blended with different weight percentages of hydrophilic polymer — poly(methyl methacrylate)(PMMA) as shown in Figure 2.2. Secondly, a regular re-entrant structure was created on SiO₂-silicon wafer. The SOP surface with hoodoo's structure was obtained by etching the silicon dioxide layer followed by chemical treatment with 1H,1H,2H,2H-perfluorodecyltrichlorosilane, by which the fabricated surface showed high contact angles and low sliding angles against various low surface tension liquids (Fig. 2.3).

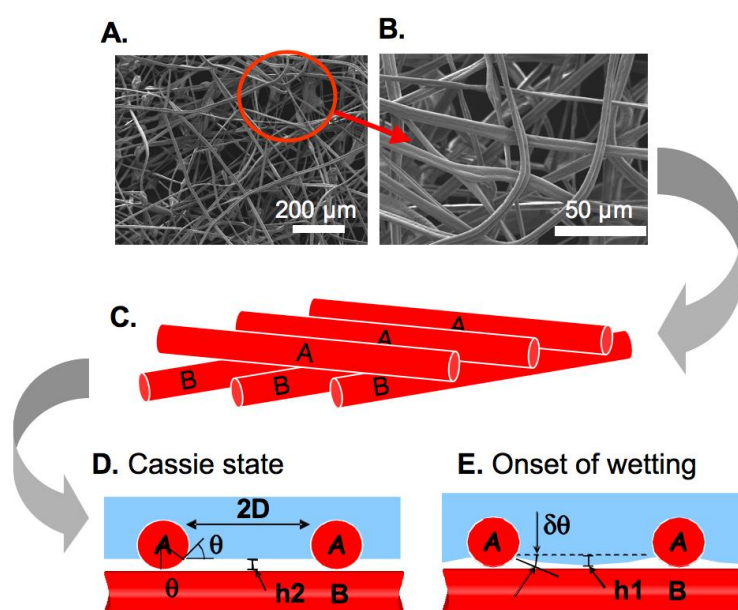


Figure 2.2: (a) and (b) SEM pictures of electrospun mat, (c) the alignment illustration of electrospun mat, (d) Cassie-Baxter state provided by re-entrant structure, (e) liquid sagging due to an external applied pressure.⁵

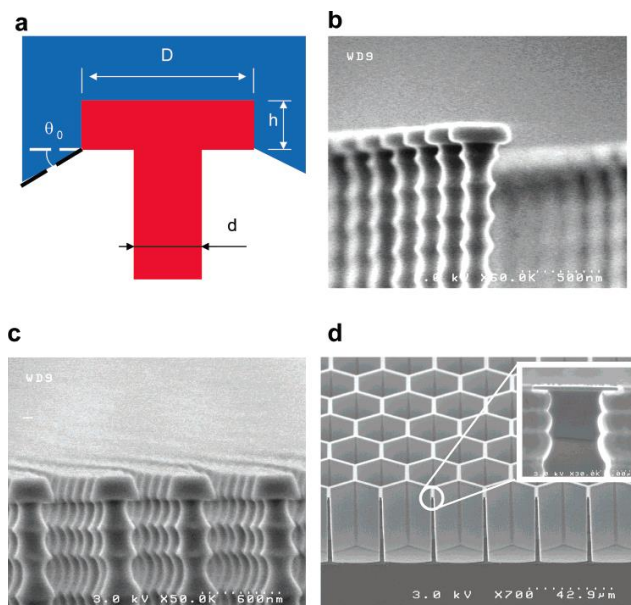


Figure 2.3: (a) an illustration of formation of liquid-solid-vapor interface of textured surface with re-entrant structure, (b), (c), and (d) SEM images of the fabricated re-entrant structures.⁵

Zhao *et al.* directly compared the wetting properties of textured surfaces with straight sidewall pillars, wavy sidewall pillars, and pillars with micro-hoodoos. All of which have the same surface chemistry.^{12,14} The surface with straight sidewall pillars presented lack of re-entrant structures and superoleophobicity (Fig. 2.4).

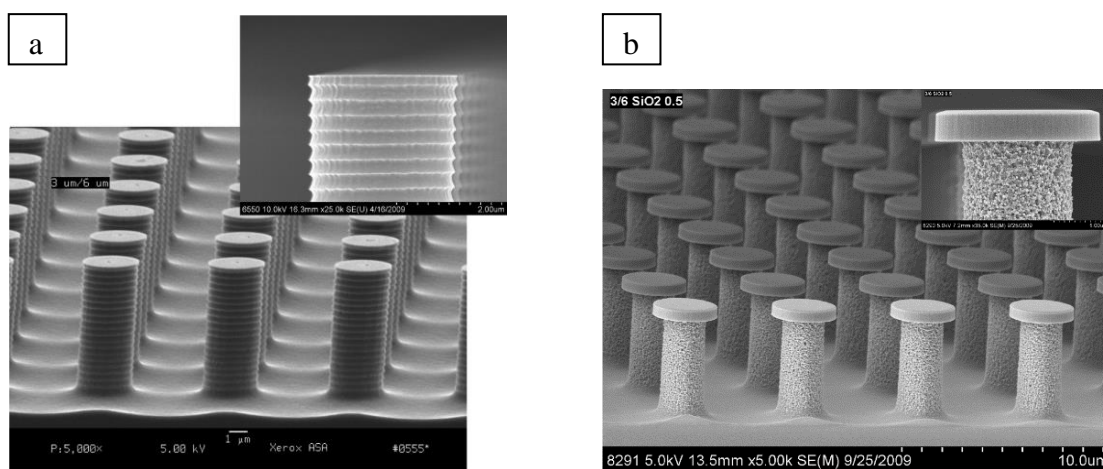


Figure 2.4: (a) SEM image of the wavy side wall pillars, (b) SEM image of the overhang structured pillars.¹²

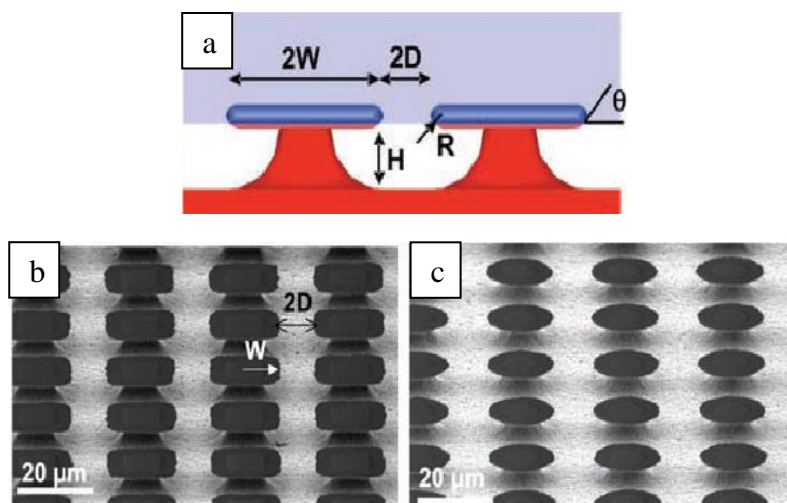


Figure 2.5: (a) schematic of the overhang structure, (b), and (c) SEM images of the fabricated overhang structure.⁴⁷

Moreover, Choi *et al.* recognized that the oleophobicity of surfaces with re-entrant structure like lotus leaves and duck feathers could be tuned when they are dip-coated with fluorodecyl polyhedral oligomeric silsesquioxane (POSS) polymer.¹⁵ The superoleophobicity of a lotus leaf and a duck feather is obtained when the low surface energy of the (POSS) is combined with the re-entrant structure.¹⁵ In addition to the re-entrant structure, Ahuja *et al.* experimentally demonstrated that SOP surfaces could be designed by having the overhang structure (nanonails) shown in Figure 2.5 by which the Cassie-Baxter state is maintained against various low surface tension liquids.⁴⁷ As a conclusion, SOP surfaces are not attainable unless the re-entrant structure is provided since the low surface tension liquids such as the hexadecane tend to wet surfaces with textures similar to lotus leaf. Meaning that, the above mentioned structures have led to a major advance in wetting robustness against low surface tension liquids.¹⁴

2.3 Fabrication of superhydrophobic and superoleophobic with random surfaces roughness

2.3.1 Electrospinning and electrospray

Electrospinning is one of the common ways of generating randomly spaced surface textures (fibers) with multiscale roughness.⁴⁸ A high voltage source is applied to a pressurized liquid that

is fed by a syringe pump. The applied voltage makes liquid droplets to erupt and disintegrate due to the electrostatic repulsion to form a liquid jet. Zheng *et al.* produced their SHP surfaces by electrospinning the Polystyrene (PS).⁴⁹ by controlling electrospinning conditions, Zheng *et al.* were able create surfaces with different morphologies such as beads with different sizes and shapes in addition to beads-on-strings in order to investigate the relationship between wetting properties and surface morphologies. As different wetting properties were observed with various solutions, the highest water contact angle ($\sim 160^\circ$) was produced by electrospinning the DMF with 5% PS solution (Fig. 2.6).^{49,50}

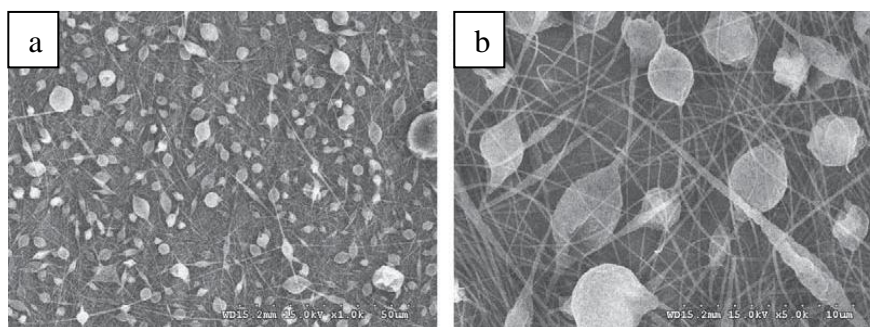


Figure 2.6: (a) electrospun micro-beads, (b) electrospun beads-on-strings.⁴⁹

Same procedure could be applied in electro spray if the operation conditions (voltage, working distance, flow rate) and the liquid parameters (viscosity, molecular weight, solvent) are carefully regulated.⁵¹

Since the electro spray is used to deposit charge particles on conducting substrates to generate thin films,^{52,53} Burkarter *et al.* decided to implement the electro spray technique to create SHP surfaces by spraying PTFE.⁵⁴ For better conductivity purposes a doped fluorine tin oxide (FTO) glass slides were used as a substrate. According to Burkarter *et al.*, most of the solvents evaporate within the path between the needle and the substrate. Nevertheless, the use of a hot substrate boosted the adhesion of the charged PTFE particles to the substrate and enhanced the evaporation of the

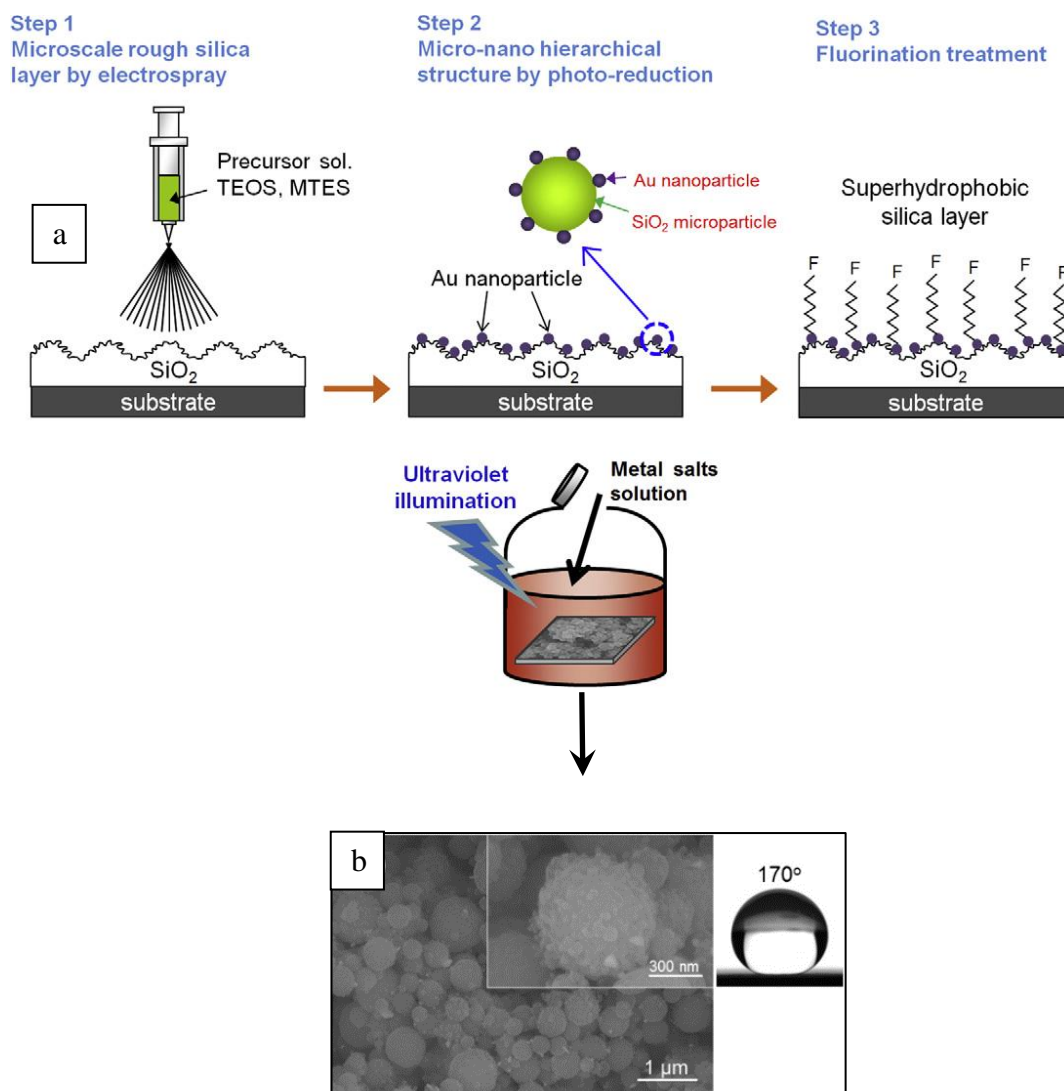


Figure 2.7: (a) electro spray deposition steps of SiO_2 layer in with Au nanoparticles producing micro-nano hierarchical structure, (b) high water contact angle after fluorinating the sample.³⁵

remaining solvent as well. After spraying the samples for 20 min and heat treating the sprayed samples up to 265°C to remove the wetting agents, the samples became SHP with excellent surface wetting properties (above 160° water contact angle and 2° sliding angle).

In order to mimic the biological hierarchical structure of lotus leaves, J. Y. Kim *et al.* fabricated a SHP surfaces by electro spraying silicon dioxide that is prepared by a sol-gel and sprayed on a silicon wafers to produce very rough silicon dioxide layers.³⁵ However, high water repellency

surfaces require a combination of the micro-nano roughness. For this reason, the sprayed samples were further treated with ultraviolet (UV) irradiation, which enhanced the chemical reduction process, to add Au nanoparticles onto the silicon dioxide layer (Fig. 2.7). Moreover, as the roughness alone is not enough for producing superhydrophobicity, it was necessary to reduce the surface energy by fluorinating the samples with trichloro(1H,1H,2H,2H-perfluorooctyl)silane by which high water contact angles ($\sim 170^\circ$) were achieved.

Despite the fact that SHP surfaces were fabricated by electrospray^{35,54} and electrospinning,^{49,50,27} much fewer research have been conducted on creating SOP surfaces by electrospray and electrospinning. Tuteja *et al.* generated SOP surfaces by electrospinning fluorodecyl POSS blended with different weight percentages of hydrophilic polymer — poly(methyl methacrylate)(PMMA). Very high contact angles and low contact angle hystereses for low surface tension liquids have been achieved on fiber mat with dual surface roughness.⁵

2.3.2 Spray coating

Air spray, which is also called “airbrush”, is one of the simplest and the most cost-effective ways that might be implemented to fabricate large scale liquid repellent surfaces with random surface roughness. Simply, it is a process of spraying surfaces by a preferred material to generate a multiscale surface roughness, which is considered one of the key factors to hit the property of robust super liquid repellent coatings. Steele *et al.* implemented the spray casting to design SOP textured coatings.¹³ The nanoparticle-polymer suspension, which is superoleophobic in nature, was sprayed on a microscopic glass slide using 30 cm working distance to produce hierarchical nano-textured surfaces (Fig. 2.8).

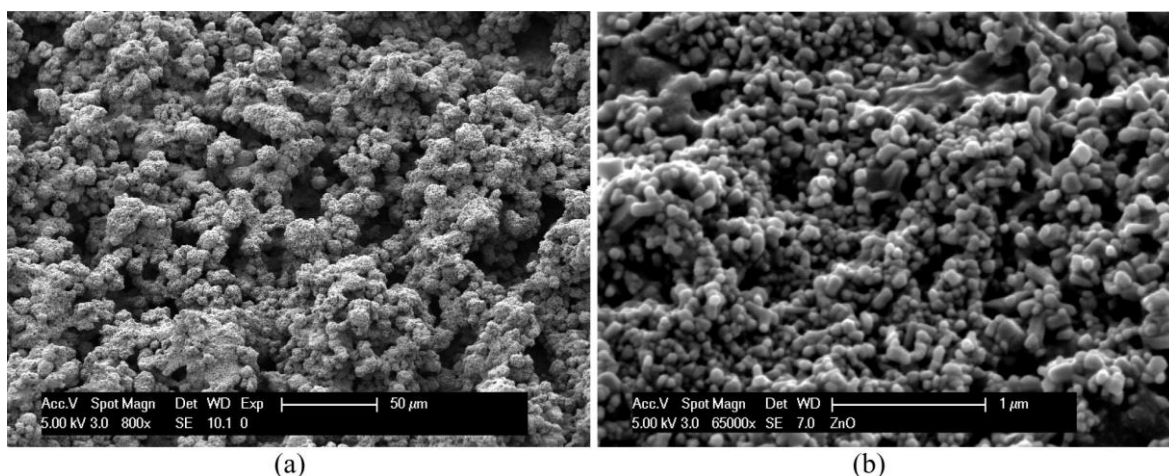


Figure 2.8: (a) and (b) SEM pictures of hierarchical textured surface with micro-nanoroughness.¹³

In order to obtain a uniform coating and to avoid coffee stain effect during the spray process, a substantial portion of the solvent should evaporate within the spray mist before impacting the substrate. For this reason, the Acetone was the best fit for this purpose because its boiling point is much lower than that of water. Similarly, Raymond *et al.* have designed their coatings through spraying a mixture of fluoroalkylfunctional precipitated silica and a fluoropolymer binder in order to acquire super liquid repellent surfaces with re-entrant structure.¹⁷ After drying the sample for 1 h in air then baking the sample by the oven to temperature up to 60 °C, the desired superoleophobicity was obtained. In other words, the mission was accomplished by combining the low surface energy and the surface roughness with the re-entrant structure that is represented by aggregate porosities.

2.3.3 Layer by layer deposition

Super liquid repellent surfaces could be fabricated by manipulating the roughness of surfaces through adjusting the size and directing the placement of the agglomerates obtained from depositing nanoparticles on different types of substrates. Bravo *et al.* reported that SHP coatings

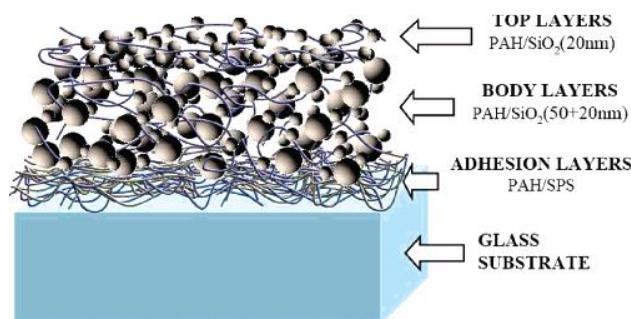


Figure 2.9: An illustration scheme of layer by layer deposition.⁵⁵

with high transparency (above 90%) could be produced by immersing the substrate sequentially into different types of aqueous solutions.⁵⁵ Their samples were prepared by alternately dipping the microscopic glass slide in to a cationic solution and an anionic solution for 15 min and rinsing the samples with DI water in-between. The anionic solution was composed of two different silica nanoparticle sizes in order to target the desired surface roughness. After depositing the required layers, the samples were then calcinated at 550 °C for 4 h to remove the solvents and to enhance the mechanical robustness of the coatings. Lastly, the samples were chemically treated with trichloro(1H,1H,2H,2H-perfluorooctyl) silane to reduce the surface energy. Figure 2.9 illustrates the multilayer deposition mechanism in which samples with high transparency present high advancing contact angles ($>160^\circ$) and low contact angle hystereses ($<10^\circ$). Similarly, Brown and Bhushan demonstrated that by applying similar concept, durable super liquid repellent coatings could be created for different applications e.g., self-cleaning, anti-smudge, low-drag, anti-fog, and oil-water separation.¹⁸ Brown and Bhushan fabricated their samples by spray coating various layers of Polydiallyldimethylammonium chloride (PDDA) followed by silica nanoparticles suspensions with different concentrations in order to have the desired surface roughness. After baking the samples at 140 °C for 1 h, the samples were then fluorinated by spraying another layer of the fluorosurfactant solution (FL, Capstone FS-50, DuPont) to make the samples superhydrophilic but superoleophobic that is suitable for oil-water separation purposes. Figure

2.10 depicts the procedure followed by Brown and Bhushan to fabricate oil repellent coatings in which the mechanical robustness is enhanced by electrostatic interactions.

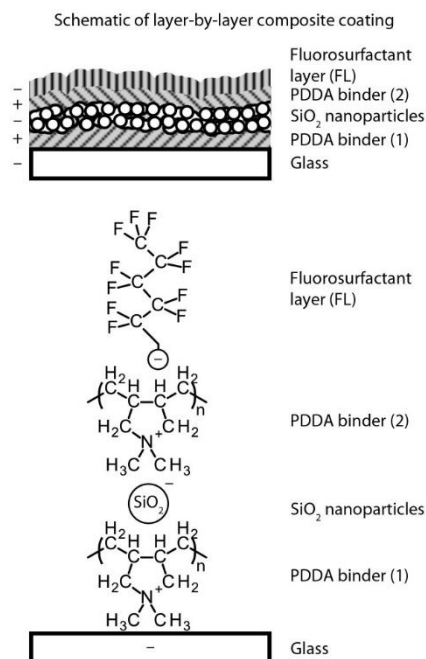


Figure 2.10: A modified scheme of layer by layer deposition.¹⁸

2.4 Fabrication of superhydrophobic and superoleophobic with regular textured surfaces

As different approaches have been employed to mimic the self-cleaning property of lotus leaf though producing random and multiscale surface roughness, such surfaces have been fabricated in more systematic approach through the use of photolithography in order to investigate fundamental liquid-solid wetting interactions on textured surfaces. The photolithography is a process of transferring the mask patterns to a sample that is cover with a photoresist layer. This process has been well-implemented in fabricating SHP surfaces with different pillar geometries during the past few years.^{56,57} Oner and McCarthy employed photolithography to fabricate textured surfaces with different pillar sizes, geometries, and spacing. The patterns were produced on silicon wafers using the contact lithographic mode, then the samples were etched and chemically treated

with silanization reagents prior to contact angle measurements.³¹ Oner and McCarthy reported that the fabricated surfaces exhibit ultra-high contact and sliding angles when the pillar X-Y dimensions are between 2 and 36 μm (Fig. 2.11). Also, they concluded that the surface wetting properties are independent of pillar height and surface chemistry. However, Oner and McCarthy noticed that at 56 μm pillar spacing, the contact angle decreases drastically due the transition from Cassie-Baxter to Wenzel state.

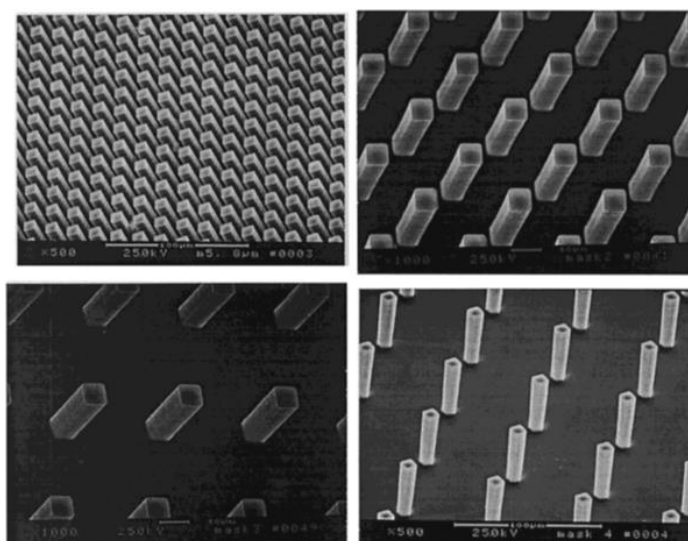


Figure 2.11: SEM images of different pillar geometries produced via photolithography.³¹

Similarly, Zhao *et al.* utilized photolithography and etching to create different types of textured silicon dioxide surfaces and studied the wetting properties of those super liquid repellent surfaces. A repetitive etching of the silicon wafers were performed to a certain depth using the Bosch deep reactive-ion etching (DIRE) so that wavy sidewall pillars were created which provided the necessary re-entrant structure for superoleophobicity. The superhydrophobicity and the Superoleophobicity were ultimately attained after chemically treating the designed surfaces with fluorosilane (FOTS) to reduce the surface free energy.¹²

The same group demonstrated the ability to fabricate SHP and SOP surface with groove structure using the same technique (Fig. 2.12). The groove patterned samples were proven to have high liquid mobility that is represented by lowering the solid-area fraction by 50%.⁵⁸

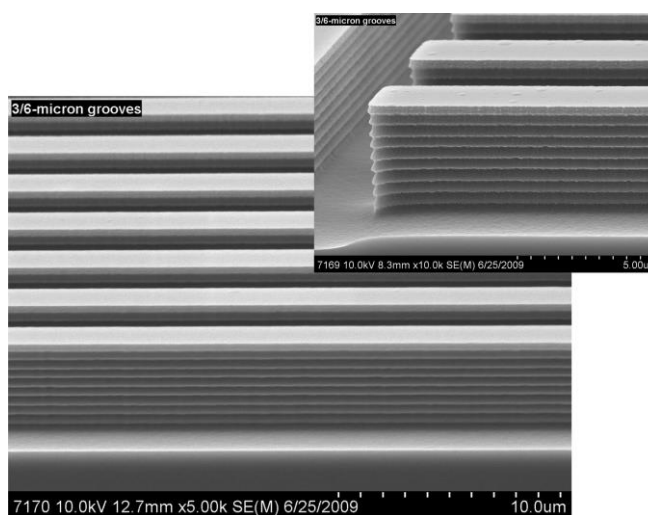


Figure 2.12: Groove patterning fabricated by Zhao *et al.*⁵⁸

It should be mentioned that many process besides the above reviewed are also used in creating SHP and SOP surface such as atom transfer radical polymerization (ATRP), Casting, Chemical vapor deposition (CVD), Dip-coating, Etching, Polymerization, Pyrolysis, Sol-gel, Solution-immersion, and Template.^{9,59,60}

CHAPTER 3 Fabricating Superhydrophobic and Superoleophobic Surfaces Using

Airbrush

3.1 Introduction to airbrushing

In recent years, the trend of engineering liquid repellent coatings is of great interest because of their special and desirable characteristics such as self-cleaning,¹ antifogging,^{19,20} drag reduction,^{22,23,61} freezing delay,⁶² windshields,⁶³ and water–oil separation.^{18,64} Remarkable accomplishments have been recently reported for such type of surfaces by using different techniques such as electrospinning,⁴⁸ photolithography,^{12,14} plasma etching,⁶⁵ and chemical vapor deposition.⁶⁶ Despite the noteworthy achievements made by the aforementioned processes, most of them involve expensive, time consuming, multistep procedures to make one sample, poor applicability to few materials and substrates, and limited practical applications.⁶⁷ Therefore, many of these techniques are not suitable for generating scalable and cost-effective SHP and SOP surfaces. In this study, we employed a facile approach to fabricate such coatings in order to tackle the above mentioned engineering hurdles. The spray coating or the so called “airbrushing” is a well-known process in many industry disciplines such as photoresist coating and painting.⁶⁸ Airbrushing is considered as a facile and cost-effective air operated tool in which scalable SHP and SOP surfaces with micro/ nanoscale surface roughness could be obtained.¹⁷ The objective of this study is to engineer surfaces that are repellent to low surface tension liquids and to establish structure-property relationships on those surfaces by characterizing surface topography, surface roughness, wetting properties, and coating transparency so that practical, efficient, and inexpensive coatings with repeatable results could be attained.

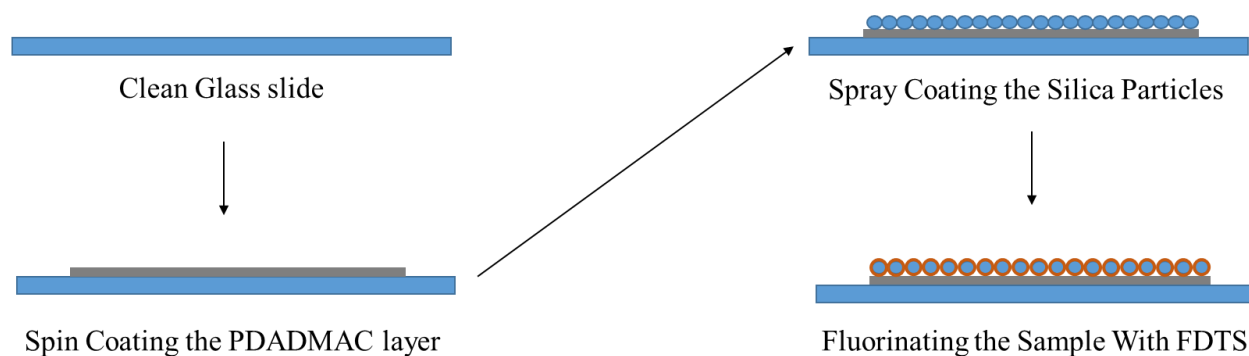


Figure 3.1: A schematic of coating procedure.

3.2 Materials and methods to fabricate textured surfaces

A complete fabrication process is illustrated in (Fig. 3.1). The silicon dioxide (SiO_2) is mechanically and thermally stable and could be used in designing coatings with high transparency for optical display devices.⁶⁹ All the textured surfaces studied in this chapter are fabricated on glass slide (Fisher Scientific). Each glass slide was cut into dimensions of 2.5 cm x 3.8 cm and used as a substrate. The substrate was cleaned rigorously by hot soapy water, Acetone, and Isopropanol, then rinsed with DI water and dried by clean air. The clean glass slide was further cleaned by plasma cleaner (HARRIC PLASMA PDC-001-HP-115V) for 5 minutes to assure that the substrate was thoroughly cleaned. An excessive cleaning process is crucial for generating super liquid repellent surfaces, because any contamination existing on the surface affects the adhesion of the coating layer with the substrate, resulting in wetting failure on the defective locations. Polydiallyldimethylammonium chloride (PDADMAC, 20 wt % in H_2O , Aldrich) was diluted in DI water to obtain 52 mg/mL PDADMAC concentration. The PDADMAC layer provides good adhesion to glass substrate,^{70,71} and can act as a positive electrolyte which establishes an electrostatic force with the negatively charged SiO_2 nanoparticles to form a robust coating.¹⁸ A thin layer of the PDADMAC was spin coated onto the previously cleaned glass slide by a spin coater

(SCS 6800 spin coater from KISCO) at 3000 rpm. SiO₂ powder (AEROSIL 200 F, Evonik Industries) with a primary particle size of 13 nm was mixed with acetone at various concentrations using an ultrasonic bath (Fisher Scientific, M/MH Series Operation, CPX-952-117R) for 1 h. An airbrush (Master Performance multi-purpose with dual action gravity feed) with 0.3 mm nozzle diameter and 25 psi air pressure was utilized to spray coat the homogeneous silica suspension on the PDADMAC coated substrate as shown in (Fig. 3.2).

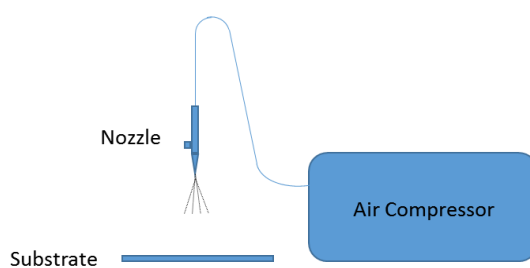


Figure 3.2: A schematic of spray coating.

In order to obtain a uniform silica coating layer throughout the substrate with multiscale roughness, the spray nozzle was held constant at the top of the substrate at 20 cm working distance and 3 μ L of SiO₂ suspension with 15 mg/mL concentration was sprayed. The sprayed samples were baked for 1 h at 140 °C in a convention oven (Fisher Scientific 700) to dry off the solvent. Since the surface roughness only is not enough for getting the high liquid repellency, it is necessary to reduce the surface energy through fluorinating the samples with a fluoropolymer, 1H, 1H, 2H, 2H-Perfluorodecyltrichlorosilane 96% (FDTS) from Alfa Aesar. The trichlorosilane forms a covalent bonding through the hydroxyl groups on the SiO₂ surface, providing a uniform self-assembled FDTS coating layer. The samples were plasma cleaned for 5 minutes to enhance the adhesion of FDTS with silica particles. The surface treatment of FDTS was done through vapor deposition process, 15 μ L of FDTS and the samples were put in a jar that is purged with nitrogen due to high affinity of FDTS to react with moisture. The sealed jar container was heated at 90 °C for 1 h to

allow FDTS to react with the SiO₂ particles. Lastly, the fluorinated sample was heat-treated for 30 min at 140 °C prior to the contact angle measurements. It should be mentioned that the fluorination process is not successful unless the samples are treated again with plasma before this step. The lack of success could be attributed to the contamination resulted from heating the PDADMAC during the baking process which in turn covers the silica particles and prevents bonding with FDTS.

As glass substrates and silica particles are negatively charged, the PDADMAC is positively charged by which the coating robustness is enhanced because of the electrostatic interactions.¹⁸ The SiO₂ powder with primary particle size of 13 nm, tend to form bigger agglomerates (e.g. 350 nm at a concentration of 15 mg/mL) when they are directly dispersed in acetone (Fig. 3.3). However, the nanoscale agglomerates grow even more when they become in contact with air during the spraying process.

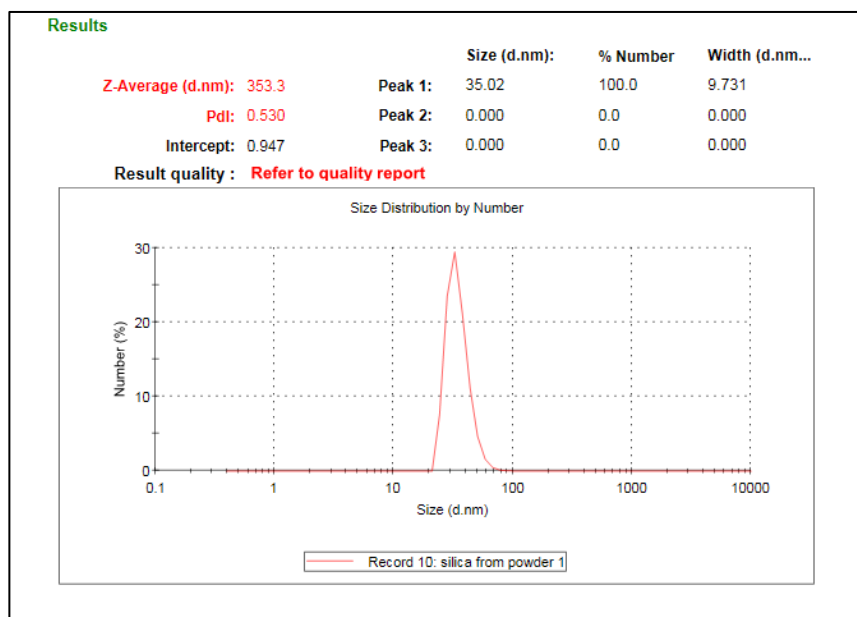


Figure 3.3: Particle size measurement of a SiO₂ suspension (15 mg/mL) by dynamic light scattering.

Therefore, the SiO₂ suspension should be sprayed within 15 min after ultra-sonicating the silica powder with acetone.¹⁷

As a matter of fact, these agglomerations are beneficial to some extent, the re-entrant structure gained from silica agglomerates successfully prevents the DI water and the hexadecane from wetting the surface (Cassie-Baxter state).

3.3 Contact angle measurements and surface morphology characterization

The contact and sliding angle measurements were conducted on a goniometer (OCA 15 CE) from Dataphysics. A 250 μ L Hamilton syringe with a 0.21 mm stainless steel needle were used. The syringe type and volume in addition to the needle size should be specified in the goniometer's software. For apparent contact angle measurements, 3 μ L droplets for DI water and hexadecane were gently dispensed on the testing substrate. Each reported data was an average of 5 independent measurements on different sample locations. The sliding angle is defined as the minimum slope measured in degrees at which the liquid droplet starts to slide or roll. It is customary to use a 10 μ L droplet size in tilting angle measurements with tilting rate of 1 %/s.⁶ The contact angle hysteresis was calculated by subtracting the advancing and receding contact angles obtained from the recorded frames of the sliding angle measurement.

It is worth noting that the accuracy of the apparent contact angle measurements mainly depends on the CCD camera ability which determines if a crisp image of the sessile droplet could be obtained, the baseline establishment upon which the contact angle is calculated, and the illumination adjustment. In our study, all the contact angle measurements were calculated by the ellipse fitting method. In this case, the crucial factors in making accurate and precise contact angle measurements with the least fitting error are the droplet profile and the baseline.

An ultra-high resolution HITACHI SU-70 FE-SEM was used with 5 kV operating voltage and 15 mm scanning distance to characterize the morphology of the textured surfaces. To minimize charging effect of the silica particles, the samples were coated with platinum using platinum sputter (Denton Vacuum Desk V) for 60 sec. Furthermore, a laser scanning microscope (LSM Zeiss 710) and an atomic scanning microscope (AFM Burker Dimension Icon) were implemented for further surface characterization e.g., three-dimensional morphology and quantitative surface roughness measurements.

3.4 Results and discussion

3.4.1 Effect of silicon dioxide concentration on surface morphology and wettability

In this study, various concentrations of SiO₂ suspensions were prepared by directly dispersing silica powder in Acetone followed by ultrasonication. The samples were fabricated and characterized according to the procedure described in the previous section. Figure 3.4 shows SEM images of surfaces prepared at various SiO₂ concentrations.

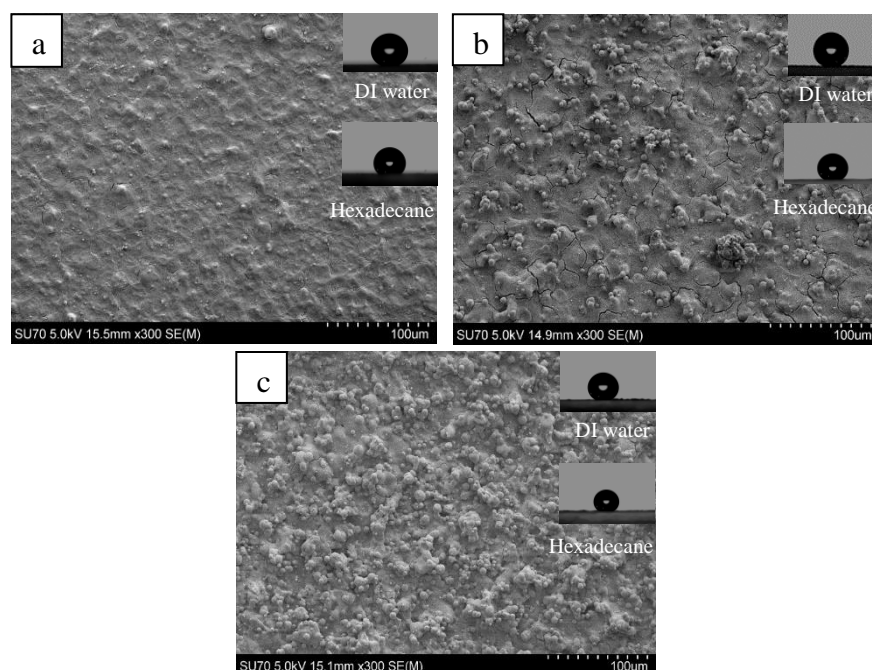


Figure 3.4: SEM images of textured surfaces fabricated with different SiO₂ concentrations: (a) 8 mg/mL, (b) 15 mg/mL, and (c) 25 mg/mL.

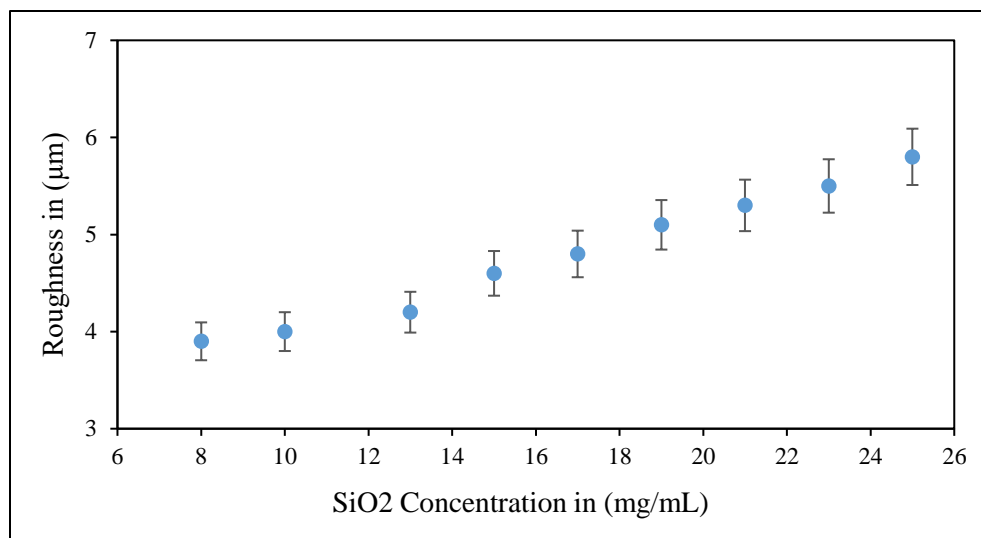


Figure 3.5: Roughness of surfaces fabricated with different SiO₂ concentrations.

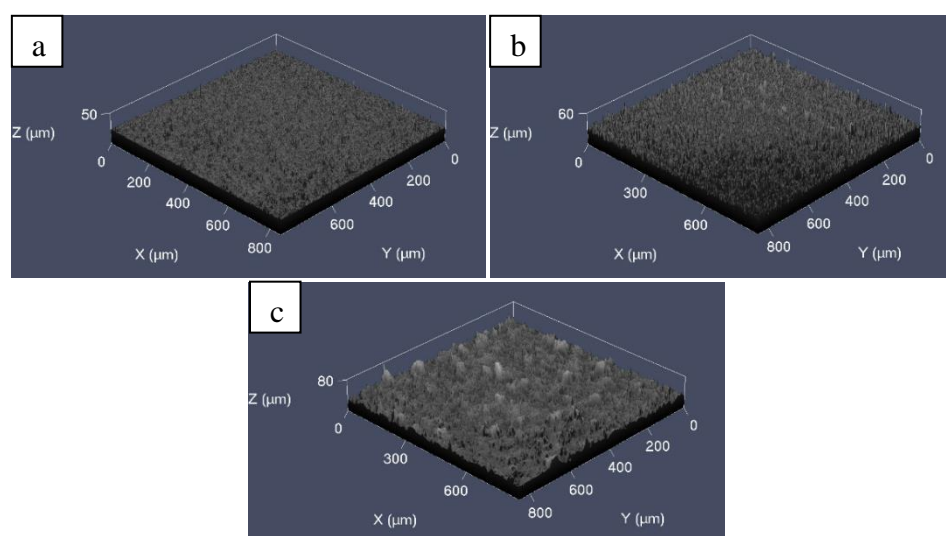


Figure 3.6: LSM 3D images of textured surfaces fabricated with different SiO₂ concentrations: (a) 8 mg/mL, (b) 15 mg/mL, and (c) 25 mg/mL. Each picture was constructed of at least 360 slices, 1 interval, and 375 μm range.

As the SiO₂ concentration increases, the sprayed surface becomes rougher indicated by the formation of larger agglomerates on the surface. Multi-level re-entrant structures are created on the agglomerates, intertwined with overhangs of random protrusions throughout the sample's surface. Figure 3.5 shows surface root mean square (RMS) roughness with the change of silica concentration measured by LSM, in which the surface roughness increases monotonically due to

the deposition of larger agglomerates when spraying with higher concentrations. Figure 3.6 shows LSM 3D pictures with scanning area of $850\ \mu\text{m} \times 850\ \mu\text{m}$ of the coated samples using different silica concentrations. The standard deviation of each reported roughness measurement is $\sim 1\ \mu\text{m}$. While the microscale roughness was characterized by LSM due to its capability of large scanning areas, the nanoscale roughness was characterized by AFM from several $1\ \mu\text{m} \times 1\ \mu\text{m}$ scanning areas of the different surfaces. The RMS roughness of samples made with 8 mg/mL, 15 mg/mL, and 25 mg/mL concentrations were 19.5 nm, 26.1 nm, and 35.3 nm respectively with a standard deviation of $\sim 1\ \text{nm}$ (Fig. 3.7). It is worth noting that within this $1\ \mu\text{m}^2$ scanning area, the nano roughness was calculated from only a $300\ \text{nm} \times 300\ \text{nm}$ area on the upper part of the agglomerates without taking the valleys areas into account.

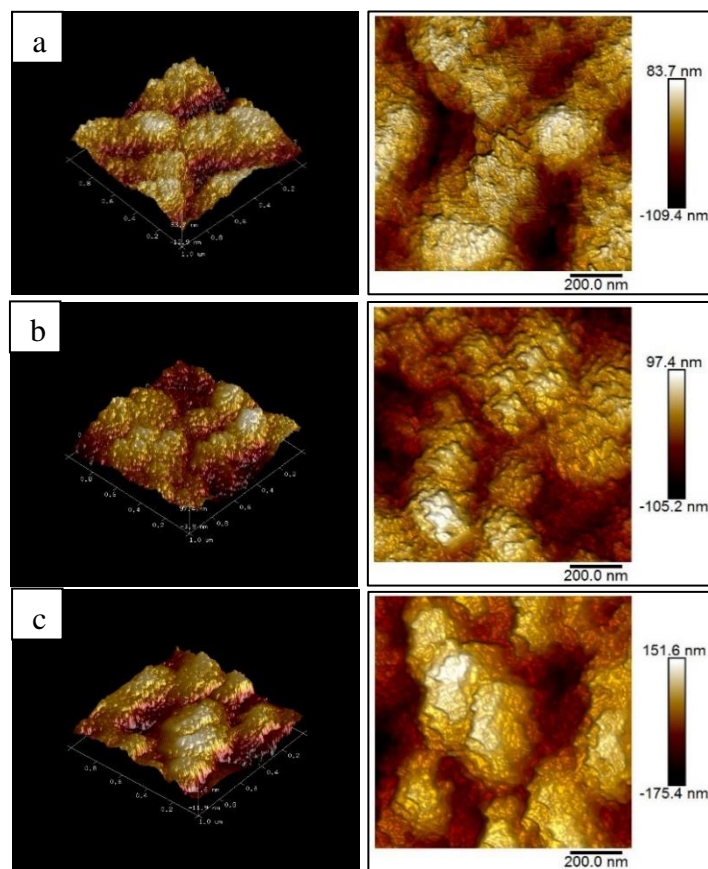


Figure 3.7: AFM 3D images of textured surfaces fabricated with different SiO_2 concentrations: (a) 8 mg/mL, (b) 15 mg/mL, and (c) 25 mg/mL.

This random hierarchical micro/nano roughness and re-entrant structures combined with the low surface energy treatment of FDTS render excellent SHP and SOP wetting properties.

Figure 3.8 shows the measured DI water and hexadecane apparent contact angles as a function of different silica concentrations. The ellipse fitting was used for each test and the standard deviation of DI water and the hexadecane were $\sim 1^\circ$ and $\sim 2^\circ$ respectively.

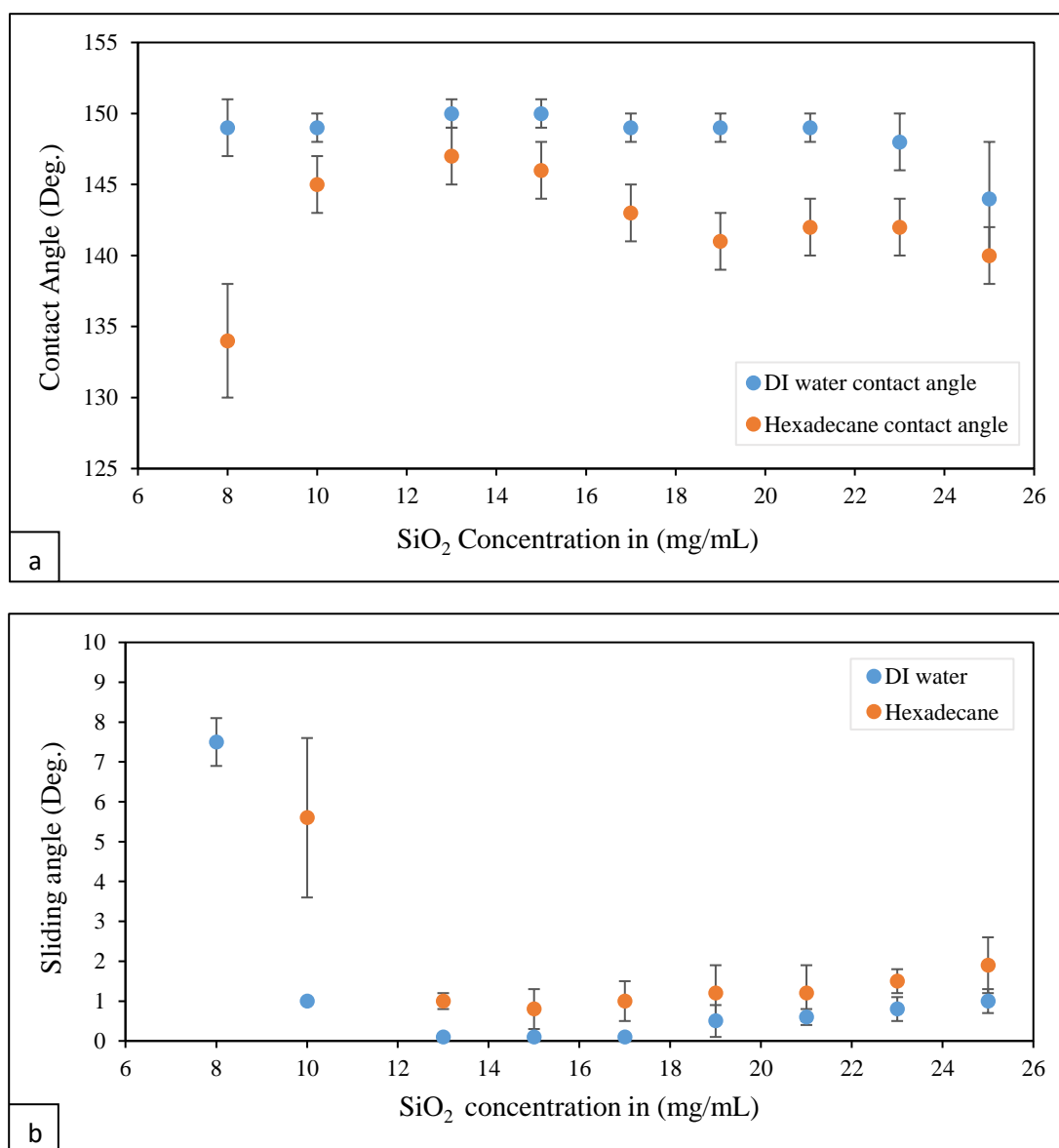


Figure 3.8: (a) apparent contact angles of samples fabricated with different SiO₂ concentrations, (b) sliding angles of samples fabricated with different SiO₂ concentrations.

For all the concentrations studied, water contact angles keep close to 150° and very low sliding angles, except the samples fabricated of 8 mg/mL concentration. It has a high contact angle with DI water (149°), but the sliding angle is much higher compared to those fabricated with higher SiO_2 concentrations. On all the samples, Hexadecane contact angles are about $4\text{-}8^\circ$ lower than those of water except the sample of 8 mg/mL, where the contact angle of 134° with a stuck hexadecane droplet and pinned contact line during tilting indicate a fully wetting Wenzel state or an intermedium wetting state between Wenzel and Cassie-Baxter state.⁷²

The loss of superoleophobicity could be explained by the low surface roughness obtained at low silica concentration by which the air pockets are replaced with liquid of low surface tension like the hexadecane, and a transition toward Wenzel fully wetting state occurs. Above a concentration of 15 mg/mL, the hexadecane apparent contact angle starts decreasing along with rising tilting angles. This could be attributed to a decreased amount of air trapped in-between the larger agglomerates leading to a stronger adhesion on those surfaces.

One of the goals of the present study is to discover how surface wettability changes with silica concentration and limits of the silica concentration range in which the sample retains superhydrophobicity and superoleophobicity. Based on the surface wetting results obtained from the fabricated samples, the optimum silica concentration range is determined between 13 mg/mL and 17 mg/mL. Table 3.1 presents the liquid wetting data on the fabricated samples, in which all the samples except the one created of 8 mg/mL silica concentration have very low sliding angles and contact angle hystereses with DI water and hexadecane.

Since water and hexadecane droplets are very mobile on the fabricated samples with high apparent contact angles, it was very difficult to measure the sliding angle for DI water and hexadecane repeatedly, and the same is true in measuring the advancing and receding contact angles.

Table 3.1: Contact angle, sliding angle, and contact angle hysteresis of DI water and hexadecane for samples fabricated with different SiO₂ concentrations.

SiO ₂ Concentration	Contact angle		Sliding angle		Contact Angle hysteresis	
	DI water	Hexadecane	DI water	Hexadecane	DI water	Hexadecane
8 mg/mL	149°	134°	7.5°	N/A	8.3°	N/A
10 mg/mL	149°	145°	1°	5.6°	1.4°	6.4°
13 mg/mL	150°	147°	0.1°	1°	0.5°	1.9°
15 mg/mL	150°	146°	0.1°	0.8°	0.6°	1.5°
17 mg/mL	149°	143°	0.1°	1°	0.6°	1.6°
19 mg/mL	149°	141°	0.5°	1.2°	1°	2.1°
21 mg/mL	149°	142°	0.6°	1.2°	1.2°	2.3°
23 mg/mL	148°	142°	0.8°	1.5°	1.5°	2.9°
25 mg/mL	144°	140°	1°	1.9°	1.7°	3.7°

Although the hexadecane wetting properties degrades when concentration increases beyond 15 mg/mL, indicated by decreasing apparent contact angles and increasing tilting angles, the surfaces fabricated at 25 mg/mL still exhibit an ultra-high contact angle of 140° and fairly low tilting angle of 3.7°. The upper limit of the silicon dioxide concentration test seems limited to the following processing obstacles: first, at concentrations higher than 35 mg/mL, not all the particles were mixed with the acetone and thus the solution is not homogenous. Second, this nonhomogeneous solution is not easy to spray; and if sprayed, it generates non-uniform coatings due to nozzle clogging issues. However, all the fabricated samples from such a thick silica solution still retain the self-cleaning property. We didn't include all the contact angle and the sliding angle data for silica concentrations higher than 25 mg/mL because the difference in the contact and sliding angle were minimal as compared to the 25 mg/mL silica concentration.

The fabricated samples possess excellent surface wetting properties when the surface roughness is between 4 – 6 μm; nonetheless, they have high affinity to catch the low surface tension liquids when the surface RMS roughness is below 4 μm (Fig. 3.5). Additionally, we speculate that the increase of silica amount in the solution (higher than 35 mg/mL), generates coarser coatings with microscale agglomerations by which the surface area fraction increases and the transition from the

Cassie-Baxter to Wenzel state may occur. Thus, the contact and the sliding angles decrease because of the increase in the solid area fraction at liquid-solid-air interface by which the liquid droplet is affected and hindered from bouncing and rolling off the sample.

Figure 3.9 shows the direct effect of surface roughness obtained by spraying different SiO_2 suspension concentrations on surface wettability that is represented by the contact angles of DI water and hexadecane.

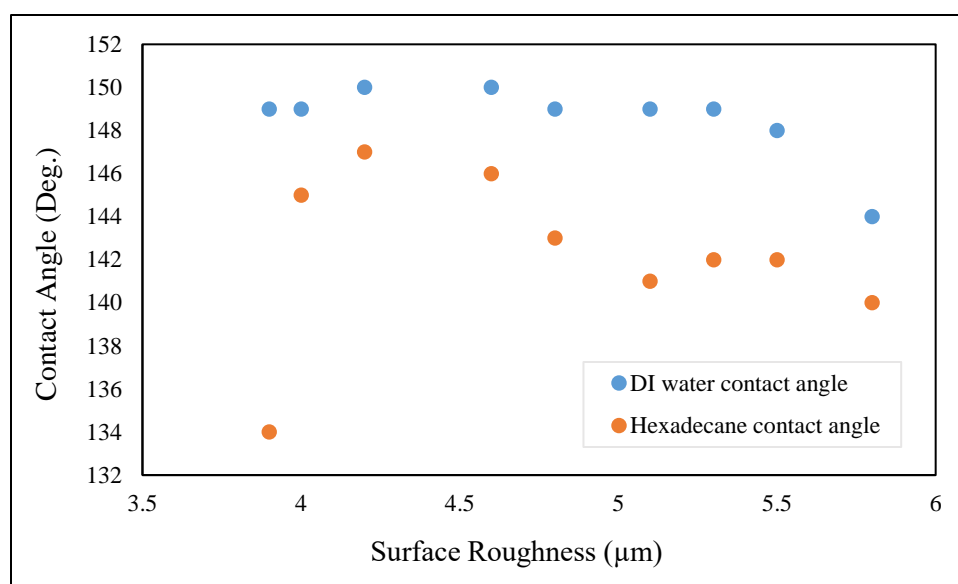


Figure 3.9: Effect of surface roughness on surface wettability for samples fabricated with different SiO_2 concentrations.

3.4.2 Effect of silicon dioxide agglomerate particle size on surface wettability

In this study, a comparison between two types of SiO_2 suspensions, i.e., directly-dispersed suspension from SiO_2 powder and surfactant-assisted suspension, have been conducted. Both have a primary particle size of 13 nm; however, they tend to form different agglomerates' size when they are mixed with acetone. While the 15 mg/mL silicon dioxide powder has agglomeration size

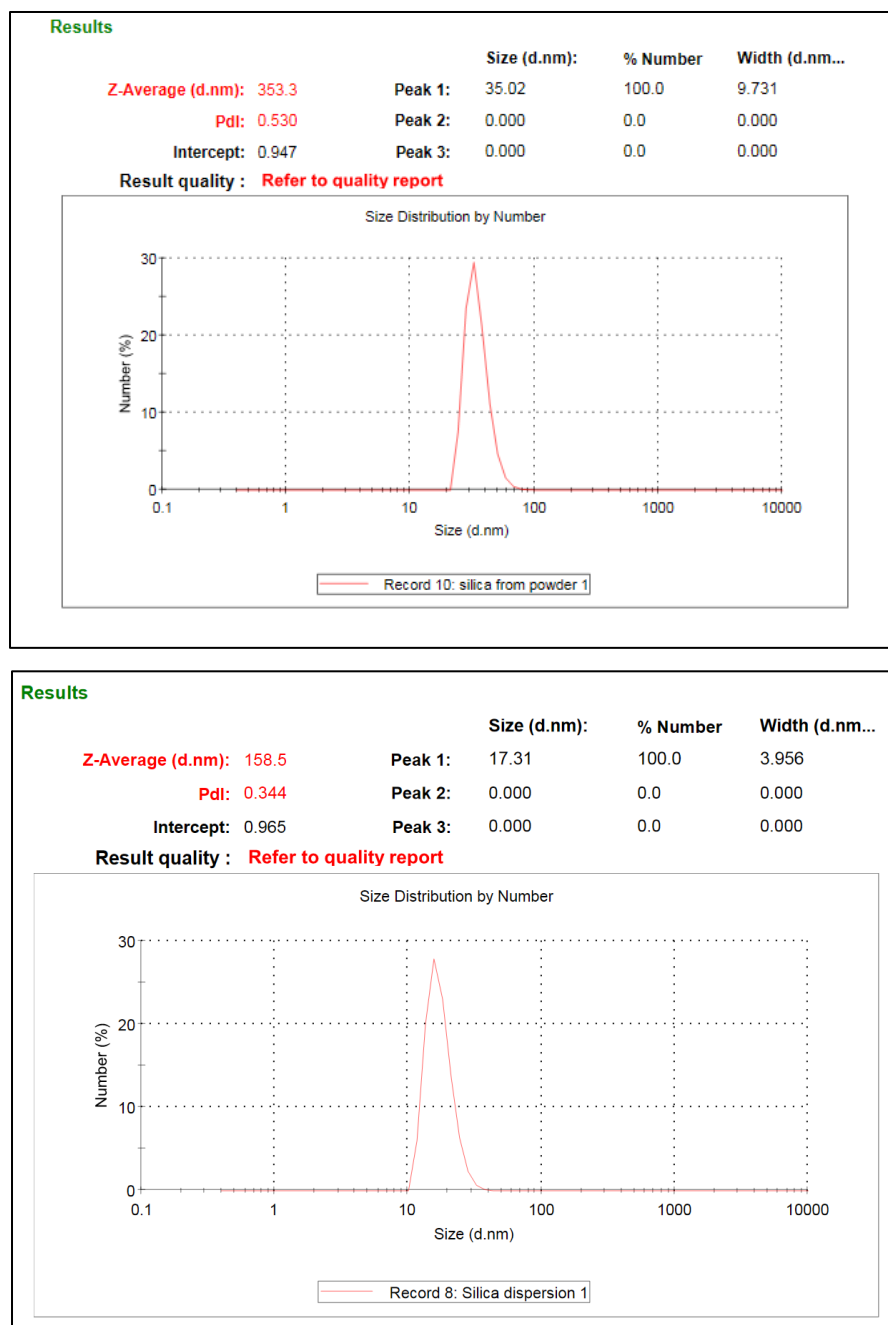


Figure 3.10: Agglomerate particle size comparison between the directly-dispersed and surfactant-dispersed suspensions.

of 350 nm with acetone, the same concentration of SiO₂ dispersion (AERODISP W 7512 S, Evonik Industries) has agglomeration size of 160 nm when mixed at the same concentration. Figure 3.10 shows the difference between directly-dispersed and surfactant-assisted suspensions measured by

Malvern Zetasizer, where the peak indicates the particle diameter size based on the number-average method (Z-average), and the PDI is the Polydispersity Index. The smaller the PDI number becomes, the closer the suspension to form monodispersed layers. As expected, the surfactant-assisted suspension provides smaller agglomerate particles with a narrower size distribution.

The samples were prepared using both suspensions of 15 mg/mL SiO₂ concentration and characterized following the procedures described in earlier sections. This comparison test indicates that larger agglomerates in suspension is favorable in producing SHP and SOP surfaces with random hierarchical roughness. Figure 3.11 displays the morphology difference obtained by spraying directly-dispersed and surfactant-dispersed SiO₂ suspensions. Each sample was fabricated by spraying 3 μL of 15 mg/mL suspension concentration.

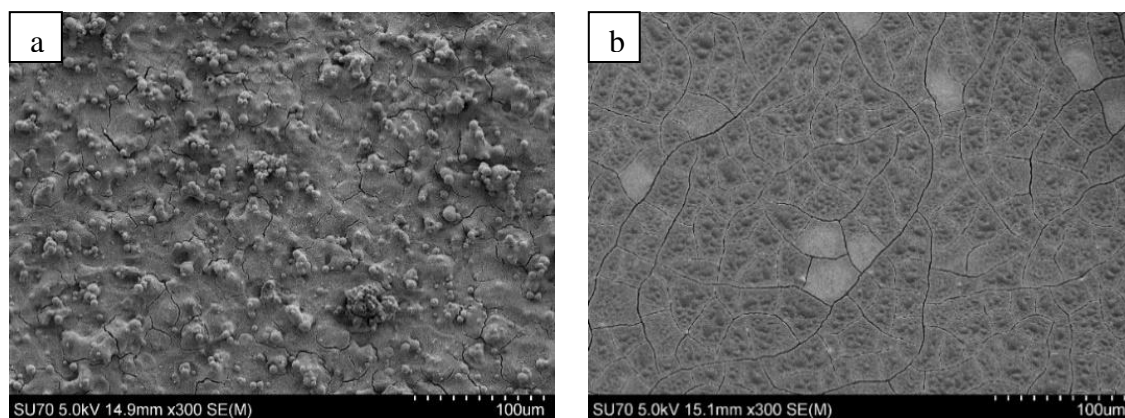


Figure 3.11: SEM images of textured surfaces fabricated with (a) directly-dispersed and (b) surfactant-dispersed suspensions.

Figure 3.12 show water and hexadecane contact angle measurements on the samples fabricated with both suspensions. Water contact angles of $\sim 150^\circ$ and sliding angles of $< 1^\circ$ are obtained on both samples, while hexadecane displays much lower contact angles on the samples that are fabricated of surfactant-assisted suspension.

Similarly, Figure 3.13 depicts the sliding angle comparison between both silica suspensions. Sliding angle measurements of hexadecane also confirms the stronger adhesion on the samples fabricated of surfactant-assisted suspension, indicated by the fact that the hexadecane droplet doesn't slide even if the tilting base of the goniometer is tilted up to 90°. That is why the sliding angle of hexadecane on this particular sample is not shown in Fig. 3.13.

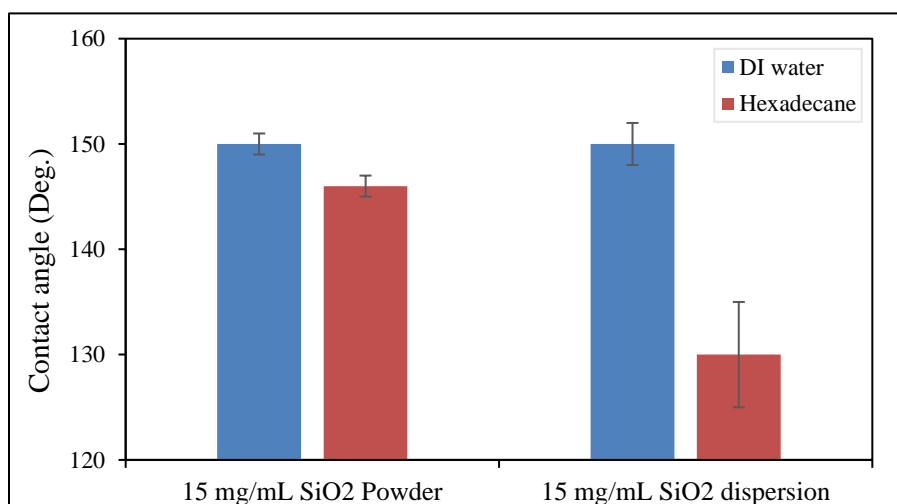


Figure 3.12: Contact angle measurements of textured surfaces fabricated with directly-dispersed and surfactant-dispersed suspensions.

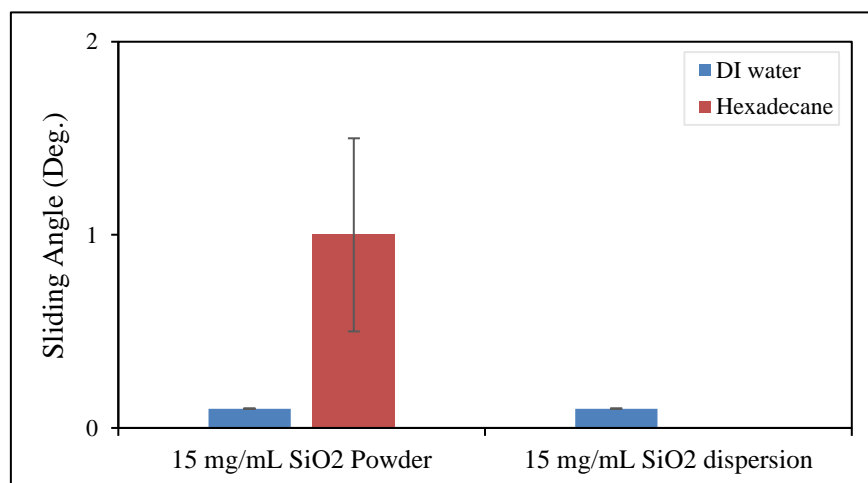


Figure 3.13: Sliding angle measurements of textured surfaces fabricated with directly-dispersed and surfactant-dispersed suspensions.

As the re-entrant structure with multiscale surface roughness is the preferred way to obtain self-cleaning property, creating such textured surfaces with dual surface roughness through spraying the silicon dioxide dispersion is not achievable. This could be attributed to the agglomeration size that is not large enough to produce such a coarse surface topography (Fig. 3.11).

3.4.3 Surface transparency

Transparent super liquid repellent surfaces are essential in many disciplines such as windshields and solar cells.^{69,73} For this purpose, the fabricated samples with different SiO₂ concentrations were further investigated in order to get better understanding of coatings' behavior with respect to light. The main factors in engineering transparent SHP and SOP coating are the coating thickness and the size of silica particle agglomerates.⁵⁵ As the SiO₂ concentration increases, the surface roughness increases as well (Fig. 3.5). Figure 3.14 illustrates the monotonically relationship between the size of silica agglomerates on the coating surface with respect to the increase in suspension concentration.

In this study, UV/ vis spectrophotometer (Thermo Scientific Evolution 200) is utilized to examine transparency of the fabricated SHP and SOP coatings. Figure 3.15 demonstrates the transmittance test conducted on the 8 mg/mL, 15 mg/mL, and 25 mg/mL silica coated samples as compared with the transparency of a bare glass slide.

All the sample show a similar trend between 300 nm and 800 nm wavelength range. If the SiO₂ concentration is low, the samples display high transparency as compared to the bare glass slide e.g., above 85% for the visible lights on the samples of 8 mg/mL. However, the light gets scattered and attenuated if the coating has highly concentrated SiO₂ since the transmittance is inversely proportional to coating thickness and surface roughness. On the other hand, by producing coatings

with high concentrated silica agglomerates, the absorption of UV light is enhanced. This feature of blockage or filtering the UV light find benefits in some engineering applications.

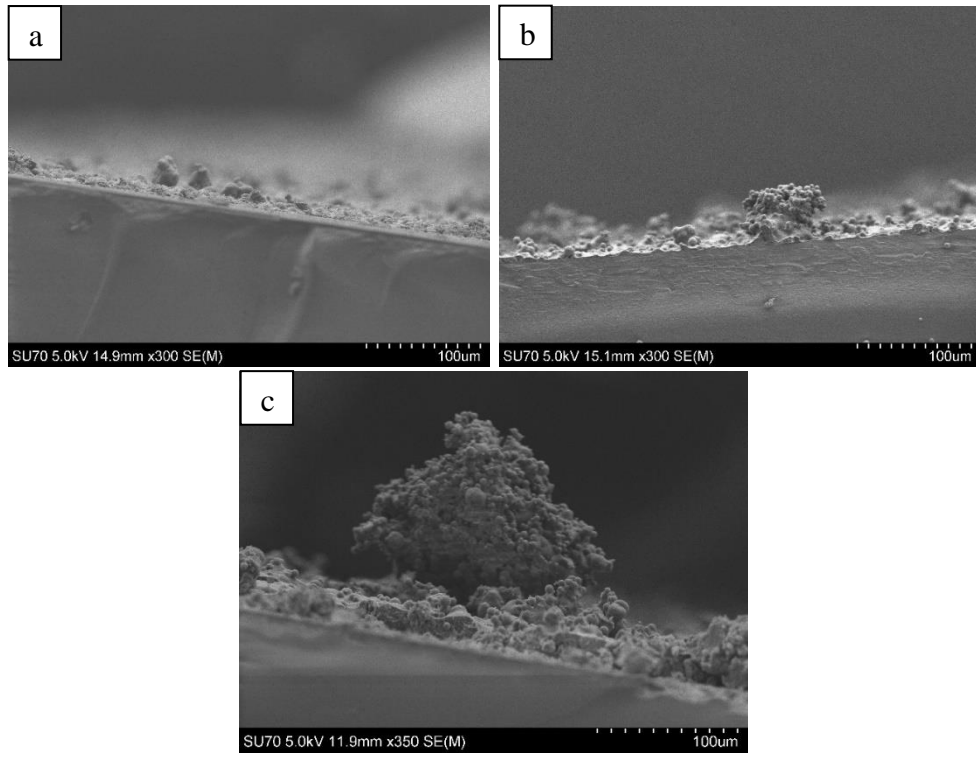


Figure 3.14: Cross-section of textured surfaces fabricated with different SiO₂ concentration: (a) 8 mg/mL, (b) 15 mg/mL, (c) 25 mg/mL.

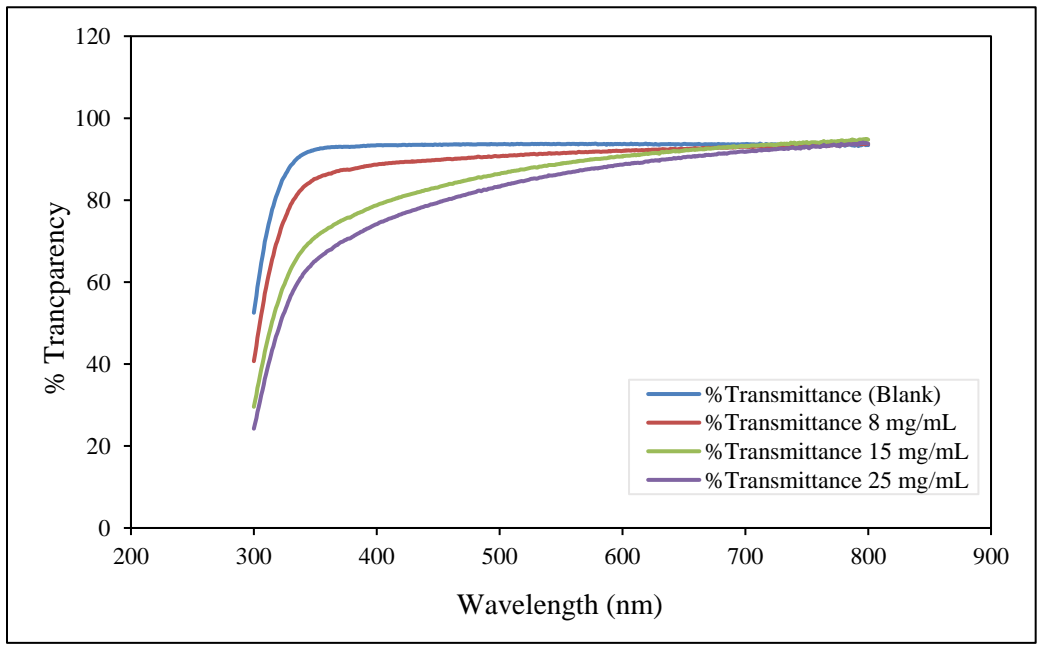


Figure 3.15: Transparency of textured surfaces fabricated with different SiO₂ concentrations.

3.5 Conclusion

In this chapter we demonstrated the fabrication of SHP and SOP coatings with high apparent contact angles and very low sliding angles. The samples were coated with different SiO_2 suspensions at various concentrations to study the effect of surface roughness on surface wettability. The experimental findings indicated that the superhydrophobicity and the superoleophobicity were achieved by combining the multiscale surface roughness that is represented by the re-entrant structure and the low surface energy obtained by chemically treating the surface. As the SiO_2 concentration increases, the surface roughness is found to increase as well. This increase in surface roughness is attributed to the increase in silica agglomeration size at higher silica concentrations, which is in turn, affects the contact angles and the sliding angles. In this study, the upper limit of SiO_2 concentration test has been specified based on the difficulty in mixing and spraying the suspension.

The fabricated samples highlighted the important role of the re-entrant structure by which the wetted area are drastically decreased leading to outstanding surface wetting properties. The findings are further corroborated with the low contact angle hysteresis for both DI water and hexadecane. The results of this study also revealed that creating SOP surfaces by spraying surfactant-dispersed SiO_2 suspension is unattainable because of its corresponding low agglomerate size. Furthermore, the fabricated samples showed high transparency to visible lights as compared to a bare glass slide when substrates were coated with low concentrated SiO_2 dispersion.

CHAPTER 4 Superhydrophobic and Superoleophobic Surfaces by Mask-assisted

Electrospray

4.1 Introduction

Electrospray is a low-cost, facile, and effective coating process produced by spraying liquids onto a substrate through electrostatic interactions to form a functional micro/nano structured coating layer.^{35,74} It can be considered as a function of solution parameters (viscosity, solvent conductivity, and molecular weight) and working conditions (applied voltage, working distance, material flow rate, and nozzle diameter).^{51,75} The electrospray was first reported in 1914 by Zeleny through applying high voltage potential between a grounded substrate and a conductive needle that is fed by pumped liquid at very low flow rates.⁷⁶⁻⁷⁸ The pumped liquid is forced to break up into fine droplets under the influence of the applied voltage that generates a stable cone-jet (Taylor cone) if liquid properties and operating parameters are carefully tuned.⁷⁵ The applied charge concentrates on the droplet meniscus at tip of the nozzle by which liquid droplets get elongated and disintegrate to nanoscale charged particles. This could be explained by Rayleigh limit when the accumulated charge overcomes the surface tension because of the coulombic repulsive force.⁷⁹ Various jetting modes have been observed by increasing the applied voltage such as dripping, pulsating, cone-jet, tilted-jet, twin-jet, and multi-jet.⁸⁰ The dripping mode occurs when the applied electric force is small as compared to hydrodynamic forces (surface tension, viscosity, and gravity).⁸¹ By ramping the voltage up the dripping mode turns to pulsating mode. Further increasing of the applied voltage causes the jet to be stable (Taylor cone jet). After the cone-jet, a tilted then a multi-jet occurs by applying a higher voltage.⁸⁰⁻⁸² Electrospray is indispensable tool for numerous applications such as thin film deposition,^{52,53,79} bio-applications,⁷⁶ spray painting,⁸³ and micro-patterning of particles and cells.^{84,85}

In this study, electrospray technique has been employed to fabricate SHP and SOP surfaces with multiscale roughness with a two-fold objective: First, to engineer SHP and SOP surfaces with random hierarchical roughness; and second, to fabricate SHP and SOP surfaces with patterned multiscale roughness and enhanced surface properties. Surfaces with random hierarchical roughness were created by electrospraying the SiO₂ nanoparticles on a glass slide substrate for various spray times, while a PTFE coated stainless steel mesh was utilized as a mask to fabricate surfaces with patterned multiscale roughness. In addition, the deposition efficiency of the electrospray is also of interest.

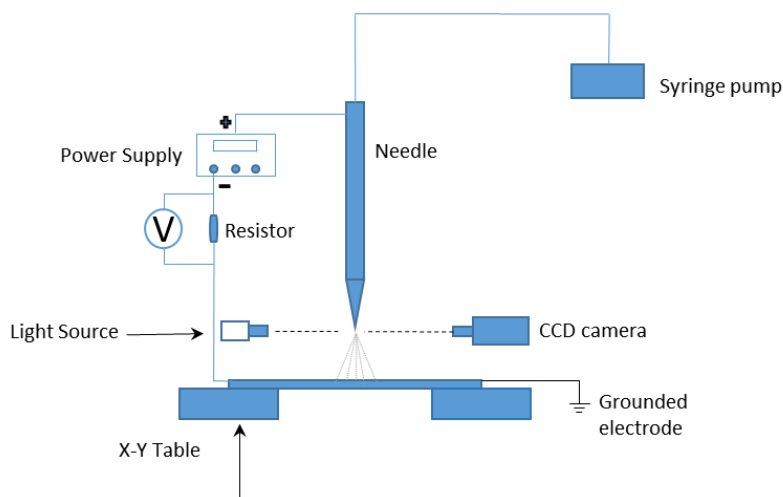


Figure 4.1: A schematic of the electrospray experimental setup.

4.2 Material and methods

4.2.1 Apparatus setup

A 250 μ L syringe from Hamilton is connected to 0.5 mm inner diameter (ID) stainless steel needle by a PTFE tubing (1.6 mm ID) and flangeless fitting from IDEX Health and Science LLC. The syringe is attached to a fully programmable double syringe pump (NE-4000) from New Era Pump System Inc. A vacuum sample holder is attached to a fine-adjust cross-slide table with two

T-slots (45.7-1.6 cm x 15 cm Table Size) from McMaster Carr. The cross table is grounded (as well as the sample holder) and a high voltage is applied to the needle by a power supply (Bertan Series 230) from Spellman. A light source (Fiber-Lite MI-152) with high intensity illumination from Dolan-Jenner and a color USB camera from Edmond (EO-2013 C LE) with 18 fps were used to monitor the meniscus and jetting modes (Fig. 4.1).

4.2.2 Materials and textured surface fabrication

4.2.2.1 Fabrication of surfaces with random hierarchical roughness

In this study, a 1 mm thick Fisher Scientific microscope glass slide was cut into dimensions of 2.5 x 3.8 cm and used as a substrate to fabricate SHP and SOP surfaces with random surface roughness. The substrate was first cleaned by following the order of hot soapy water, Acetone, and Isopropanol then rinsed with DI water and dried by clean air. The clean glass slide was further cleaned by plasma cleaner (HARRIC PLASMA PDC-001-HP-115V) for 5 minutes to assure that the substrate was thoroughly cleaned. An excessive cleaning process is crucial for generating super liquid repellent surfaces, because any contamination existing on the surface affects the adhesion of the coating layer with the substrate, resulting in wetting failure on the defective locations. Polydiallyldimethylammonium chloride (PDADMAC, 20 wt % in water, Aldrich) was diluted in DI water to obtain 52 mg/mL PDADMAC concentration. A thin layer of the PDADMAC was spin coated onto the previously cleaned glass slide by a spin coater (SCS 6800 spin coater from KISCO) at 3000 rpm. SiO₂ dispersion (AEROSIL W 7512 S, Evonik Industries) with a primary particle size of 13 nm was diluted with Isopropanol to 15 mg/mL concentration for electrospray process. This specific solution concentration was chosen based on SiO₂ concentration test in Chapter 3. It should be mentioned that getting a stable cone-jet using the isopropanol alone is not attainable unless a small amount of nitride acid is added to the solution to increase electrical conductivity of

the suspension. In this study, the electrical conductivity is tuned to be around 38-40 $\mu\text{S}/\text{cm}$. Producing clean and uniform coatings by electro spray requires careful adjustment of the applied voltage and its correspondent material flow rate. Figure 4.2 represents the operating window in which a stable cone-jet is achievable, i.e., in-between the multi-jet mode and pulsating mode; other than that, the charged particles will not be uniformly deposited onto the substrate.

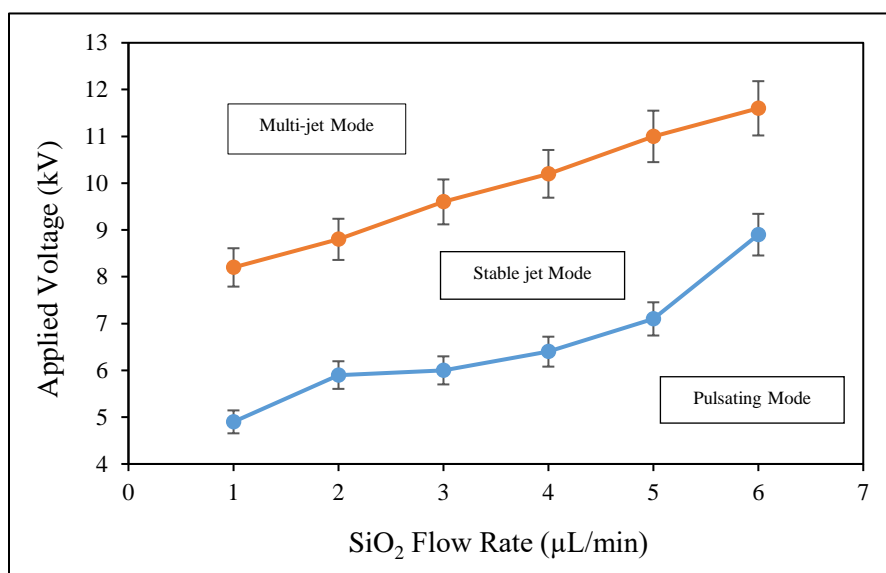


Figure 4.2: Operating window (stable cone-jet region) along with different electro spray modes.

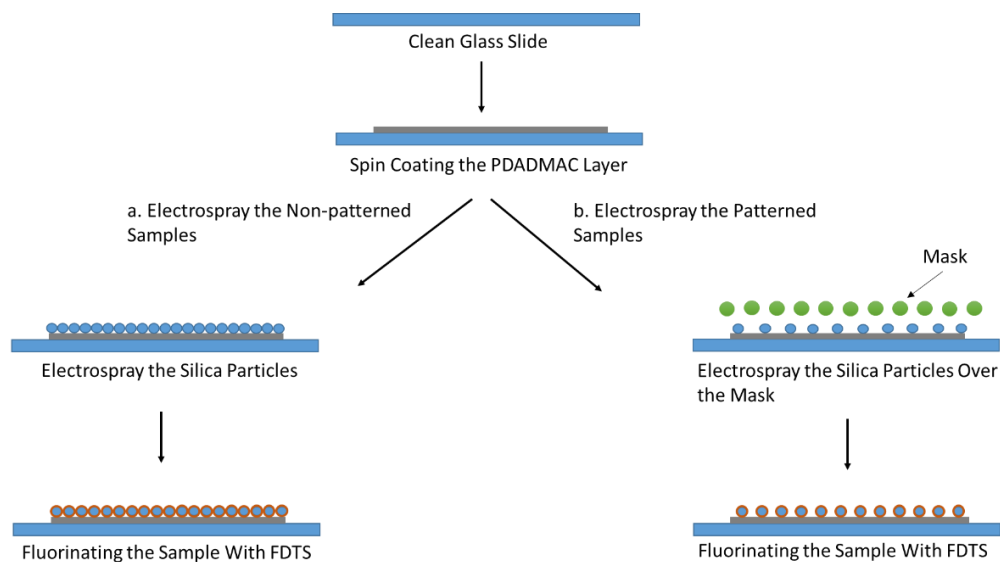


Figure 4.3: Electro spray scheme: (a) surfaces with random hierarchical roughness, (b) surfaces with Patterned multiscale roughness.

Figure 4.3a illustrates the fabrication procedure for SHP and SOP surfaces with random surface roughness. SiO₂ suspension was electrosprayed onto the prior PDADMAC-coated samples for various time periods. The working distance, the applied voltage and the suspension flow rate are 5 cm, 7-9 kV DC, and 3 μL/min, respectively. For the samples produced at a 15-min spray time and longer, a second layer of 0.2 mL of 8 mg/mL PDADMAC solution is air sprayed on the top of the coating, followed by a 5-min electrospray deposition. The benefit of this step is twofold: Firstly, this second PDADMAC layer serves as a protecting layer that holds all the silica particles in place, which significantly minimizes the amount of loose silica particles; Secondly, this PDADMAC coating acts as a base layer for the subsequent electrospray of SiO₂ that only lasts for 5 min.

The surface treatment of FDTD fluorination follows procedures described in Chapter 3.

4.2.2.2 Fabrication of patterned surfaces with multiscale roughness

The procedure for generating patterned coatings with microscale roughness of SiO₂ nanoparticles on a substrate is a little bit different than that mentioned in the previous section. To fabricate the pillar-patterned samples, we have utilized a PTFE coated stainless steel mesh as a mask with a 36 μm wire diameter and a 79 μm center-to-center distance (Fig. 4.3b). A 1 mm glass slide that is cut into same dimensions as explained in the previous section was used as a substrate. The mesh was attached to the glass slide at various gaps (ranging from 70 to 500 μm) and should be perfectly insulated from the ground so that the charged silica particles find their way to deposit on the grounded substrate, instead of on the mesh. A DC voltage of 10-12 kV is applied to the needle, and 2 kV is applied to the mesh which reduces the amount of charged particles deposited on the mesh and increases the deposition density of the particles in the desired spots (openings of the mesh). A 3 μL/min flow rate of SiO₂ dispersion and 90 min spray time were used to make

patterned multiscale pillars. Then the mesh was removed, followed by electro spraying SiO₂ suspension for 10 min in order to overlay a nanoscale roughness on the microscale pillars and to cover any exposed area of the PDADMAC-coated substrate.

The surface treatment of FDTS fluorination follows procedures described in Chapter 3.

4.2.3 Contact angle measurements and surface morphology characterization

The contact and sliding angle measurements were conducted on a goniometer (OCA 15 CE) from Dataphysics. A 250 μ L Hamilton syringe with a 0.21 mm stainless steel needle was used. The syringe type and volume in addition to the needle size should be specified in the goniometer's software. For static contact angle measurements, a 3 μ L of DI water and hexadecane were gently dispensed on the testing substrate. Each reported data was an average of five independent measurements on different sample locations. The ellipse fitting and the Young-Laplace fitting were used for each test and the standard deviation for DI water and hexadecane were $\sim 1^\circ$ and $\sim 2^\circ$ respectively. The sliding angle is defined as the minimum slope measured in degrees at which the liquid droplet starts to slide or roll. It is customary to use a 10 μ L droplet size in tilting angle measurements with tilting rate of 1 %/s.⁶ The standard deviation for tilting angle measurements were $\sim 0.1^\circ$ for DI water and $\sim 0.2^\circ$ for hexadecane which give an indication about our success in fabricating excellent superhydrophobic and superoleophobic surfaces. The ultra-high resolution HITACHI SU-70 FE-SEM with 5 kV and 15 mm scanning distance were used to characterize the morphology of the fabricated textured surfaces. To minimize charging effect of the silica particles, the samples were coated with platinum using the (Denton Vacuum Desk V platinum sputter) for 60 sec. Furthermore, the Zeiss 710 Laser Scanning Microscope (LSM) and the Burker Dimension Icon Atomic Scanning Microscope (AFM) were also implemented for further surface characterization like three-dimensional morphology and surface roughness.

4.3 Results and discussion

4.3.1 Superhydrophobic and superoleophobic surfaces with random hierarchical roughness

The textured surfaces in this study were created using the electrospray technique to spray nanoparticles of SiO₂ on a glass slide followed by chemical treatment with FDTS to reduce the surface energy. The glass slide and the silica particles are negatively charged while the PDADMAC is positively charged by which the coating robustness is enhanced because of the electrostatic interactions.¹⁸ The homogenous SiO₂ solution with primary particle size of 13 nm, tends to form bigger agglomerates (~ 160 nm) when the silica particles are mixed with isopropanol. Figure 4.4 shows the dynamic light scattering (DLS) results of the 15 mg/mL SiO₂ dispersion.

The change of spray time is intended to increase the surface roughness which in turn gives the desirable re-entrant/overhang structure. Figure 4.5 shows the change in surface morphology of the silica coated samples with various spray time.

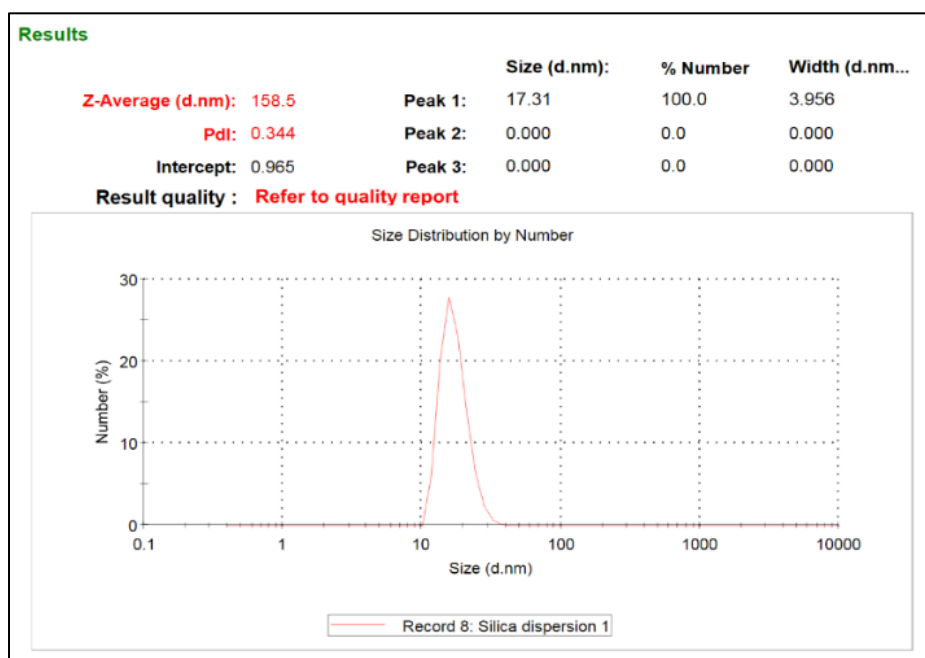


Figure 4.4: Particle size measurement of a SiO₂ suspension (15 mg/mL) by dynamic light scattering.

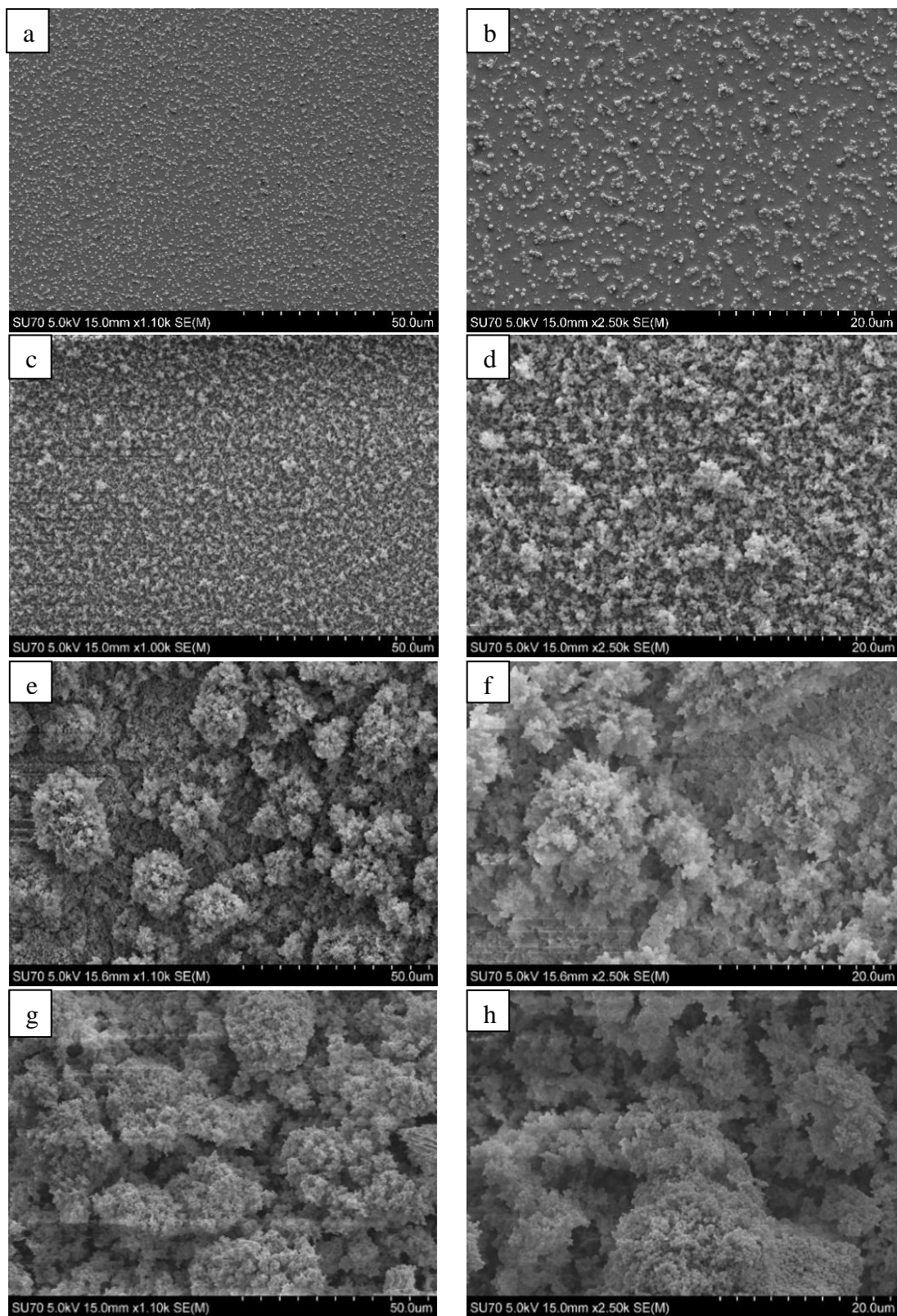


Figure 4.5: SEM images of textured surfaces with hierarchical roughness fabricated at different spray times: (a) and (b) 2 min spray time, (c) and (d) 5 min spray time, (e) and (f) 45 min, (g) and (h) 90 min spray time.

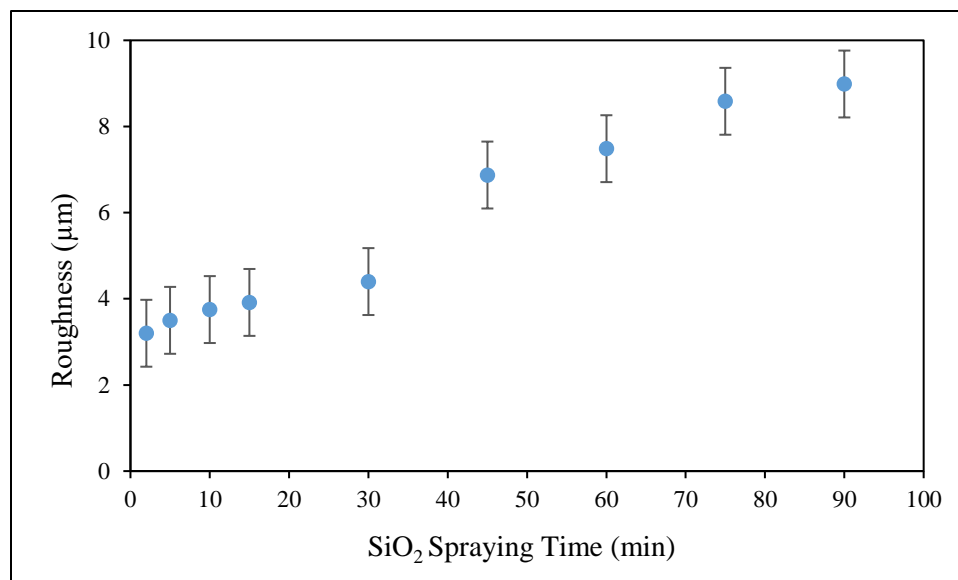


Figure 4.6: Roughness of surface with hierarchical multiscale structure fabricated at various electro spray times.

In order to better understand the relationship between the super liquid repellent property and the surface geometry, the surface topography on those textured surfaces were examined in more detail. As the spray time increases, the surface roughness increases as well (Fig. 4.6). This means that more silica agglomerates are deposited that provide the preferred re-entrant/overhang structure to successfully prevent DI water and hexadecane from wetting the surface.

Figure 4.7 shows LSM 3D pictures with a scanning area of 850 x 850 μm using the 10x lens of different coated samples with various coating periods. Each picture was constructed of at least 360 slices, 1 interval, and 375 μm range. The standard deviation of each roughness measurement ~ 2 μm.

In this study, LSM is utilized to characterize the microscale roughness by scanning large surface areas, while AFM is used to measure the nanoscale roughness of silica agglomerates from scanning small areas on the surface. Figure 4.8 displays 3D images obtained from AFM that shows a similar trend to that obtained from LSM. The RMS surface roughness of samples fabricated at spraying

times of 5, 45, and 90 min spray times are 20.8, 30, 37 nm respectively with a standard deviation of ~ 2 nm. The AFM roughness measurement was an average of five independent measurements at different sample locations with a scanning area of $1 \mu\text{m} \times 1 \mu\text{m}$. It is worth noting that within this $1 \mu\text{m}^2$ scanning area, the nano roughness was calculated from only a $300 \text{ nm} \times 300 \text{ nm}$ area on the upper part of the agglomerates without taking the valleys in the whole $1 \mu\text{m} \times 1 \mu\text{m}$ scanning areas into account. Thus, we conclude that surface roughness is positively and linearly associated with spray time. In fact, these obtained agglomerates are crucial for rendering a favorable non-wetting Cassie-Baxter state by preventing DI water and hexadecane from wetting the surface. However, care should be taken when spraying liquid with big agglomerates. The larger the agglomerates become, the more difficult it will be to electro-spray due to nozzle clogging issues.

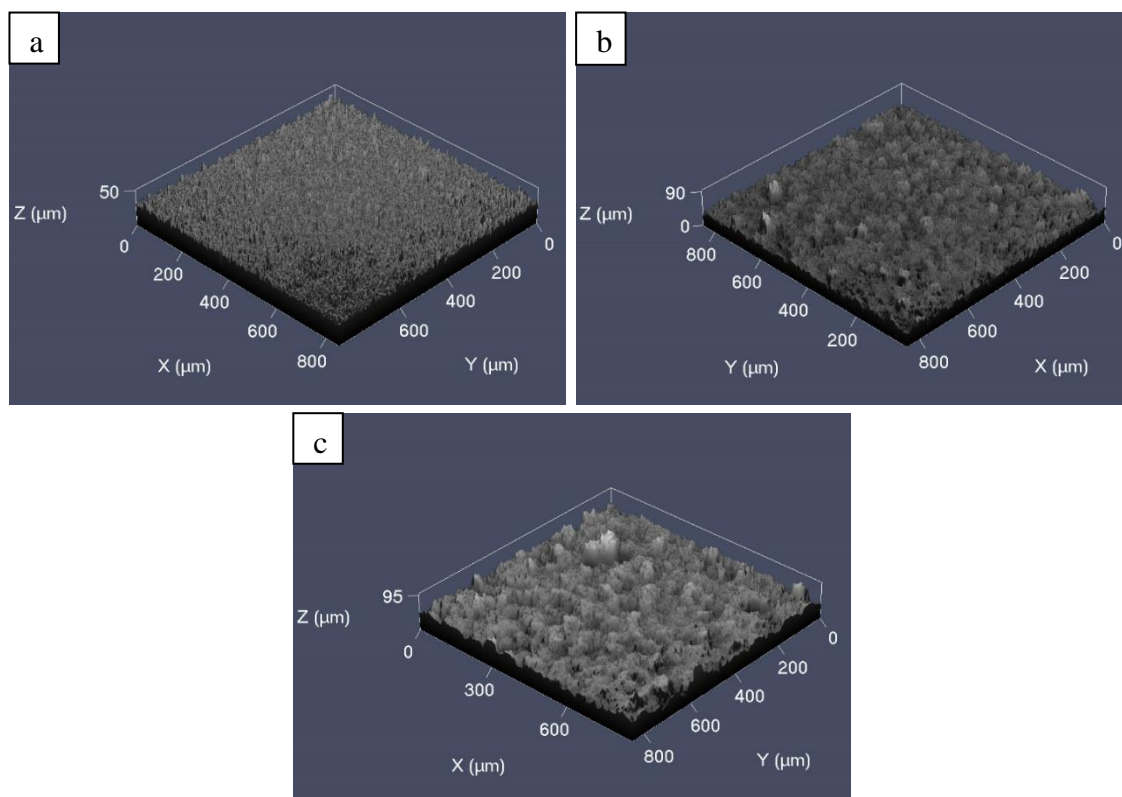


Figure 4.7: LSM 3D images of samples with random hierarchical roughness sprayed at various spray times: (a) 5 min, (b) 45 min, (c) 90 min.

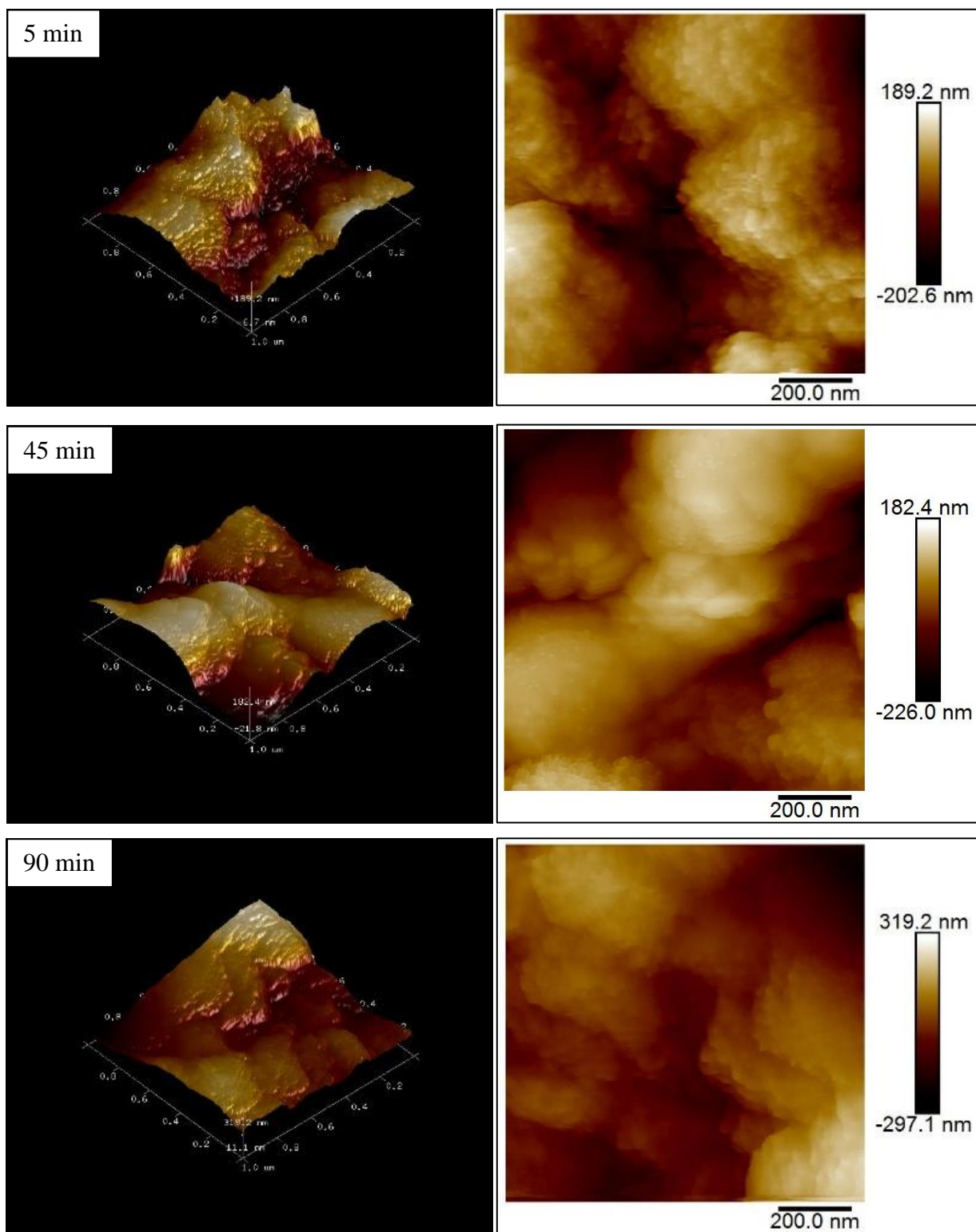


Figure 4.8: AFM 3D images for measuring the nanoscale roughness of silica agglomerates using samples coated with 5, 45, 90 min electrocoat time.

The wetting properties of the fabricated coatings were investigated using both the static and the sliding contact angles measurements. Table 4.1 manifests the contact and sliding angle measurements in addition to contact angle hysteresis of water and hexadecane for samples with hierarchical multiscale roughness.

Table 4.1: Surface wetting properties of samples with random hierarchical roughness using different spray times.

Spray time	DI water			Hexadecane		
	C.A. and S.A. (Ellipse fitting)	C.A. and S.A. (Young-Laplace fitting)	C.A Hysteresis (Ellipse fitting)	C.A. and S.A. (Ellipse fitting)	C.A. and S.A. (Young-Laplace fitting)	C.A Hysteresis (Ellipse fitting)
2 min	117 (N/A)	120°	N/A	80 (N/A)	80°	N/A
3 min	142 (N/A)	152°	N/A	93 (N/A)	94°	N/A
4 min	150 (4.9°)	165°	18°	95 (N/A)	96°	N/A
5 min	150 (0°)	168°	0°	146 (0.1°)	164°	0.5°
10 min	152 (0°)	175°	0°	147 (0.1°)	168°	0.6°
15 min	151 (0°)	173°	0°	148 (0°)	170°	0°
30 min	151 (0°)	170°	0°	147 (0°)	167°	0°
45 min	149 (0°)	168°	0°	146 (0°)	166°	0°
60 min	149 (0°)	166°	0°	146 (0°)	165°	0°
75 min	149 (0°)	165°	0°	145 (0.1°)	163°	0.6°
90 min	148 (0°)	164°	0°	143 (0.5°)	161°	1°

The change of spray time is intended to increase the surface roughness which in turn gives the desirable re-entrant/overhang structure. Figure 4.9 shows a schematic to illustrate the importance of the re-entrant and overhang structures obtained from different sizes of silica agglomerates. For spray time shorter than 5 minutes, the samples only present superhydrophobicity while they have strong affinity toward low surface tension liquids like hexadecane. The loss of superoleophobicity is due to the low surface roughness obtained at short spray times, by which the re-entrant structure is not attained (Fig. 4.10a). At longer spray times (above 60 min), the contact angle decreases as the surface roughness increases. This is mainly because of the increase of wetted area underneath the liquid droplet, as a result, the amount of trapped air is substantially decreased (Fig. 4.10b).

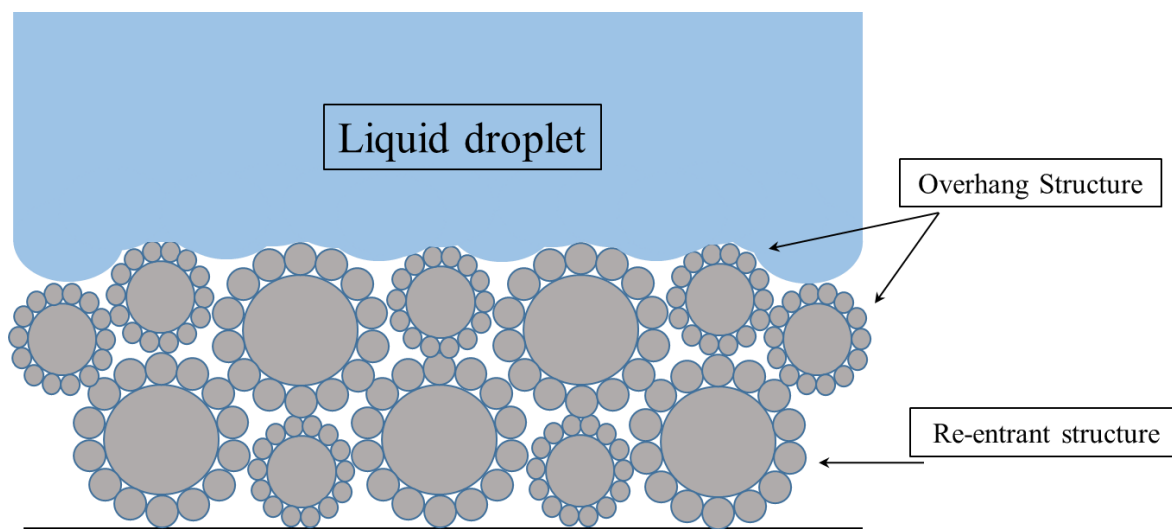


Figure 4.9: A schematic of the re-entrant and overhang structures.

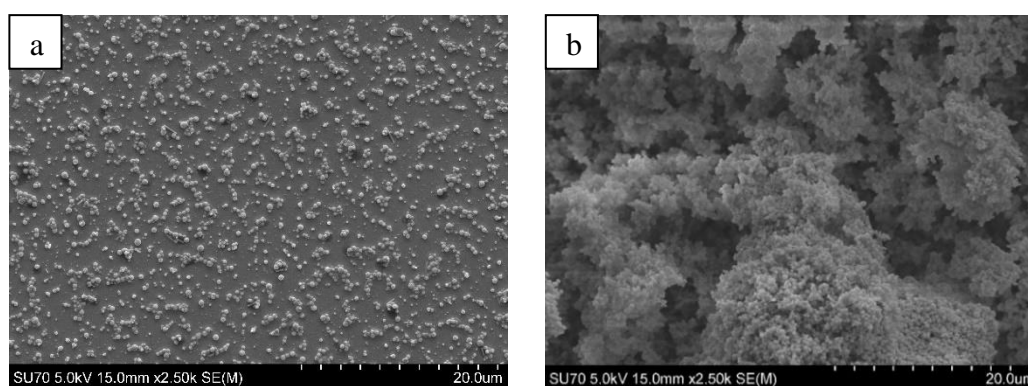


Figure 4.10: SEM images of samples with random hierarchical roughness: (a) sample fabricated at 2 min spray time, (b) sample fabricated at 90 min.

After a 15 min electro spray of SiO_2 suspension, the deposited nanoparticles become loose due to the large amount of stacked silica particles. To tackle the coating robustness issue, we have added a second layer of PDADMAC to preserve the deposited silica particles and to enhance surface roughness as explained in method section. Nevertheless, for long spray periods especially above 45 min, coating robustness decreases drastically. This could be attributed to two reasons: firstly, the nanoparticle-containing droplets become almost dry when depositing onto the substrate due to significant solvent evaporation during electro spray process. Secondly, a considerable amount of

the deposited particles stacks over each other with no binder material that could hold them in place. On the contrary, there is no need for the second PDADMAC and silica layer for samples with spray time below 15 min since the deposited silica particle seems to hold very well on the substrate. All the designed surfaces exhibit high contact angles with DI water and hexadecane; thus, we conclude that superhydrophobicity and superoleophobicity are accomplished by both the surface roughness with re-entrant structure and low surface energy obtained from chemically treating the surface with FDTS. These results are further corroborated by the extremely low sliding angles and contact angle hysteresis as shown in Table 4.1. However, with a longer spray time and increased surface roughness, the solid-area fraction at the liquid-solid-air interface could increase, by which the contact and sliding angles are negatively affected. Nevertheless, the produced samples at the longest spray time (90 min) still retain their super liquid repellent property against low surface tension liquids. Figure 4.11 demonstrates the relationship between the surface roughness its corresponding surface wettability.

It is worth noting that the accuracy of the static contact angle measurements mainly depends on the CCD camera's ability by which a crisp image of the sessile droplet could be obtained, the baseline establishment upon which the contact angle is calculated, the size of sessile droplet, the illumination adjustment, and the fitting methods used. Most of the literatures in this field unfortunately fail to mention the fitting methods they have used in obtaining their contact angles. For this reason, we did a comparison between ellipse fitting and Young-Laplace fitting methods to clear the confusion about the characterization of surface wettability.

The ellipse fitting presumes that shape of a liquid droplet setting on a surface is elliptical where the least fitting error is obtained by applying the ellipse fitting equation on droplet's profile. The crucial factors in making effective contact angle measurements with the smallest fitting errors are

droplet profile and baseline determination. However, ellipse fitting is not recommended for measuring droplets with high volume since the fitting curve deviates from the captured liquid profile. In addition to that, it is also not recommended when static contact angle is greater than 150° because of significant error introduced by its algorithm.^{6,86} On the other hand, the Young-Laplace fitting assumes that sessile liquid droplet is in a symmetrical shape and that gravity is the only force that affects the droplet's shape. The Young-Laplace fitting, which is also known as axisymmetric drop shape analysis (ADSA), is suitable for evaluating both droplets with high volume and high contact angles (greater than 150°). However, it is not resistant to noise which yields high fitting error when a distortion in droplet symmetry occurs.^{6,86}

Figure 4.11 depicts the difference between the contours and the baselines in the ellipse fitting and the Young-Laplace fitting for $3\ \mu\text{L}$ of DI water and hexadecane. By comparing the curve fitting with the droplet profile as shown in Figure 4.11, the ellipse fitting gave the smallest fitting errors.

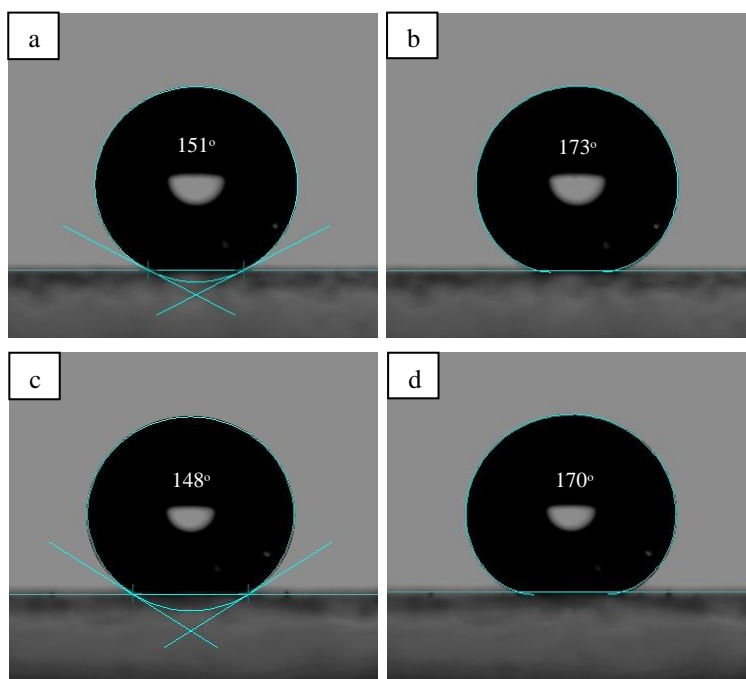


Figure 4.11: (a) Contact angle of $3\ \mu\text{L}$ DI water droplet using ellipse fitting, (b) Contact angle of $3\ \mu\text{L}$ DI water droplet using Young-Laplace fitting, (c) Contact angle of $3\ \mu\text{L}$ hexadecane droplet using ellipse fitting, (d) Contact angle of $3\ \mu\text{L}$ hexadecane droplet using Young-Laplace fitting.

In fact, in the discrepancy in contact angle measurements shows that contact angle only doesn't truly demonstrate the actual surface wetting properties of the coating surface, unless the fitting method is clearly stated.⁸⁷ Therefore, we prefer to use the ellipse fitting rather than the Young-Laplace fitting since our droplet size is 3 μL to minimize the fitting error produced.

4.3.2 Superhydrophobic and superoleophobic surfaces with patterned multiscale roughness

The main objective of this study is to generate micro-patterns in which the wetting properties of SHP and SOP coatings could be enhanced. Figure 4.3b illustrates the procedure to pattern the silica particles on a substrate using a mass-assisted electro spray technique. For this purpose, a positive DC voltage was applied to the mask, resulting in a focusing electric field between the mask and the grounded substrate. The charged silica particles with the same polarity (positive) are forced to deposit on the substrate (glass slide) through the openings of the mesh. As a result, microscale pillars are created on the substrate and overall efficiency of electro spray process are improved by reducing the amount of charged particles depositing on the mesh. The PTFE coating on the stainless steel mesh, although not perfectly cover all the mesh wires, also contributes to repelling of the positively charged particles. When some positively charged particles deposited on the mesh initially, the charges will accumulate and suppress further deposition of charged particles on the mesh. However, a major portion of the spraying material could be lost (depositing onto the mesh) in the case of no voltage being applied because the stainless steel mesh isn't totally covered with PTFE (Fig. 4.12). The micropillars were generated at different gaps ranging from 70 μm up to 500 μm . All the pillars were similar in shape for different gaps except the 140 μm gap. The fabricated pillars became elongated when the mask was placed 140 μm away from the glass slide and a wavy structure was obtained (Fig. 4.13).

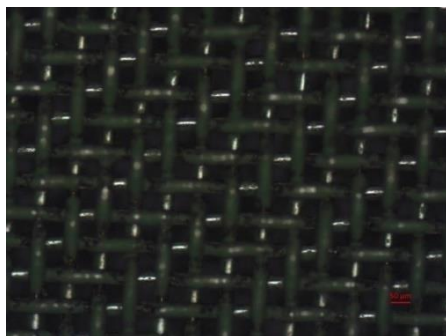


Figure 4.12: PTFE coated stainless steel mesh.

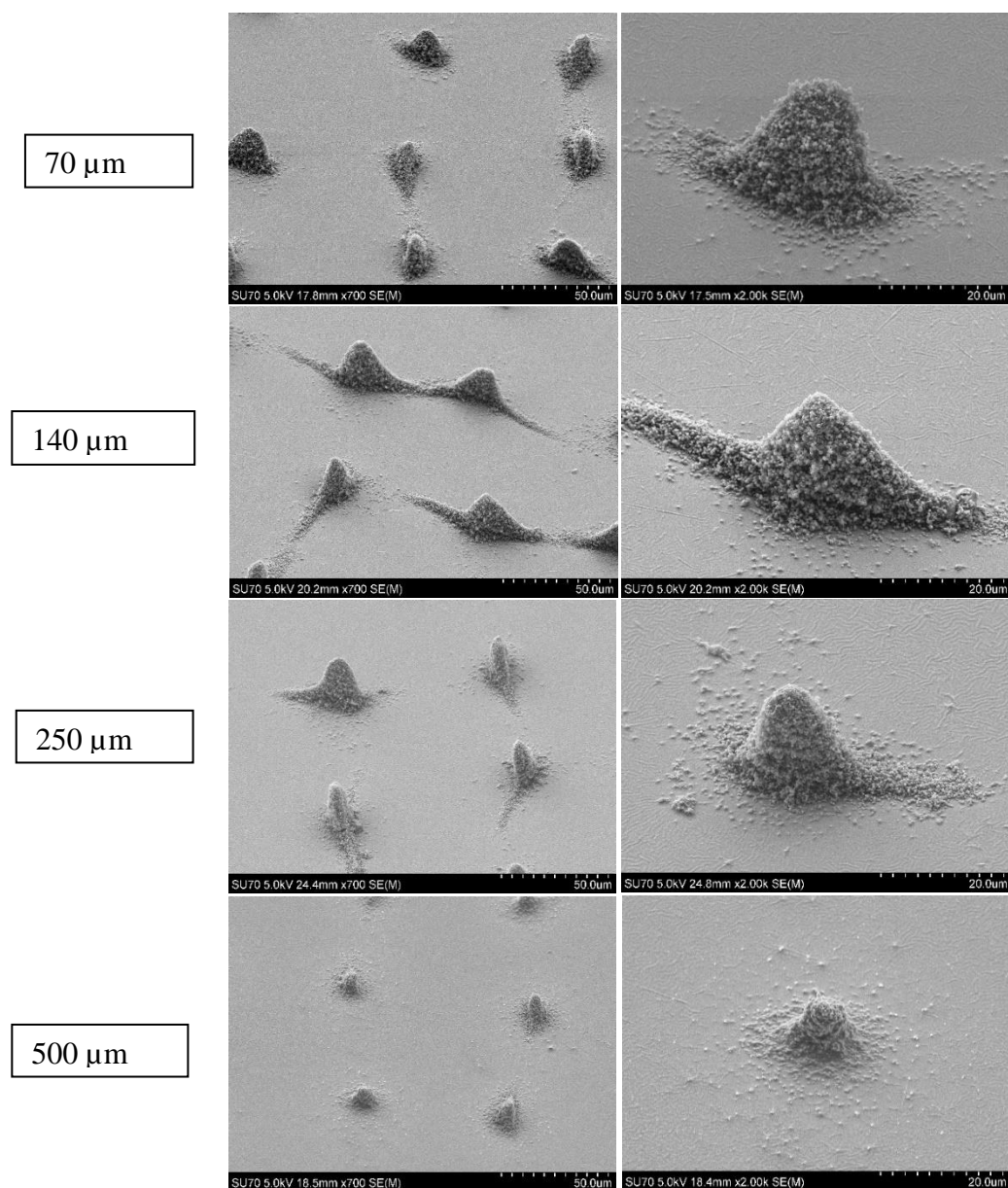


Figure 4.13: Shows SEM images of the fabricated pillars using different mesh gaps ranging from 70 to 500 μm , before addition of the second SiO_2 layers. The images were taken with 45° tilting angle.

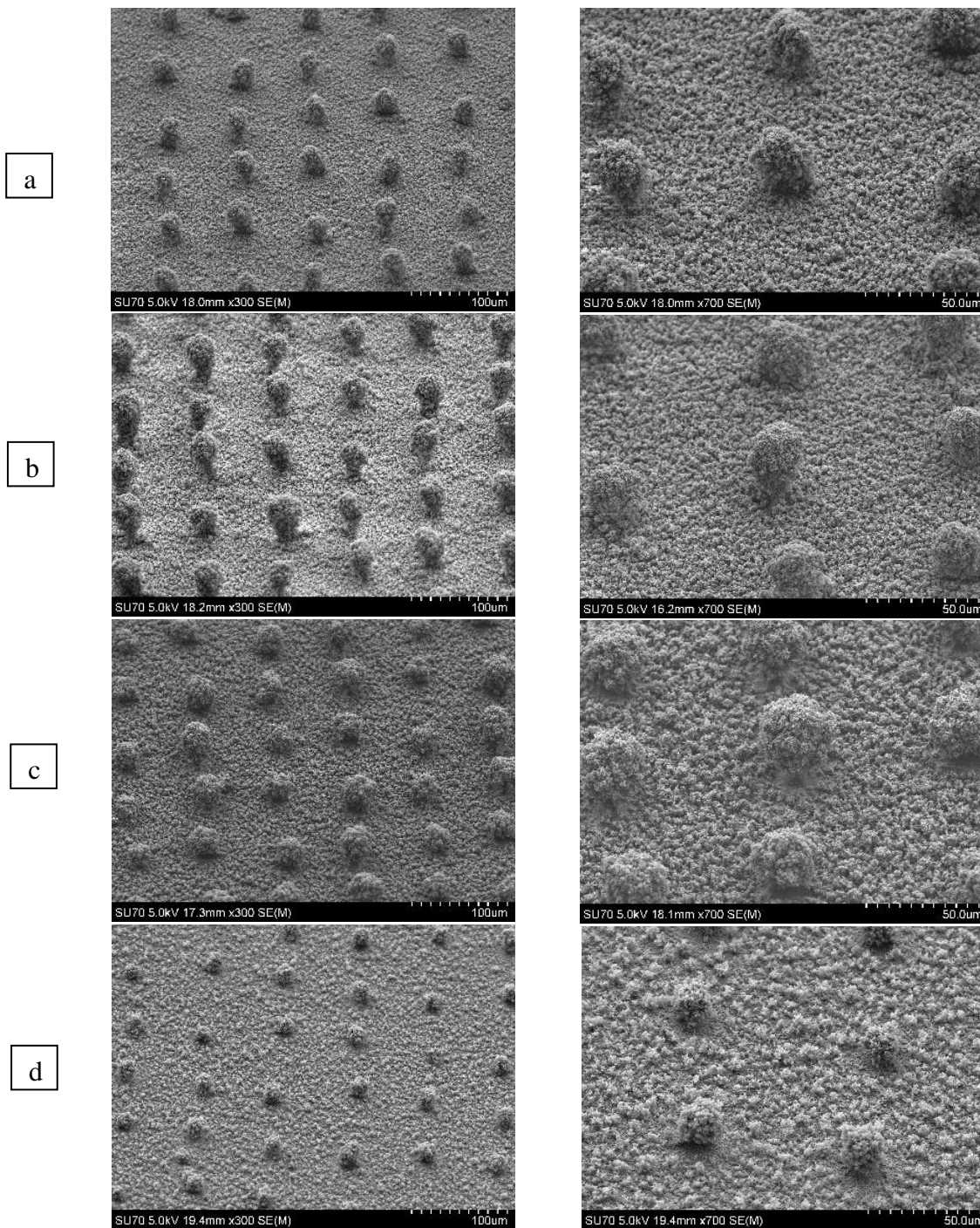


Figure 4.14: (a) micro-pillars fabricated using 70 μm gap, (b) micro-pillars fabricated using 140 μm gap, (c) micro-pillars fabricated using 250 μm gap, (d) micro-pillars fabricated using 500 μm gap.

This means that the focusing of electric field lines get deviated and refracted when the mesh is placed at this particular gap. The pillars generated at a shorter gap are taller and wider than those

at a larger gap since a stronger focusing electric field in the former lead to more efficient deposition onto the substrate instead of the mesh.

Interestingly, a drastic change in morphology were observed after a successive 10 minutes electro spraying of SiO₂ layers without mesh. Figure 4.14 shows SEM images of the samples tilted at a 45° angle. Pillars with dome-like shape were obtained with the desirable re-entrant structures along with the overlaid layer of random hierarchical micro/nano roughness over the pillars and the entire substrate surface.

The LSM was employed in this study to measure the average pillar heights. As the gap between the mesh and the substrate increases, the height of the fabricated pillars decreases. This could be attributed to the strong electric effect generated when the mesh is placed close to the substrate. Subsequently, more charge particles could be deposited on the substrate when the mesh gap is 70 μm than that of higher mesh gaps. The average height of pillars is ranging from 10.5 μm when the mesh gap is 500 μm up to 21.8 μm when the used gap is 70 μm. The standard deviation of each roughness measurement ~ 2 μm. Figure 4.15 shows 3D pictures of the patterned samples with microscale roughness using different gaps after depositing the second layer of SiO₂ and fluorinating the samples with FDTs. The red line in the presented LSM pictures indicates the pillar height profile of each fabricated sample. Figure 4.16 presents the relation between the average height of the fabricated pillars with respect to different substrate-mesh gaps.

Our carefully designed micro-pillars, by which the re-entrant structure is accomplished, successfully prevent DI water and hexadecane from wetting the surface. As the gap between the substrate and the mesh increases, the height of the fabricated pillars decreases. For instance, at 500 μm the pillars become small as compared to the 70, 140, and 250 μm gaps. It seems that the electric focusing effect is inversely correlated with the increase in mesh gaps. In other words, closer mesh

gaps enhance the focusing effect by which the charge particles prefer to deposit on the designated substrate rather than depositing elsewhere.

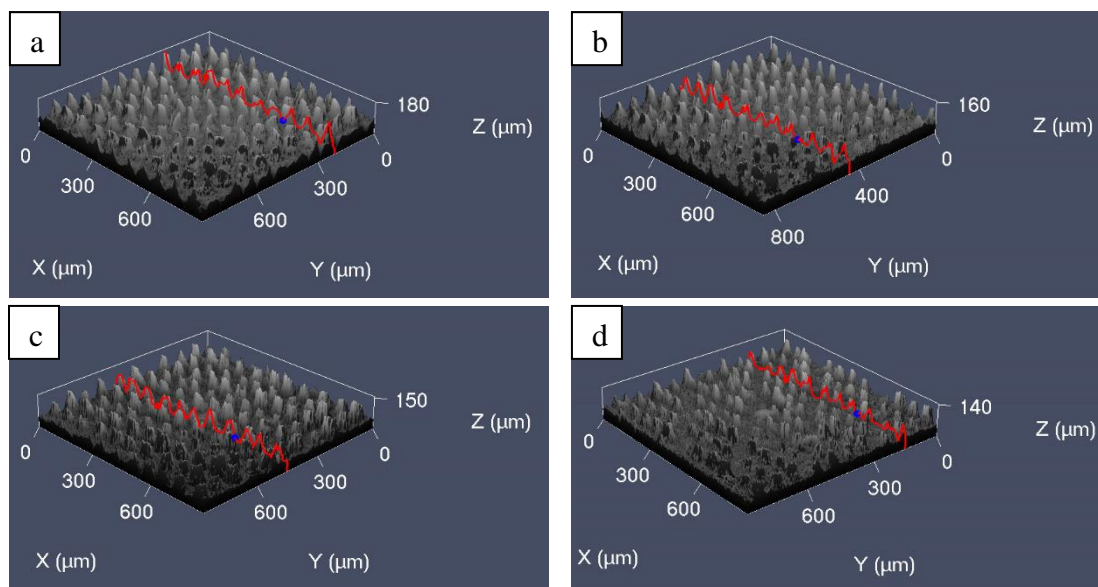


Figure 4.15: LSM 3D images of patterned samples with multiscale roughness fabricated using different mesh gaps: (a) 70 μm , (b) 140 μm , (c) 250 μm , (d) 500 μm .

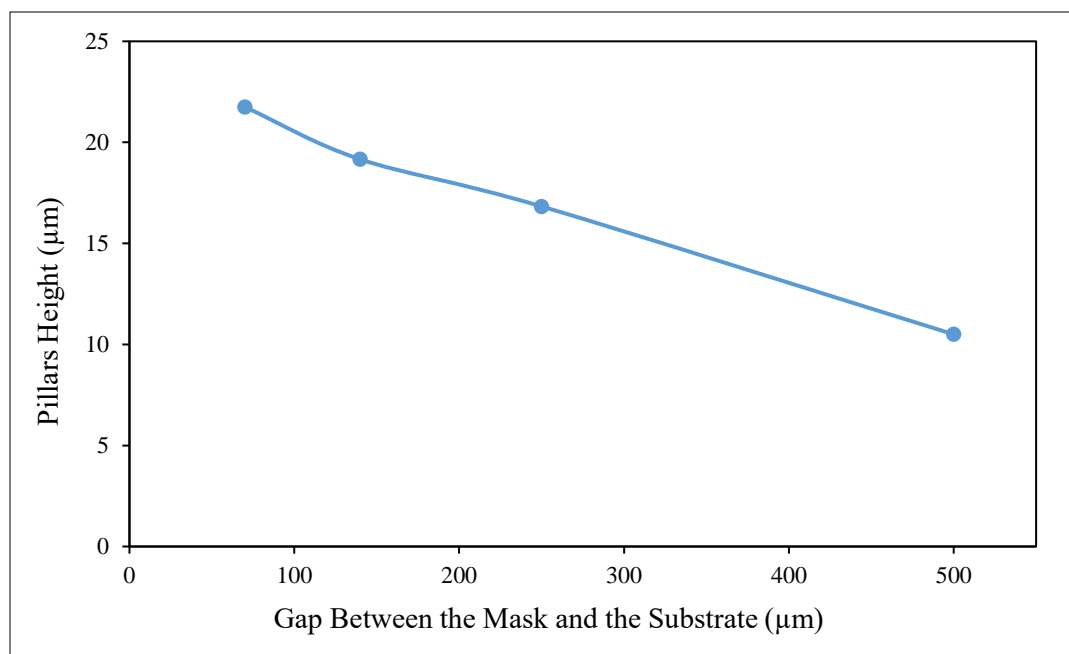


Figure 4.16: Pillars' average height of patterned samples with multiscale roughness fabricated using different mesh gaps: (a) 70 μm , (b) 140 μm , (c) 250 μm , (d) 500 μm .

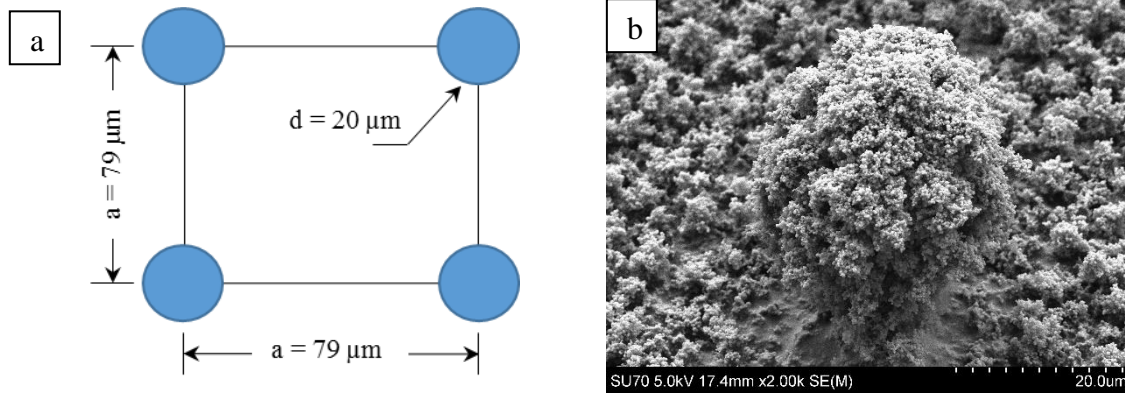


Figure 4.17: (a) pillars patterns by which the solid area fraction is reduced, (b) SEM picture of an individual pillar.

Figure 4.17 demonstrates the benefits of pillar structures with a large spacing. By assuming the solid-area fraction of surfaces with random hierarchical roughness is 5 %, then the surface-area fraction, which is calculated using equation (4.1), of patterned surfaces with multiscale roughness is reduced to 20 times than that of surfaces with random hierarchical roughness.

$$f = \frac{\pi d^2}{4 a^2} \quad (4.1)$$

where f is the solid-area fraction, d is pillar diameter, and a is the center-to-center spacing of the PTFE coated mesh.

The average diameter of the fabricated pillars is 20 μm and calculated area is considered according to the center-to-center spacing of the PTFE coated stainless steel (79 μm x 79 μm). This ultimate reduction in solid-area fraction resulted in a reduced wetting area and an improved surface wetting properties especially with low surface tension liquids. The large spacing is particularly desirable in providing a large slip length for drag reduction application.⁸⁸

To get a better insight about the functionality of the fabricated pillars, we have pictured DI water and hexadecane droplets sitting on these patterns in which the confined air cushions could be clearly seen (Fig. 4.18).

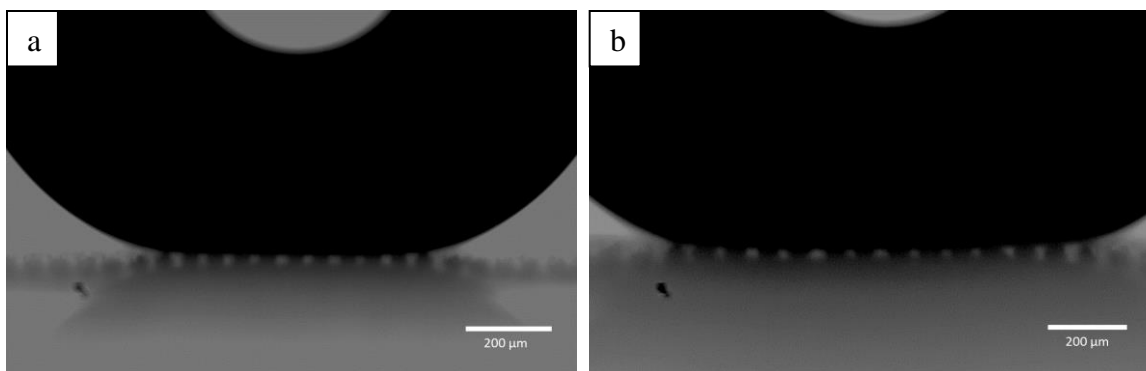


Figure 4.18: (a) and (b) are DI water and hexadecane droplets respectively sitting on the fabricated pillars using the 140 μm gap. The pictures were taken by goniometer.

All the fabricated samples with patterned coatings presented excellent wetting properties against DI water and hexadecane. Table 4.2 shows the wetting properties of patterned samples with multiscale roughness. By comparing contact angle data for samples with random hierarchical roughness and patterned multiscale roughness, we deduce that the success in improving the surface wetting properties against low surface tension liquid is achieved by having more air cushions trapped under the liquid droplet, which in turn, minimizes the wetted area.

Table 4.2: Wetting properties of samples with patterned multiscale roughness.

Mesh gap	DI water			Hexadecane		
	C.A. and S.A. (Ellipse fitting)	C.A. and S.A. (Young-Laplace fitting)	C.A Hysteresis (Ellipse fitting)	C.A. and S.A. (Ellipse fitting)	C.A. and S.A. (Young-Laplace fitting)	C.A Hysteresis (Ellipse fitting)
70 μm	151 (0°)	171°	0°	146 (0.2°)	169°	0.7°
140 μm	153 (0°)	173°	0°	152 (0°)	171°	0°
250 μm	152 (0°)	173°	0°	152 (0.1°)	170°	0.9°
500 μm	150 (0°)	163°	0°	145 (0.9°)	160°	0.8°

According to the 3D topographies shown in Figure 4.15, all the fabricated samples, except the one at the 500 μm gap, have well-ordered pillars. This could explain the decrease in apparent contact angle of hexadecane of the named surface. In other words, the amount of the trapped air cushions is less within this particular sample as compared with others due to the short produced pillars and

the lack of consistent patterns. Testing liquids tend to wet into the bigger space between the micro-pillars resulting in an increased wetted area. However, the sample still exhibiting the superhydrophobicity and the superoleophobicity due to the presence of the second silica layer.

It should be noted that the voltage applied to the needle, with respect to the specific flow rate according to Figure 4.2, is higher by 2 kV (i.e., the voltage applied on the mesh) in case of patterned surfaces than that used for samples with random hierarchical roughness. In other words, higher voltage should be applied to the needle to overcome the mesh opposing voltage. At high flow rates higher than 4 $\mu\text{L}/\text{min}$, a stable jet becomes difficult to attain. In addition to that, partial blockage of the needle that causes a refraction or skewness in spraying direction is noticed especially when the voltage is applied to the mesh. This is a common issue associated with electrospray deposition that is mainly caused by following reasons: Firstly, the fast evaporation of isopropanol in the solution which facilitates the accumulation and the solidification of the silica particles on the nozzle's tip. Secondly, the presence of the voltage applied on the mesh. Third, the surrounding areas are not totally insulated. This skewness in jet direction leads to major loss of the raw material and thus poor coating quality that may affect the wetting properties. Figure 4.19 shows the difference between a stable-jet and skewed-jet.

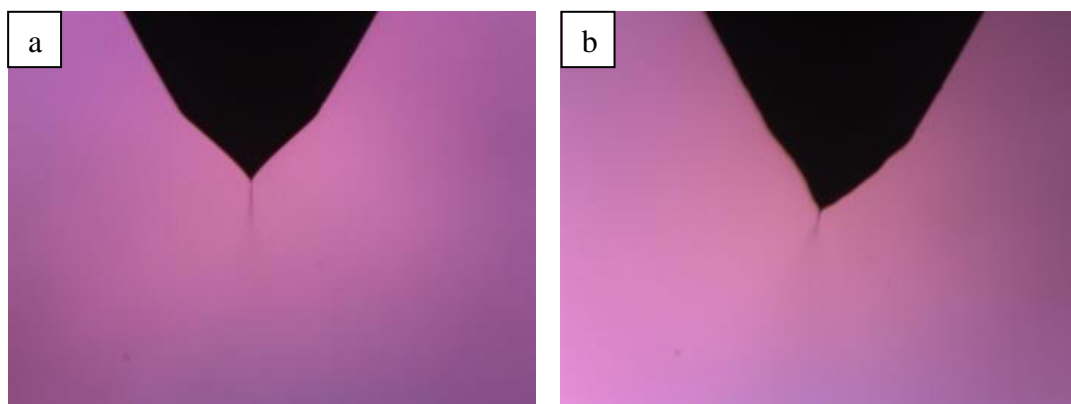


Figure 4.19: (a) stable-jet, (b) skewed-jet.

4.4 Conclusion

In summary, we have demonstrated and for the first time that SOP coatings could be produced using the electrospray deposition technique. In this work, two approaches were used to fabricate such coatings with random hierarchical roughness and patterned multiscale roughness. First, the silica nanoparticles were directly deposited on a glass slide to generate samples with multiscale random roughness. Second, a PTFE coated stainless steel mesh was employed in order to pattern the particle on the substrate. The use of the mask and the focusing voltage applied to the needle helped to improve the overall efficiency of electrospray process. While similar attempts have been devoted for the sake of preparing textured coatings, none of which has been successfully implemented to produce SHP and SOP surfaces with patterned and random multiscale roughness. All the samples were produced through electrospraying silica nanoparticles on a glass slide then followed by chemical treatment. The fabricated samples give a clear evidence about importance of the re-entrant structure by which the wetted area are drastically decreased leading to outstanding surface wetting properties. These findings were further corroborated with extremely low sliding angles and contact angle hystereses for both DI water and hexadecane.

We have demonstrated that mask-assisted electrospray can be utilized to fabricate SHP and SOP surfaces with a large design space which have never been explored before.

CHAPTER 5 Modeling of Textured Surface Formation in Mask-assisted Electrospray

5.1 Introduction

The present study has a twofold objective: (i) to investigate the nature of electric field focusing that influences the deposition of charged particles on a substrate; (ii) to simulate and analyze the physical processes associated with the deposition of charged particles in the mask-assisted electrospray. These processes are comprised of electric field, particle trajectory, solvent evaporation, and particle transport.⁸⁵ For this purpose, the COMSOL Multiphysics 5.2a was employed to interpret and quantify the factual parameters acquired by the electrospray. A 2D model was created to simulate the electric field focusing effect using the electrostatic module that is available in AC/DC model. In addition to that, the particle tracing module was incorporated with electric field module in which the interactions of particle-electrical field, particle-flow field, and particle-particle interactions were taken into consideration. A Lagrangian particle tracking equation was solved for charged particles on which drag force, gravitational force, buoyancy force, Brownian force, electrostatic Coulomb force, and particle-particle interaction forces are exerted. Since the charged particles in the simulated region of interest were released from an inlet that is very close to the substrate, solvent evaporation was not considered in this simulation. One-way coupling is assumed in this work where the addition of charged particles don't affect the electrical field distribution. The simulation results were compared to the experimental findings and a qualitative agreement was obtained in terms of charged particle deposition in mask-assisted electro spraying.

5.2 Simulation domains and mesh geometry

In this work, two different simulation domains were defined for electrical field simulation and for particle tracking, respectively. In order to accurately investigate the focusing effect of the

electric field with respect to different mesh-substrate gaps, a simulation domain of 53 mm x 30 mm (Domain A) was defined including the same experimental parameters and geometries, as described in Chapter 4. However, computing particle trajectory with the above mentioned dimensions is very challenging due to the multi-body interactions involved in this model and the expensive computational cost. Accordingly, a simulation domain of 2 mm x 2 mm (Domain B) was chosen since the region of interest is between the mesh and the substrate. Furthermore, only 15 mesh wires with diameters and spacing of 36 μm and 79 μm respectively were used to investigate the effect of electrical field focusing. Five thousand (5000) charged particles were released into simulation Domain B, which were assumed to be uniformly distributed. When a typical electro spray without mesh was simulated, only 8 kV was applied to the needle and the mesh was removed. However, in case of producing patterned coatings in mask-assisted electro spray, 10 kV and 2 kV were applied to the needle and the mesh respectively. Figure 5.1 is a cartoon illustration of domain A and domain B.

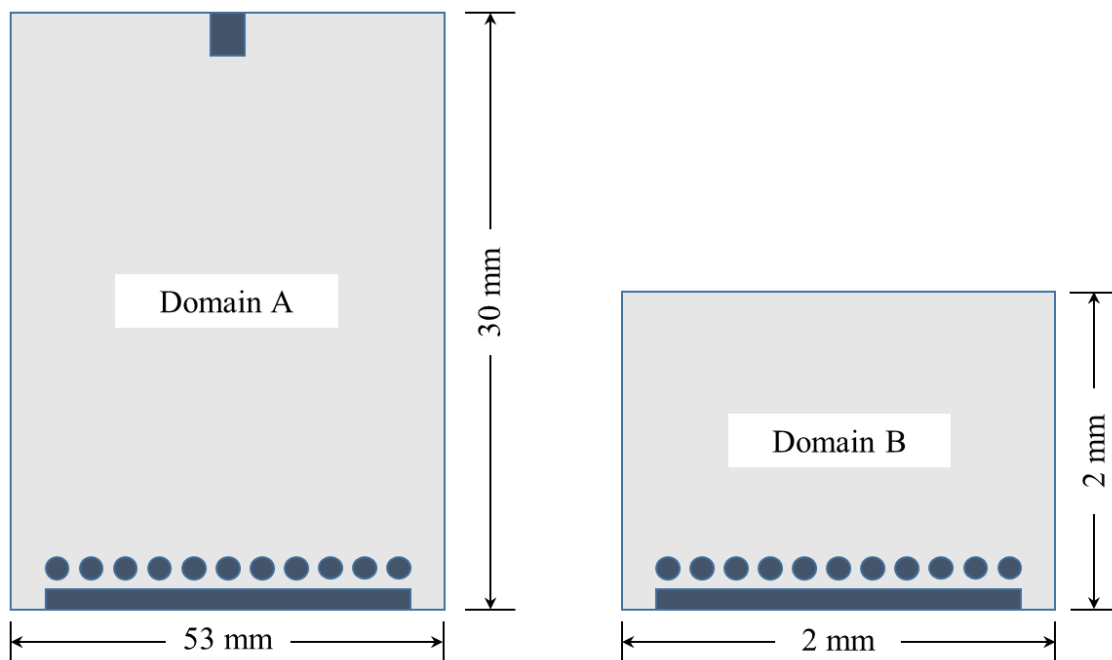


Figure 5.1: A cartoon illustration of domain A and domain B.

5.3 Electric field and charged particle dynamics

The electrical field \mathbf{E} (V/m) is calculated by a gradient equation.

$$\mathbf{E} = -\nabla V \quad (5.1)$$

where V is the electric potential.

The motion of a charged particle in a flow field is governed by the following Lagrangian equation:

$$m \frac{dv_p}{dt} = \mathbf{F}_d + \mathbf{F}_g + \mathbf{F}_{bo} + \mathbf{F}_b + \mathbf{F}_{es} + \mathbf{F}_{pp} \quad (5.2)$$

where m is the mass of the traveling particle (kg), v_p is the particle velocity (m/s), F_d is the drag force (N), F_g is the gravitational force (N), F_{bo} is the buoyancy force (N), F_b is the Brownian force (N), F_{es} is the electrostatic force (N), and F_{pp} is the particle-particle interaction force (N). In COMSOL the Drag force is expressed as in Eq. (5.3) below.

$$\mathbf{F}_d = \left(\frac{1}{\tau_p s} \right) m_p (\mathbf{u} - \mathbf{v}) \quad (5.3)$$

where \mathbf{u} is the velocity of the particle (m/s), \mathbf{v} is the fluid velocity (m/s), τ_p is the particle velocity response time that could be computed using Eq. (5.4), and s is the drag force correction factor as expressed in Eq. (5.5).

$$\tau_p = \frac{\rho_p d_p^2}{18\mu} \quad (5.4)$$

$$s = 1 + K_n (C_1 + C_2 e^{-\frac{C_3}{K_n}}) \quad (5.5)$$

In Eq. (5.4), ρ_p represents the particle density (kg/m^3), d_p is the particle diameter (m), and μ is the fluid dynamic viscosity (Pa. s). In Eq. (5.5), K_n is the Knudsen number that is expressed by Eq. (5.6), and C_1 , C_2 , and C_3 are characteristic parameters that equal to 1.142, 0.558, and 0.999 respectively for solid particles.⁸⁹

$$K_n = \frac{\lambda}{d_p} \quad (5.6)$$

where λ is the mean free path of gas molecules and d_p is the particle diameter. In COMSOL the mean free path is expressed by Eq. (5.7) below.

$$\lambda = \sqrt{\frac{\pi}{2P\rho}} \mu \quad (5.7)$$

where p is the gas pressure (Pa), ρ is the gas density (kg/m^3), and μ is the gas viscosity (Pa s). Since the electrostatic force is the dominant force in our case and the density of silica particles are much larger than the density of the surrounding fluid (i.e., air), the effect of the gravitational force and buoyancy force were not considered in the created model.⁹⁰ The small effect of Brownian force on the charged particles is calculated in COMSOL using Eq. (5.8).

$$\mathbf{F}_b = \zeta \sqrt{\frac{12\pi k_b \mu T r_p}{\Delta t}} \quad (5.8)$$

where ζ is a normally distributed random number with a mean of zero and unit standard variation, k_b is Boltzmann's constant, T is the absolute fluid temperature, r_p is the particle radius, and Δt is the time step taken by the solver.

The contribution of the electric field is computed by Eq. (5.9) in which the applied voltage to the needle and the mesh were taken into account in the built model.

$$\mathbf{F}_{es} = eZE \quad (5.9)$$

where e is the elementary charge (s A), Z is the charge number (dimensionless number), and \mathbf{E} is the electrical field which is calculated by the Eq. (5.1).

Additionally, as the particles are highly charged because of the high potential difference applied, the interaction between the particles cannot be neglected. For this reason, the particle-particle interaction force, which is best explained in Eq. (5.10), was implemented complementary to the external forces acting on each individual particle.

$$\mathbf{F}_{pp} = -Gm^2 \sum_{j=1}^N \frac{(\mathbf{r}_i - \mathbf{r}_j)}{|\mathbf{r}_i - \mathbf{r}_j|^3} \quad (5.10)$$

where \mathbf{r}_i and \mathbf{r}_j are position vectors of the i^{th} and j^{th} particles, G is the gravitational constant ($6.674 \times 10^{-11} \text{ N}\cdot\text{m}^2/\text{kg}^2$), and m is the particle mass (kg).

In order to solve the above mentioned equations, the electro sprayed particle's information i.e., particle mass, particle diameter, particle charge number, and the initial velocity of the particle must be identified in COMSOL. For this purpose, the scaling theory proposed by Gañán-Calvo was employed to obtain the relevant electro spray parameters as inputs to the modeling.^{91,92} The electro spray current and the particle diameter could be estimated from Eq. (5.11) and (5.12) below.

$$I = \left(\frac{\sigma K Q}{\beta - 1} \right)^{1/2} \quad (5.11)$$

$$d = \left(\frac{\varepsilon_0 Q}{K} \right)^{1/3} \quad (5.12)$$

where σ is the liquid surface tension (N/m), K is the liquid electric conductivity (S/m), Q the liquid flow rate (m^3/s), ε_0 is the vacuum permittivity (F/m), and β is the ratio of the liquid to vacuum permittivity. Furthermore, Eq. (5.13) could be used to compute the charge of an individual particle by which the charge number (Z) and the total number of particles in the calculation domain could be determined.

$$q_d = \frac{\pi d^3 I}{6Q} \quad (5.13)$$

The initial velocity of the charged particles was set to be 0.23 m/s according to results acquired by a Phase Doppler Particle Analyzer.^{84,85} Table 5.1 shows the particle input parameters utilized to simulate the trajectory of the charged particles.

Table 5.1: Particle input parameters for simulating the particle trajectory.

Description	Value
Particle Diameter	87 nm
Particle Charge	$3.67 \times 10^{-17} \text{ C}$
Particle's Initial Velocity	0.23 m/s
Particle mass	$9.24 \times 10^{-19} \text{ kg}$

Other parameters like different working mesh gaps, voltage applied to the needle and the mesh, and the characteristics of the working domain were set in COMSOL in order to have a good basis for comparing between the real case and the simulated one (See appendix A for more details about model instructions).

5.4 Simulation of the electric field

A 2D model was created to simulate the electric field focusing effect obtained from applying voltage to the mask. The experimental configurations illustrated in Figure 4.3, i.e., electrospray without mask and mask-assisted electrospray, were considered in the simulation to prove and validate the experimental observations regarding the particle deposition and electrospray efficiency. Figure 5.2 shows the electric field contour lines comparison among different mesh-substrate gaps.

For patterned surfaces, a 2 kV was applied on the mesh and a 10 kV was applied on the needle. However, for samples without patterned coatings when no mask is needed, only 8 kV was applied to produce an equivalent electric field and a stable cone jet. The equipotential contour lines illustrate the gradient of the applied voltage which exemplifies a clear evidence about why a higher voltage applied to the needle is necessary to achieve a stable jet when an additional voltage is applied on the mesh. In other words, additional 2 kV is required for the needle to overcome the

resistance of the 2 kV applied to the mesh so that the meniscus at the needle experiences an equivalent electrical force to overcome the surface tension and forms a stable cone jet (Fig. 5.3).

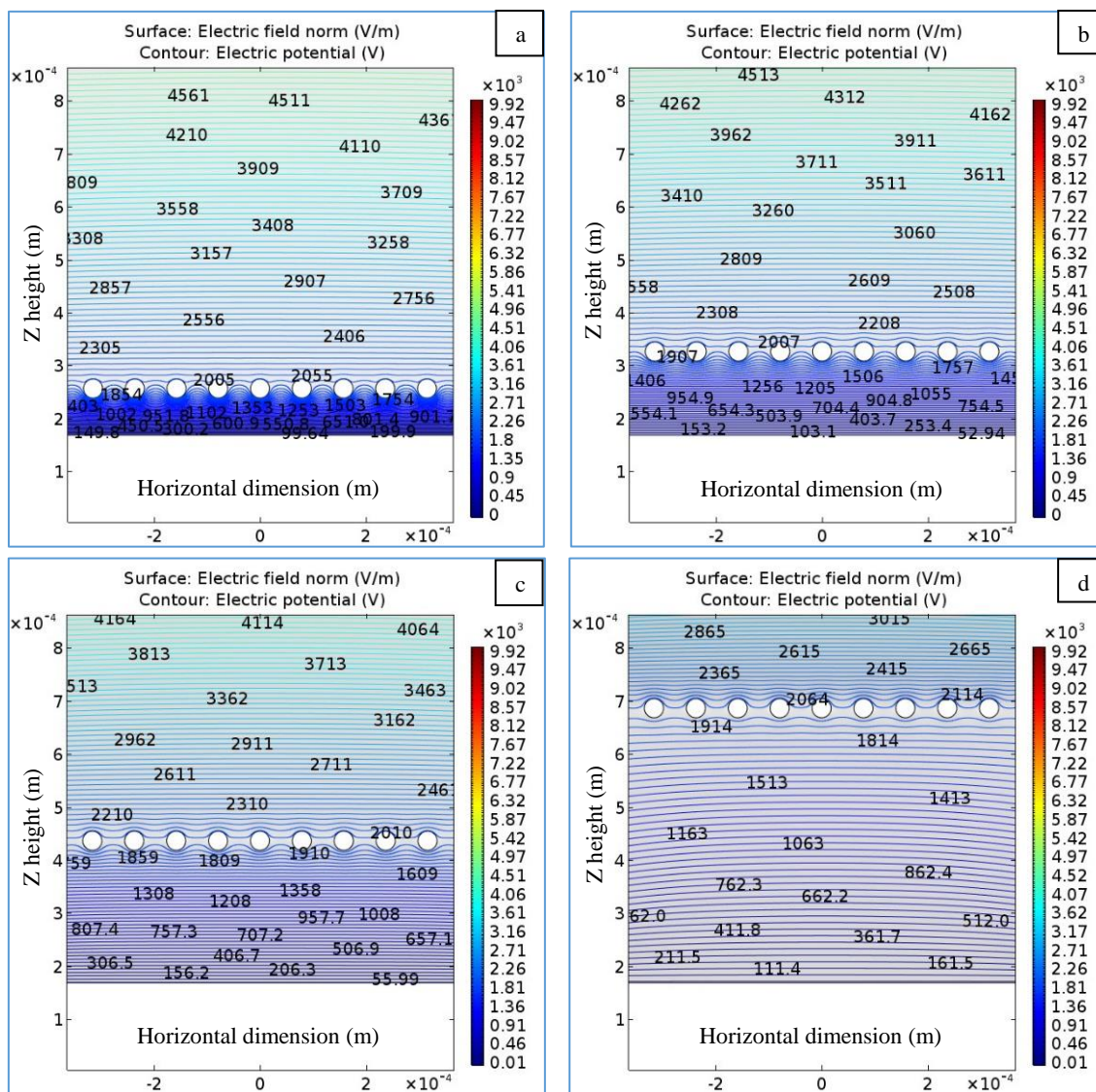


Figure 5.2: Contour lines of electric field when 10 kV applied on the needle and 2 kV applied on the mesh using the following mesh gaps: (a) 70 μm , (b) 140 μm , (c) 250 μm , (d) 500 μm . The legend indicates voltage applied on the needle and all axes scale in meters.

Figure 5.4 illustrates the focusing effect of electric field streamlines when a 2 kV is applied to the mesh with different mesh gaps where the electric field lines are deviated away from the mesh. The focusing of electric field lines provides a proof of the ability to form micro patterns when a voltage

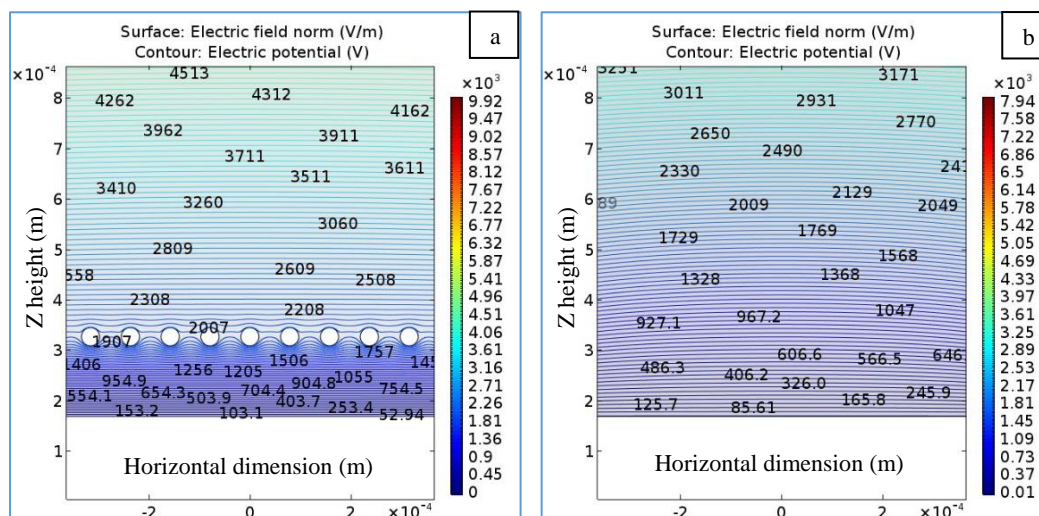


Figure 5.3: (a) contour lines of electric field used for patterned samples when a 10 kV is applied on the needle and a 2 kV is applied on the mesh using the 140 μm mesh gap, (b) contour lines of electric field used for sample with random surface roughness when only 8 kV is applied on the needle. The legend indicates voltage applied on the needle.

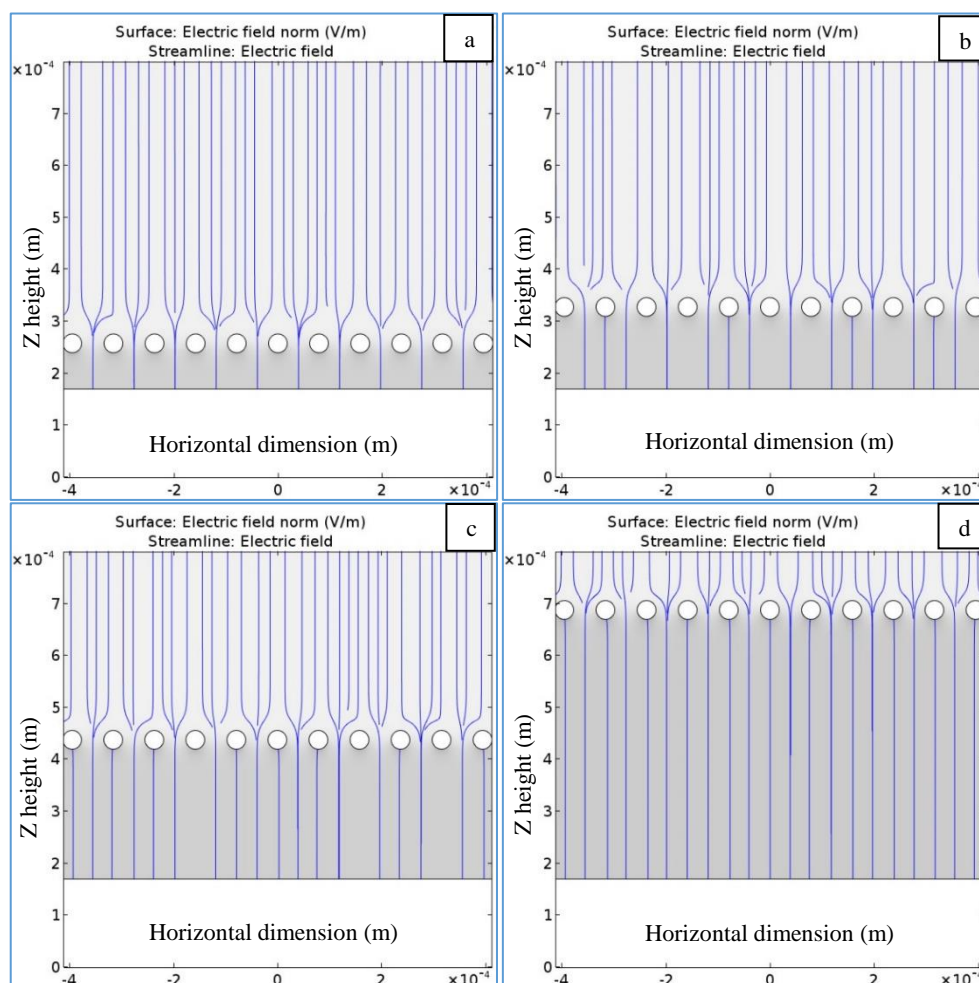


Figure 5.4: Streamlines of electric field when 10 kV applied on the needle and 2 kV applied on the mesh using the following mesh gaps: (a) 70 μm , (b) 140 μm , (c) 250 μm , (d) 500 μm . All axes scale in meters.

with the same polarity as the needle is applied to the mesh. All the configurations with various mesh-substrate gaps demonstrate the electrical field focusing effect. However, the shorter the gap is, the closer the equipotential lines; correspondingly stronger focusing effect is experienced by the charged particles. The trajectory of the charge particles is calculated in the following section in order to get better understanding of mesh-substrate gap effect on the particle deposition and electro spray deposition efficiency.

5.5 Simulation of the trajectory of charged particles

The effect of electric field focusing with various mesh-substrate gaps were further investigated by simulating the particle trajectory using the particle tracing module in COMSOL. The motion of the charged particles was studied in a smaller 2 mm x 2 mm domain (Domain B). In this study, five thousand (5000) charged particles with 87 nm in diameter were released uniformly at the inlet of the calculation domain B. Figure 5.5 shows particle deposition with different mesh-substrate gaps. The focusing effect is the strongest when the gap is 70 μm while the patterns tend to spread if the mesh is placed at higher gaps.

It should be mentioned that the particle-particle interaction takes place once the charged liquid droplets of the spraying material get disintegrated due to electrostatic force to form the so called electro spray plume.⁹³ When the charge particles move away from the needle's tip, they become more separated and thus the electrostatic interaction between the charged particles gets diminished.⁹⁴ however, once the charged particles reach the mesh in which the potential difference is applied, the particles get squeezed and focused. Accordingly, if the mesh is placed at 70 μm gap, the charged particles experience stronger electric Coulomb force and remain focused while they deposit on the substrate. Conversely, if the mesh is placed at higher gaps, the interaction between the particles due to the high concentrated charges along with the weaker electrical Coulomb forces

by the electric field tend to separate and spread those charged particles. This could be the answer of why larger mesh gaps produces weaker patterns.

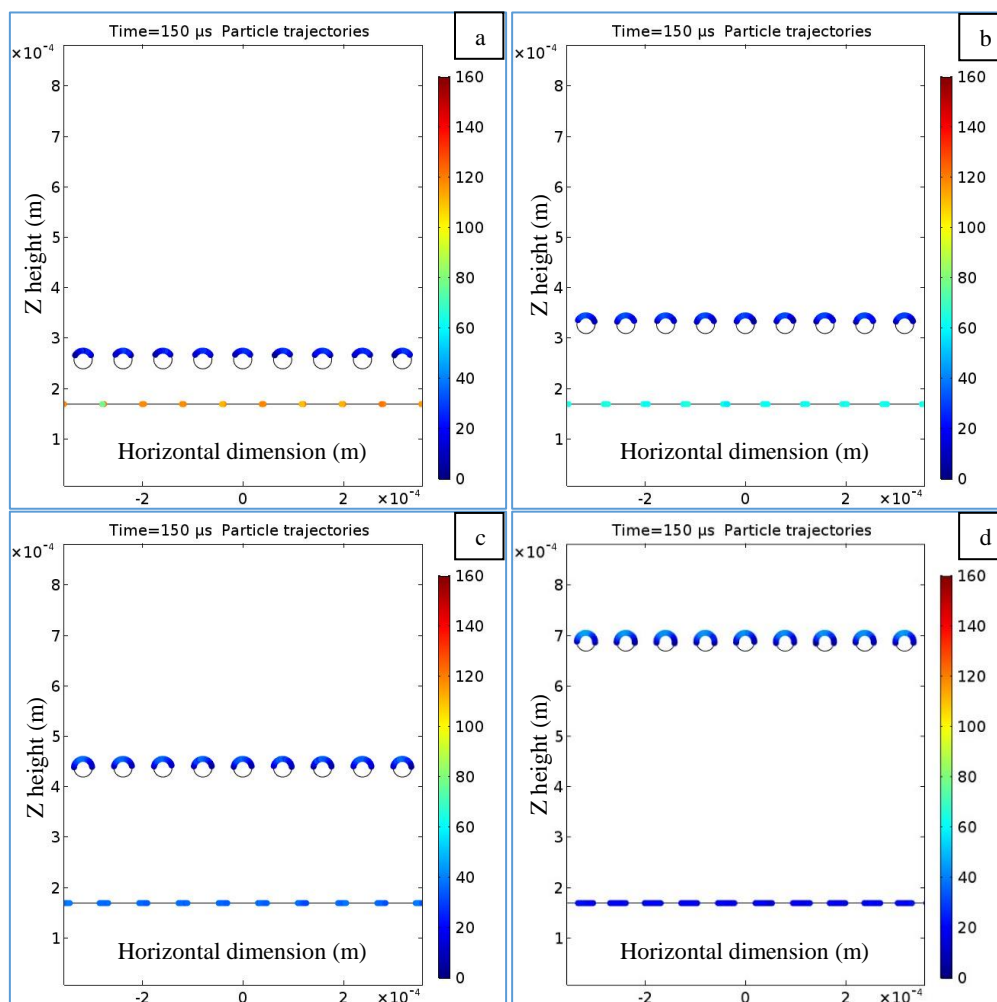


Figure 5.5: The charged particles deposition on a substrate using different mesh gaps: (a) is 70 μm gap, (b) is 140 μm gap, (c) is 250 μm gap, (d) is 500 μm gap. The legend indicates the velocity of the particle (m/s) and all axes scale in meters.

Figure 5.5 also indicates that the velocity of the deposited charged particles is the highest when the mesh is placed at 70 μm gap and vice versa.

As a matter of fact, patterning silica charged particles on a substrate without applying voltage to the mesh is possible, since the stainless steel mesh is PTFE coated. However, the majority of the

deposited particles were noticed to attach to mesh instead of to substrate. This fact could be more explicated in Figure 5.6 that portrays the difference between electric field streamlines when in both cases.

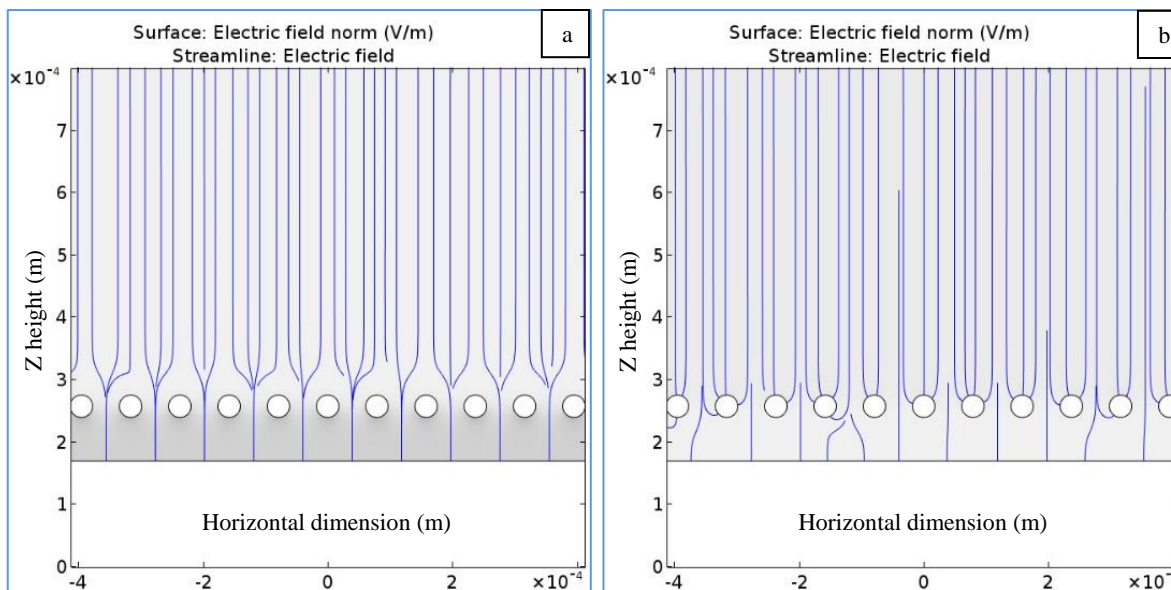


Figure 5.6: (a) streamlines with 2 kV is applied on the mesh with 70 μm gap, (b) streamlines when no voltage is applied on the mesh using the same mesh gap. Axes scale of the images is in meters.

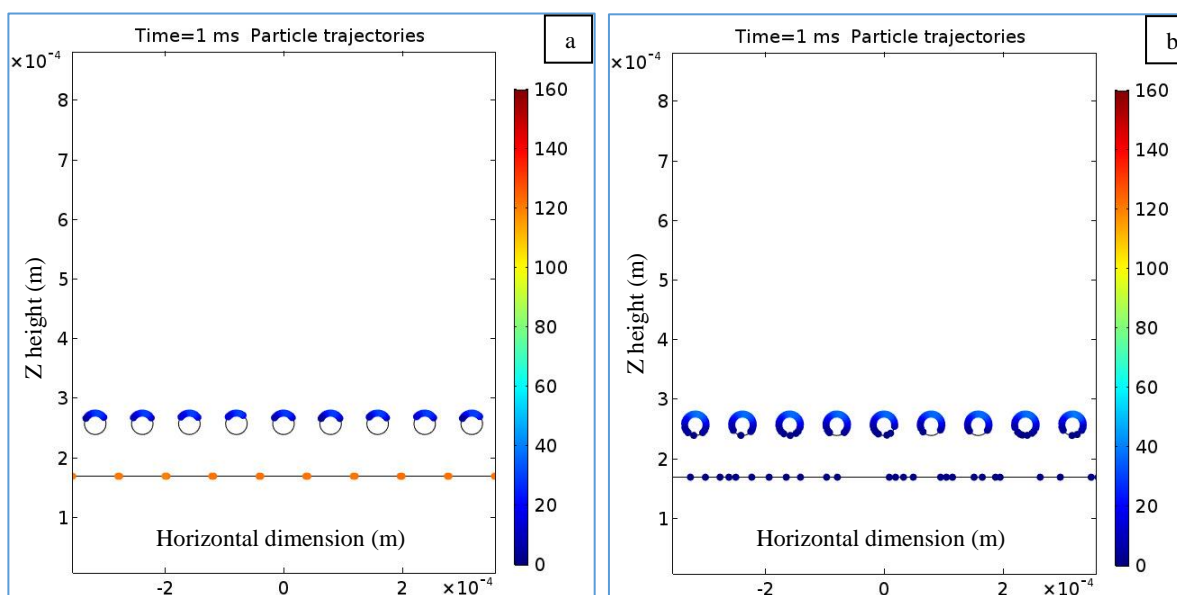


Figure 5.7: Particle deposition difference on mesh and substrate for 70 μm mesh gap: (a) 10 kV applied on the needle and 2 kV is applied on the mesh, (b) 8 kV applied on the needle and no voltage is applied on the mesh. The legend represents the velocity of the particle (m/s) and axes scale of the images is in meters.

Figure 5.7 further demonstrates how electrospray efficiency could be enhanced by focusing the electric field. While applying 2 kV resulted in focusing the charged particles through the mesh openings, the simulation results disclosed that almost all the charge particles deposit on mesh when no voltage is applied. For simplicity of the built model, the mesh material was chosen to be stainless steel only. Experimentally, the PTFE coating of the mesh contributed to enhance particles deposition. However, when no voltage was applied to the mesh, only a small amount of charged particle were able to find their way to the substrate with no obvious patterns observed (Fig. 5.7 b).

The results obtained from the particle tracing module are completely consistent with the experimental data obtained in Chapter 4 in which all mesh gaps produce favorable patterning except for the largest mesh gap used in this study, i.e., 500 μm . By using the particle counter in COMSOL for post-processing, the amount of spraying material deposited on the substrate and the mash are quantified in order to determine the patterning efficiency and the percentage of loss in raw material. Table 5.2 shows the effect of using different mesh gaps in terms of percentages of raw material deposited on mesh and substrate.

Table 5.2: Percentages of material deposited on the substrate and the mesh in addition to the loss in raw material.

Gaps (μm)	Percentage of charged particles deposited on the substrate	Percentage of charged particles deposited on the mesh	The total loss percentage of raw material
70 μm	64%	30%	36%
140 μm	55%	39%	45%
250 μm	46%	47%	54%
500 μm	37%	58%	63%
No mesh	92%	-	8%

It is clear that the efficiency of producing patterned coatings is enhanced when the mesh gap is reduced. Nevertheless, the total loss still high as compared to 8 % loss in raw material calculated by COMSOL for the typical electrospray process, when no mash is involved.

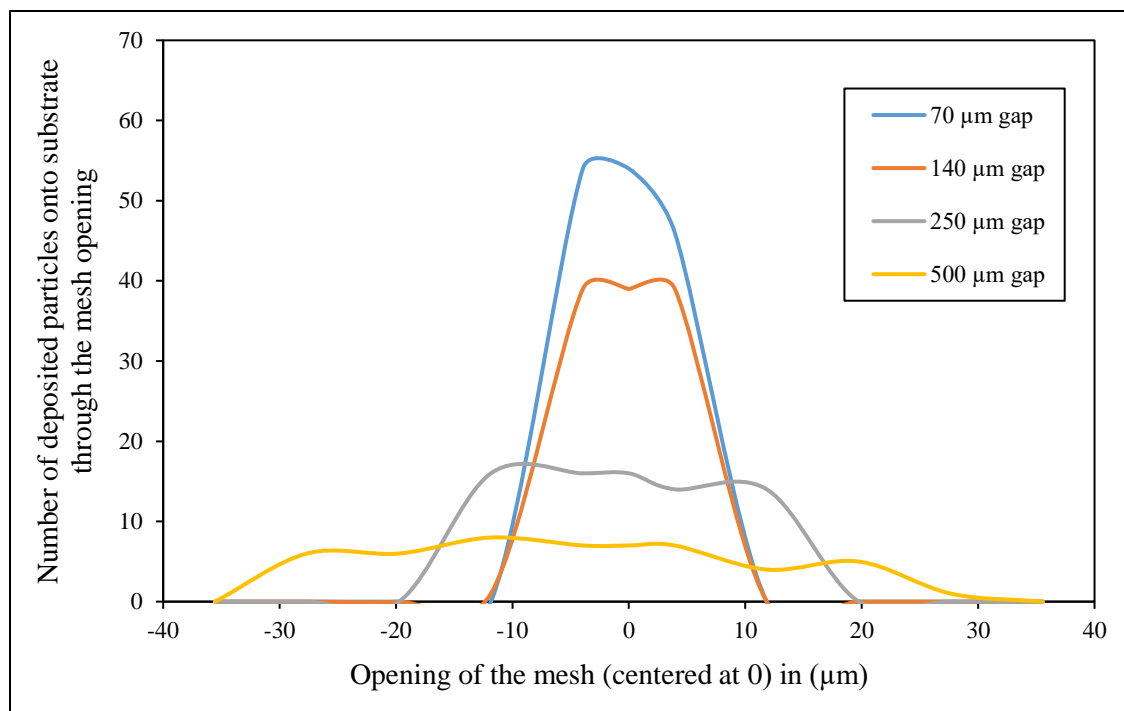


Figure 5.8: Charged particle distribution in each fabricated pillar with respect to different mesh gaps.

Figure 5.8 illustrates the particle deposition in each mesh opening with respect to different mesh gaps. The results shown in Figure 5.8 agrees very well with the experimental observations where the 70 μm gap produces tallest pillars among all the configurations and 500 μm gap gives the shortest pillars. In the model, charged particles deposit onto the substrate without affecting the potential of the grounded substrate; following particles can deposit onto the same location and stack onto the previously deposited particles. In other words, those particles are assumed to be conductive particles where the charges are dissipated instantaneously when they deposit and contact the grounded substrate. However, since the silica nanoparticles are dielectric materials, charge might be accumulated due to a relatively long charge relaxation time, which repels the following particles and spread them into a wider pillar as shown in Fig. 4.14. Nevertheless, the simulation effort in this work clearly elucidates the electrical field focusing effect and the particle

dynamics as a result of particle-electrical field interactions and particle-particle interactions in the mask-assisted electro spray.

5.6 Conclusion

In this study, COMSOL Multiphysics is employed to investigate the effect of electric field focusing on particles deposition, and to simulate and to analyze the physical processes associated with the deposition of charged particles in the mask-assisted electro spray. The electric field contours and streamlines are simulated using the electrostatic module, while the trajectory of deposited particles was simulated by incorporating the particle tracing module with the former one. The amount of spraying material deposited on the substrate and the mask are quantified in order to determine the patterning efficiency and the percentage of loss in raw material. The obtained results are completely consistent with the experimental data obtained in Chapter 4 in which all mesh gaps produce favorable patterning with well-defined profiles except for the largest mesh gap used in this study, i.e., 500 μm . The 70 μm gap produces tallest pillars among all the configurations, while the 500 μm gap gives the shortest pillars. Furthermore, the study indicated that efficiency of electro spray process with mask-assist is enhanced when a voltage with similar polarity to that applied to the needle and close mesh-substrate gaps (i.e., 70 μm) are used. Nonetheless, the total loss still high as compared to 8 % loss in raw material calculated by COMSOL for the typical electro spray process, when no mash is involved.

CHAPTER 6 Concluding Remarks

6.1 Review of results and conclusions

The main objective of this thesis has been achieved by producing SHP and SOP surfaces with low affinity toward most of the contaminants and organic solvents by a cost-effective and scalable air spray and electrospray deposition techniques. The experimental findings were corroborated with the extremely low contact angle hystereses for both the DI water and the hexadecane. This thesis also provides a thorough examination of related parameters such as the surface roughness and surface chemistry in order to establish relationships of processing-structure-property for engineering such coatings. In the air spray experiment, the surface roughness was observed to increase as the SiO₂ concentration increases. The fabricated samples with hierarchical micro/nano scale exhibited very high contact angles with low surface tension liquids when the RMS surface roughness is $\geq 4 \mu\text{m}$. The influence of different types of SiO₂ suspensions (directly-dispersed and the surfactant-dispersed suspensions) on surface morphology and surface wettability were thoroughly investigated. Both types of SiO₂ suspensions have a primary particle size of 13 nm; however, the nanoparticles tend to form much bigger agglomerates when they are directly dispersed in solvents (i.e., acetone), compared to smaller agglomerates formed in surfactant-dispersed suspensions. Furthermore, the results disclosed that creating SOP surfaces with such high contact angles is not achievable by spraying the surfactant-dispersed SiO₂ because the conditions of super-liquid repellent surfaces are not met. SOP surfaces with random hierarchical surface roughness were also demonstrated by electrospraying SiO₂ surfactant-dispersed. The fabricated samples presented low affinity toward low surface tension liquids when the surface roughness is $\geq 3.5 \mu\text{m}$. This agreement of RMS roughness between these two spray techniques indicates that the RMS roughness could be used as a general guideline in SHP and SOP surface

designs with random hierarchical roughness. More importantly, for the first time SHP and SOP surfaces have been created by a mask-assisted electrospray technique, with controlled micro-scale patterning and multiscale roughness. Micro-pillars were produced as a results of electric field focusing effect, when a voltage with similar polarity of that applied to the needle is applied to the mesh. The size of the fabricate pillars were observed to change with to the utilized substrate-mesh gap. Furthermore, Focusing the electric field enhanced particle deposition on the substrate especially for close mesh gaps (i.e, 70 μm), which in turn improved the overall efficiency of electrospray by reducing the number of particles depositing of the mesh.

By mimicking the nature of lotus leaf surface, we succeeded in creating coatings with self-cleaning properties which could be implemented in our daily life applications.

6.2 Comparison of air spray and electrospray

The air spray and electrospray employed in this works have been widely used as coating techniques for many industrial disciplines. However, each of the prior mentioned techniques has its pros and cons that must be clarified. The air spray is considered as a facile and cost-effective air-operated tool in which scalable SHP and SOP surfaces with micro/ nanoscale surface roughness could be obtained.

Air spray generates much bigger droplets with a large droplet size distribution. Accidental dripping of large droplets form defects on the coating surface where wetting failure can be initiated. On the other hand, electrospray generates finer droplets to create uniform micro/nano structured coatings, which uses much less material and produces very effective deposition and less defects in the coatings. For example, a 5-minute electrospray deposition at a flow rate of 3 $\mu\text{L}/\text{min}$. can generate

SHP and SOP surfaces, which is 15 μL solution, compared to air spraying of 3 mL of solution to create the textured SHO and SOP surfaces.

Compared to air spray, electrospray allows utilization of external means to control the nanoparticle deposition, for example, electrical field focusing of the mask-assisted electrospray employed in this study. More discussion is presented in section 6.4.

In addition, air spray method prone to suffer from a high raw material loss if the working distance and the spray gun are not carefully adjusted. This issue could be addressed by employing the electrospray in which the charge particles are forced to deposit onto a collector (the grounded substrate).

In terms of mechanical robustness of the fabricated coatings, air spray seems to give SHP and SOP surfaces with decent surface robustness. This could be attributed to the big droplet size deposited on the substrate in which the deposited silica particles could be held through interfacial surface tensions by the remaining solvent. On the contrary, the lack of coating robustness is observed when electrospray is used. This is mainly because the disintegrated nano-droplet, facilitates solvent evaporation at a faster rate. Thus, the deposited coating become nearly dry and the electrostatic interaction between the successive coating layers is not as strong to hold all the stacked silica particles, especially at long electrospray times.

6.3 Modeling of mask-assisted electrospray deposition

The main objective of the simulation has been achieved by systematically examining the effect of electric field focusing, when a voltage with the same polarity to that applied to needle is applied to the mesh, and particle trajectory in the electrical field. Furthermore, the enhancement of electrospray efficiency has been confirmed through reducing the loss of the spraying fluid and

increasing the amount of deposited material through the mesh openings. The COMSOL Multiphysics was employed to interpret and quantify the factual parameters involved in the electro spray configuration. A 2D model was created to simulate the electric field focusing effect using the electrostatic module. In addition to that, the particle tracing module was incorporated with electric field module in which relevant forces are exerted on charged particles, such as drag force, gravitational force, buoyancy force, Brownian force, electric field force, and particle-particle interactions.

In this study, two different simulation domains are used. A 53 mm × 30 mm simulation region was utilized according to the experimental geometries in order to accurately study the focusing effect of the electric field with respect to different mesh gaps. However, computing the particle trajectory with the above mentioned dimensions is prohibited due to extremely high computing cost. As a result, a simulation region of 2 mm x 2 mm is chosen since the region of interest is between the mesh and the substrate.

The results obtained from the electrostatic and particle tracing modules agree reasonably well with the experimental data in which all mesh gaps produce pillars similar to those obtained in the electro spray experiments. The simulation data also revealed that the overall efficiency of electro spray is enhanced if the mesh is placed closer to the substrate; thus, higher pillars with well-defined profiles from the deposited charged particles can be obtained. However, total loss of the spraying material is still high in case of patterned coatings as compared to 8% loss when only random hierarchical coatings are produced (i.e., without implementing the mesh in the electro spray process).

6.4 Future works

In this work, mask-assisted electro spray has been demonstrated to fabricate SHP and SOP surfaces with well-controlled pillar structures and micro/nano roughness.

Mask-assisted electro spray can also be used in fabricating different kinds of textured surfaces. By moving the fine-adjust cross-slide table in one direction at a traveling speed of 0.28 mm/s and by applying the spray settings explained in Chapter 4, traces (grooves) of silica particles was deposited on the substrate. The spraying material flow rate used in this experiment was between 3-10 $\mu\text{L}/\text{min}$ and the gaps range were between 0.5 - 1 mm which is slightly higher than that used previously for patterned samples with multiscale roughness.

By increasing or decreasing the gap between the mesh and the substrate, the width of generated silica traces increases (spreading) or decreases (focusing) accordingly (Fig. 6.1). While manipulating the gap could influence the width of silica traces, increasing or decreasing the flow rate changes the thickness of silica traces. In other words, increasing the flow rate, enables more silica particles to penetrate the mask (Fig. 6.2).

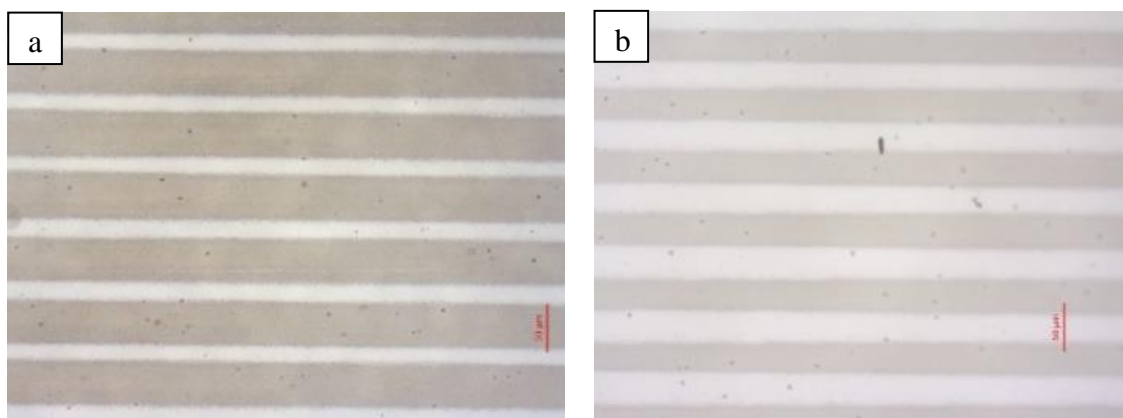


Figure 6.1: (a) microscopic picture of a sample fabricated at 1 mm mesh gap, (b) microscopic picture of a sample fabricated at 780 μm mesh gap.

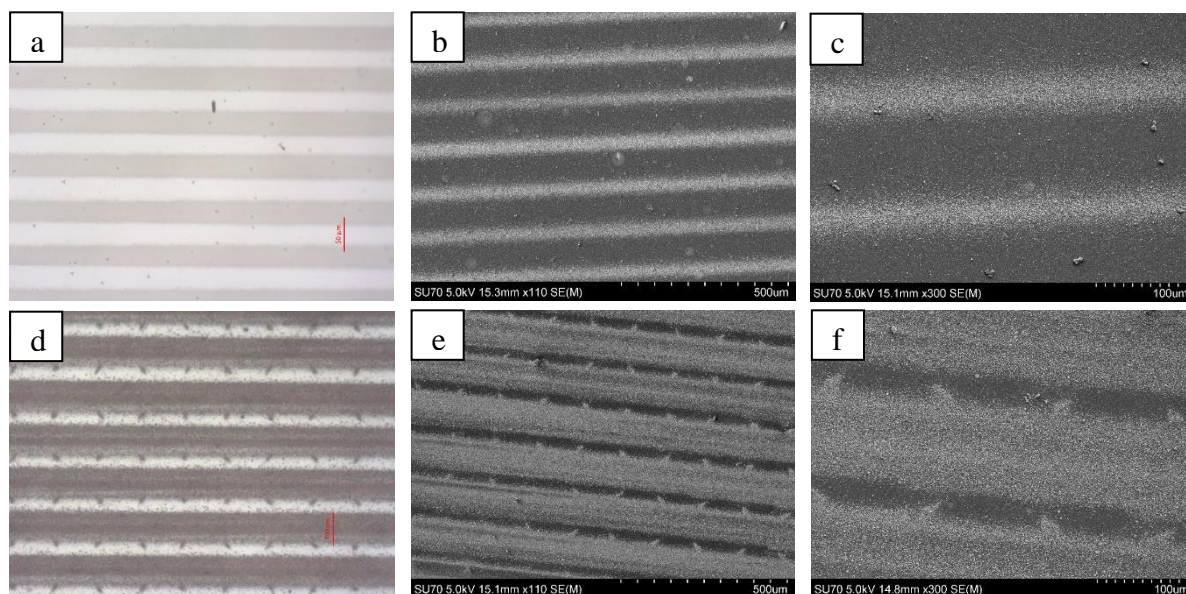


Figure 6.2: (a), (b), and (c) are pictures of a sample fabricated using 3 $\mu\text{L}/\text{min}$ material flow rate (d), (e), and (f) are pictures of a sample fabricated using 10 $\mu\text{L}/\text{min}$ material flow rate. The mesh gap for both samples was 1 mm.

The capability of creating different patterns through a mask directly from electro spray may open the gate to control the direction of the liquid droplet which can find many applications in drag reduction, microfluidics, water management in fuel cells, and inkjet printhead coatings.

For super liquid repellent coatings to survive in daily life applications, two crucial factors must be available such as coatings' mechanical robustness and coating wettability robustness. In fact, these two aspects are quite different from each other. Wetting robustness is defined as the surface ability to resist the external stimuli (e.g. vibration, or pressure). As explained in the literature review, the wetting robustness could be enhanced by combining the hierarchical structure with the low surface energy. The fabricated coatings in this study could survive the impact of water droplets at high release distances (higher than 1 m). However, it is still very challenging for such surfaces to survive against high impacting pressures exerted by low tension liquids from such high distances. Similarly, the coating robustness, which is represented by the mechanical resistivity against abrasions and extreme weather conditions, is another issue to be tackled. One of the good solutions

proposed is to coat the substrate by epoxy as a base layer on which silica particles could be added to provide the required multiscale hierarchical surface roughness.

Although enormous efforts have been devoted so far to mimic the self-cleaning property of lotus leaf, a significant work remains unfinished particularly for the above-named obstacles so that mechanically and functionally robust SHP and SOP coatings can be manufactured and implemented in our daily life applications.

References

- (1) Solga, A.; Cerman, Z.; Striffler, B. F.; Spaeth, M.; Barthlott, W. The Dream of Staying Clean: Lotus and Biomimetic Surfaces. *Bioinspir. Biomim.* **2007**, *2*, S126–S134.
- (2) Barthlott, W.; Neinhuis, C. Purity of the Sacred Lotus, or Escape from Contamination in Biological Surfaces. *Planta* **1997**, *202*, 1–8.
- (3) Patankar, N. A. Mimicking the Lotus Effect: Influence of Double Roughness Structures and Slender Pillars. *Langmuir* **2004**, *20*, 8209–8213.
- (4) Su, Y.; Ji, B.; Huang, Y.; Hwang, K. C. Nature's Design of Hierarchical Superhydrophobic Surfaces of a Water Strider for Low Adhesion and Low-Energy Dissipation. *Langmuir* **2010**, *26*, 18926–18937.
- (5) Tuteja, A.; Choi, W.; Ma, M.; Mabry, J. M.; Mazzella, S. A.; Rutledge, G. C.; McKinley, G. H.; Cohen, R. E. Designing Superoleophobic Surfaces. *Science (80-.)*. **2007**, *318*, 1618–1622.
- (6) Law, K. Y.; Zhao, H. *Surface Wetting: Characterization, Contact Angle, and Fundamentals*; 2015.
- (7) Young, T. An Essay on the Cohesion of Fluids. *Philos. Trans. R. Soc. London* **1805**, *95*, 65–87.
- (8) Wenzel, R. N. RESISTANCE OF SOLID SURFACES TO WETTING BY WATER. *Ind. Eng. Chem.* **1936**, *28*, 988–994.
- (9) Liu, K.; Tian, Y.; Jiang, L. Bio-Inspired Superoleophobic and Smart Materials: Design,

- Fabrication, and Application. *Progress in Materials Science*, 2012.
- (10) Cassie, A. B. D.; Baxter, S. Wettability of Porous Surfaces. *Trans. Faraday Soc.* **1944**, *40*, 546–551.
 - (11) Bhushan, B.; Her, E. K. Fabrication of Superhydrophobic Surfaces with High and Low Adhesion Inspired from Rose Petal. *Langmuir* **2010**, *26*, 8207–8217.
 - (12) Zhao, H.; Law, K.-Y.; Sambhy, V. Fabrication, Surface Properties, and Origin of Superoleophobicity for a Model Textured Surface. *Langmuir* **2011**, *27*, 5927–5935.
 - (13) Steele, A.; Bayer, I.; Loth, E. Inherently Superoleophobic Nanocomposite Coatings by Spray Atomization. *Nano Lett.* **2009**, *9*, 501–505.
 - (14) Zhao, H.; Park, K.-C.; Law, K.-Y. Effect of Surface Texturing on Superoleophobicity, Contact Angle Hysteresis, and “Robustness.” *Langmuir* **2012**, *28*, 14925–14934.
 - (15) Choi, W.; Tuteja, A.; Chhatre, S.; Mabry, J. M.; Cohen, R. E.; McKinley, G. H. Fabrics with Tunable Oleophobicity. *Adv. Mater.* **2009**, *21*, 2190–2195.
 - (16) Kota, A. K.; Li, Y.; Mabry, J. M.; Tuteja, A. Hierarchically Structured Superoleophobic Surfaces with Ultralow Contact Angle Hysteresis. *Adv. Mater.* **2012**, *24*, 5838–5843.
 - (17) Campos, R.; Guenther, A. J.; Meuler, A. J.; Tuteja, A.; Cohen, R. E.; McKinley, G. H.; Haddad, T. S.; Mabry, J. M. Superoleophobic Surfaces through Control of Sprayed-on Stochastic Topography. *Langmuir* **2012**, *28*, 9834–9841.
 - (18) Brown, P. S.; Bhushan, B. Mechanically Durable, Superoleophobic Coatings Prepared by Layer-by-Layer Technique for Anti-Smudge and Oil-Water Separation. *Sci. Rep.* **2015**, *5*,

- 8701.
- (19) Chen, Y.; Zhang, Y.; Shi, L.; Li, J.; Xin, Y.; Yang, T.; Guo, Z. Transparent Superhydrophobic/superhydrophilic Coatings for Self-Cleaning and Anti-Fogging. *Appl. Phys. Lett.* **2012**, *101*.
- (20) Lai, Y.; Tang, Y.; Gong, J.; Gong, D.; Chi, L.; Lin, C.; Chen, Z. Transparent Superhydrophobic/superhydrophilic TiO₂-Based Coatings for Self-Cleaning and Anti-Fogging. *J. Mater. Chem.* **2012**, *22*, 7420–7426.
- (21) Fürstner, R.; Barthlott, W.; Neinhuis, C.; Walzel, P. Wetting and Self-Cleaning Properties of Artificial Superhydrophobic Surfaces. *Langmuir* **2005**, *21*, 956–961.
- (22) Aljallis, E.; Sarshar, M. A.; Datla, R.; Sikka, V.; Jones, A.; Choi, C. H. Experimental Study of Skin Friction Drag Reduction on Superhydrophobic Flat Plates in High Reynolds Number Boundary Layer Flow. *Phys. Fluids* **2013**, *25*.
- (23) Song, D.; Daniello, R. J.; Rothstein, J. P. Drag Reduction Using Superhydrophobic Sanded Teflon Surfaces. *Exp. Fluids* **2014**, *55*.
- (24) Tian, X.; Verho, T.; Ras, R. H. A. Moving Superhydrophobic Surfaces toward Real-World Applications. *Science (80-.)*. **2016**, *352*, 142–143.
- (25) Gao, L.; McCarthy, T. J.; Zhang, X. Wetting and Superhydrophobicity. *Langmuir* **2009**, *25*, 14100–14104.
- (26) Liu, K.; Jiang, L. Bio-Inspired Self-Cleaning Surfaces. *Annu. Rev. Mater. Res.* **2012**, *42*, 231–263.

- (27) Samaha, M. A.; Ochanda, F. O.; Tafreshi, H. V.; Tepper, G. C.; Gad-El-Hak, M. In Situ, Noninvasive Characterization of Superhydrophobic Coatings. *Rev. Sci. Instrum.* **2011**, *82*.
- (28) Neinhuis, C.; Barthlott, W. Characterization and Distribution of Water-Repellent, Self-Cleaning Plant Surfaces. *Ann. Bot.* **1997**, *79*, 667–677.
- (29) Bharathidasan, T.; Narayanan, T. N.; Sathyanaryanan, S.; Sreejakumari, S. S. Above 170° Water Contact Angle and Oleophobicity of Fluorinated Graphene Oxide Based Transparent Polymeric Films. *Carbon N. Y.* **2015**, *84*, 207–213.
- (30) Cha, T.-G.; Yi, J. W.; Moon, M.-W.; Lee, K.-R.; Kim, H.-Y. Nanoscale Patterning of Microtextured Surfaces to Control Superhydrophobic Robustness. *Langmuir* **2010**, *26*, 8319–8326.
- (31) Öner, D.; McCarthy, T. J. Ultrahydrophobic Surfaces. Effects of Topography Length Scales on Wettability. *Langmuir* **2000**, *16*, 7777–7782.
- (32) Ming, W.; Wu, D.; Van Benthem, R.; De With, G. Superhydrophobic Films from Raspberry-like Particles. *Nano Lett.* **2005**, *5*, 2298–2301.
- (33) Mammen, L.; Bley, K.; Papadopoulos, P.; Schellenberger, F.; Encinas, N.; Butt, H.-J.; Weiss, C. K.; Vollmer, D. Functional Superhydrophobic Surfaces Made of Janus Micropillars. *Soft Matter* **2014**, *11*, 506–515.
- (34) Kota, A. K.; Kwon, G.; Tuteja, A. The Design and Applications of Superomniphobic Surfaces. *NPG Asia Mater.* **2014**, *6*, e109.
- (35) Kim, J.-Y.; Kim, E.-K.; Kim, S. S. Micro-Nano Hierarchical Superhydrophobic

- Electrospray-Synthesized Silica Layers. *J. Colloid Interface Sci.* **2013**, *392*, 376–381.
- (36) Li, W.; Amirfazli, A. Hierarchical Structures for Natural Superhydrophobic Surfaces. *Soft Matter* **2008**, *4*, 462–466.
- (37) Yu, Y.; Zhao, Z. H.; Zheng, Q. S. Mechanical and Superhydrophobic Stabilities of Two-Scale Surface Structure of Lotus Leaves. *Langmuir* **2007**, *23*, 8212–8216.
- (38) Nosonovsky, M. Multiscale Roughness and Stability of Superhydrophobic Biomimetic Interfaces. *Langmuir* **2007**, *23*, 3157–3161.
- (39) Su, Y.; Ji, B.; Zhang, K.; Gao, H.; Huang, Y.; Hwang, K. Nano to Micro Structural Hierarchy Is Crucial for Stable Superhydrophobic and Water-Repellent Surfaces. *Langmuir* **2010**, *26*, 4984–4989.
- (40) Extrand, C. W. Repellency of the Lotus Leaf: Resistance to Water Intrusion under Hydrostatic Pressure. *Langmuir* **2011**, *27*, 6920–6925.
- (41) Gao, L.; McCarthy, T. J. The “lotus Effect” explained: Two Reasons Why Two Length Scales of Topography Are Important. *Langmuir* **2006**, *22*, 2966–2967.
- (42) Liu, H. H.; Zhang, H. Y.; Li, W. Thermodynamic Analysis on Wetting Behavior of Hierarchical Structured Superhydrophobic Surfaces. *Langmuir* **2011**, *27*, 6260–6267.
- (43) Li, J., Xu, J., Du, F., Xu, C., & Yu, H. Superhydrophobic Properties of Multiple Coupling. In Manipulation, Manufacturing and Measurement on the Nanoscale (3M-NANO). *IEEE* **2013**, pp. 385–388.
- (44) Feng, L.; Li, S.; Li, Y.; Li, H.; Zhang, L.; Zhai, J.; Song, Y.; Liu, B.; Jiang, L.; Zhu, D.

- Super-Hydrophobic Surfaces: From Natural to Artificial. *Adv. Mater.* **2002**, *14*, 1857–1860.
- (45) Cha, T. G.; Yi, J. W.; Moon, M. W.; Lee, K. R.; Kim, H. Y. Nanoscale Patterning of Microtextured Surfaces to Control Superhydrophobic Robustness. *Langmuir* **2010**, *26*, 8319–8326.
- (46) Helbig, R.; Nickerl, J.; Neinhuis, C.; Werner, C. Smart Skin Patterns Protect Springtails. *PLoS One* **2011**, *6*.
- (47) Ahuja, A.; Taylor, J. A.; Lifton, V.; Sidorenko, A. A.; Salamon, T. R.; Lobaton, E. J.; Kolodner, P.; Krupenkin, T. N. Nanonails: A Simple Geometrical Approach to Electrically Tunable Superlyophobic Surfaces. *Langmuir* **2008**, *24*, 9–14.
- (48) Ochanda, F. O.; Samaha, M. A.; Tafreshi, H. V.; Tepper, G. C.; Gad-El-Hak, M. Fabrication of Superhydrophobic Fiber Coatings by DC-Biased AC-Electrospinning. *J. Appl. Polym. Sci.* **2012**, *123*, 1112–1119.
- (49) Zheng, J.; He, A.; Li, J.; Xu, J.; Han, C. C. Studies on the Controlled Morphology and Wettability of Polystyrene Surfaces by Electrospinning or Electrospraying. *Polymer (Guildf)*. **2006**, *47*, 7095–7102.
- (50) Sas, I.; Gorga, R. E.; Joines, J. A.; Thoney, K. A. Literature Review on Superhydrophobic Self-Cleaning Surfaces Produced by Electrospinning. *Journal of Polymer Science, Part B: Polymer Physics*, 2012, *50*, 824–845.
- (51) Yohe, S. T.; Grinstaff, M. W. A Facile Approach to Robust Superhydrophobic 3D

- Coatings via Connective-Particle Formation Using the Electrospraying Process. *Chem. Commun.* **2013**, *49*, 804–806.
- (52) Sweet, M. L.; Pestov, D.; Tepper, G. C.; McLeskey Jr., J. T. Electro Spray Aerosol Deposition of Water Soluble Polymer Thin Films. *Appl. Surf. Sci.* **2014**, *289*, 150–154.
- (53) Jaworek, A., Sobczyk, A., Krupa, A., Lackowski, M., & Czech, T. Electrostatic Deposition of Nanothin Films on Metal Substrate. *Bulletin of the Polish Academy of Sciences: Technical Sciences*, 2009, *57*, 63.
- (54) Burkarter, E.; Saul, C. K.; Thomazi, F.; Cruz, N. C.; Roman, L. S.; Schreiner, W. H. Superhydrophobic Electrosprayed PTFE. *Surf. Coatings Technol.* **2007**, *202*, 194–198.
- (55) Bravo, J.; Zhai, L.; Wu, Z.; Cohen, R. E.; Rubner, M. F. Transparent Superhydrophobic Films Based on Silica Nanoparticles. *Langmuir* **2007**, *23*, 7293–7298.
- (56) Martines, E.; Seunarine, K.; Morgan, H.; Gadegaard, N.; Wilkinson, C. D. W.; Riehle, M. O. Superhydrophobicity and Superhydrophilicity of Regular Nanopatterns. *Nano Lett.* **2005**, *5*, 2097–2103.
- (57) Fürstner, R.; Barthlott, W.; Neinhuis, C.; Walzel, P. Wetting and Self-Cleaning Properties of Artificial Superhydrophobic Surfaces. *Langmuir* **2005**, *21*, 956–961.
- (58) Zhao, H.; Law, K. Y. Directional Self-Cleaning Superoleophobic Surface. *Langmuir* **2012**, *28*, 11812–11818.
- (59) Celia, E.; Darmanin, T.; Taffin de Givenchy, E.; Amigoni, S.; Guittard, F. Recent Advances in Designing Superhydrophobic Surfaces. *Journal of Colloid and Interface*

- Science*, 2013, 402, 1–18.
- (60) Ma, M.; Hill, R. M. Superhydrophobic Surfaces. *Curr. Opin. Colloid Interface Sci.* **2006**, 11, 193–202.
- (61) Srinivasan, S.; Choi, W.; Park, K.-C.; Chhatre, S. S.; Cohen, R. E.; McKinley, G. H. Drag Reduction for Viscous Laminar Flow on Spray-Coated Non-Wetting Surfaces. *Soft Matter* **2013**, 9, 5691–5702.
- (62) Tourkine, P.; Merrer, M. Le; Quéré, D. Delayed Freezing on Water Repellent Materials. *Langmuir* **2009**, 25, 7214–7216.
- (63) Hong, B. S.; Han, J. H.; Kim, S. T.; Cho, Y. J.; Park, M. S.; Dolukhanyan, T.; Sung, C. Endurable Water-Repellent Glass for Automobiles. *Thin Solid Films* **1999**, 351, 274–278.
- (64) Kota, A. K.; Kwon, G.; Choi, W.; Mabry, J. M.; Tuteja, A. Hygro-Responsive Membranes for Effective Oil-Water Separation. *Nat. Commun.* **2012**, 3, 1025.
- (65) Gao, J. Z.; Li, Y. P.; Li, Y.; Liu, H. W.; Yang, W. Fabrication of Superhydrophobic Surface of Stearic Acid Grafted Zinc by Using an Aqueous Plasma Etching Technique. *Cent. Eur. J. Chem.* **2012**, 10, 1766–1772.
- (66) Lee, J.-H.; Lee, S. H.; Kim, D.; Park, Y. S. The Structural and Surface Properties of Carbon Nanotube Synthesized by Microwave Plasma Chemical Vapor Deposition Method for Superhydrophobic Coating. *Thin Solid Films* **2013**, 546, 94–97.
- (67) Cui, Z.; Ding, J.; Scoles, L.; Wang, Q.; Chen, Q. Superhydrophobic Surfaces Fabricated by Spray-Coating Micelle Solutions of Comb Copolymers. *Colloid Polym. Sci.* **2013**, 291,

- 1409–1418.
- (68) Pham, N. P. N.; Burghartz, J. N. J.; Sarro, P. P. M. Spray Coating of Photoresist for Pattern Transfer on High Topography Surfaces. *J. Micromechanics Microengineering* **2005**, *15*, 691–697.
- (69) Li, X.; Du, X.; He, J. Self-Cleaning Antireflective Coatings Assembled from Peculiar Mesoporous Silica Nanoparticles. *Langmuir* **2010**, *26*, 13528–13534.
- (70) Du, X.; Li, X.; He, J. Facile Fabrication of Hierarchically Structured Silica Coatings from Hierarchically Mesoporous Silica Nanoparticles and Their Excellent Superhydrophilicity and Superhydrophobicity. *ACS Appl. Mater. Interfaces* **2010**, *2*, 2365–2372.
- (71) Lee, K. K.; Ahn, C. H. Superhydrophilic Multilayer Silica Nanoparticle Networks on a Polymer Microchannel Using a Spray Layer-by-Layer Nanoassembly Method. *ACS Appl. Mater. Interfaces* **2013**, *5*, 8523–8530.
- (72) Wang, S.; Jiang, L. Definition of Superhydrophobic States. *Adv. Mater.* **2007**, *19*, 3423–3424.
- (73) Deng, X.; Mammen, L.; Zhao, Y.; Lellig, P.; Müllen, K.; Li, C.; Butt, H. J.; Vollmer, D. Transparent, Thermally Stable and Mechanically Robust Superhydrophobic Surfaces Made from Porous Silica Capsules. *Adv. Mater.* **2011**, *23*, 2962–2965.
- (74) Mizukoshi, T.; Matsumoto, H.; Minagawa, M.; Tanioka, A. Control over Wettability of Textured Surfaces by Electrospray Deposition. *J. Appl. Polym. Sci.* **2007**, *103*, 3811–3817.

- (75) Choi, K. R. and A. K. and N. M. M. and J. J. and K.-H. Fine-Resolution Patterning of Copper Nanoparticles through Electrohydrodynamic Jet Printing. *J. Micromechanics Microengineering* **2012**, 22, 65012.
- (76) Xie, J.; Jiang, J.; Davoodi, P.; Srinivasan, M. P.; Wang, C.-H. Electrohydrodynamic Atomization: A Two-Decade Effort to Produce and Process Micro-/nanoparticulate Materials. *Chem. Eng. Sci.* **2015**, 125, 32–57.
- (77) Li, X. Electrohydrodynamic Deposition and Patterning of Nano-Hydroxyapatite for Biomedical Applications, 2009.
- (78) Zeleny, J. The Electrical Discharge from Liquid Points, and a Hydrostatic Method of Measuring the Electric Intensity at Their Surfaces. *Phys. Rev.* **1914**, 3, 69–91.
- (79) Jaworek, A. Electro spray Droplet Sources for Thin Film Deposition. *J. Mater. Sci.* **2007**, 42, 266–297.
- (80) Lee, A.; Jin, H.; Dang, H.-W.; Choi, K.-H.; Ahn, K. H. Optimization of Experimental Parameters To Determine the Jetting Regimes in Electrohydrodynamic Printing. *Langmuir* **2013**, 29, 13630–13639.
- (81) Chen, X.; Jia, L.; Yin, X.; Cheng, J.; Lu, J. Spraying Modes in Coaxial Jet Electro spray with Outer Driving Liquid. *Phys. Fluids* **2005**, 17.
- (82) Chen, D.-R.; Pui, D. Y. H.; Kaufman, S. L. Electro spraying of Conducting Liquids for Monodisperse Aerosol Generation in the 4 Nm to 1.8 Mm Diameter Range. *J. Aerosol Sci.* **1995**, 26, 963–977.

- (83) Licari, J. J. Coating Materials for Electronic Applications - Polymers, Processes, Reliability, Testing.
- (84) Xie, J.; Rezvanpour, A.; Wang, C. H.; Hua, J. Electric Field Controlled Electro spray Deposition for Precise Particle Pattern and Cell Pattern Formation. *AIChE J.* **2010**, *56*, 2607–2621.
- (85) Rezvanpour, A.; Wang, C.-H. Computational and Experimental Studies of Electro spray Deposition Process in Pharmaceutical Micro-Pattern Formation. *Chem. Eng. Sci.* **2011**, *66*, 3836–3849.
- (86) Xu, Z. N. An Algorithm for Selecting the Most Accurate Protocol for Contact Angle Measurement by Drop Shape Analysis. *Rev. Sci. Instrum.* **2014**, *85*.
- (87) Zhang, X.; Shi, F.; Niu, J.; Jiang, Y.; Wang, Z. Superhydrophobic Surfaces: From Structural Control to Functional Application. *J. Mater. Chem.* **2008**, *18*, 621–633.
- (88) Ybert, C.; Barentin, C.; Cottin-Bizonne, C.; Joseph, P.; Bocquet, L. Achieving Large Slip with Superhydrophobic Surfaces: Scaling Laws for Generic Geometries. *Phys. Fluids* **2007**, *19*.
- (89) Sung, C. J.; Law, C. K.; L Axelbaum, R. Thermophoretic Effects on Seeding Particles in LDV Measurements of Flames. *Combust. Sci. Technol.* **1994**, *99*, 119–132.
- (90) Hinds, W. C. *Aerosol Technology: Properties, Behavior, and Measurement of Airborne Particles*; 2012; Vol. 1.
- (91) Gañán-Calvo, A. M. On the General Scaling Theory for Electro spraying. *J. Fluid Mech.*

2004, 507, 203–212.

- (92) Gañan-Calvo, A. M. Abstracts of the 1994 European Aerosol Conference 20.O.05 The Size and Charge of Droplets in the Electro spraying of Polar Liquids in Cone-Jet Mode, and the Minimum Droplet Size. *J. Aerosol Sci.* **1994**, 25, 309–310.
- (93) Wilm, M. Principles of Electrospray Ionization. *Mol. Cell. Proteomics* **2011**, 10, M111.009407.
- (94) Wang, R.; Zenobi, R. Evolution of the Solvent Polarity in an Electrospray Plume. *J. Am. Soc. Mass Spectrom.* **2010**, 21, 378–385.

Appendix A: Modeling Instructions

Modeling instructions for simulating the electric field

NEW

1. From the **File** menu, choose **New**.

MODEL WIZARD

1. In the **New** window, click **Model Wizard**.
 1. In the **Model Wizard** window, click **2D**.
 2. In the **Select physics** tree, select **AC/DC>Electrostatics (ec)**.
 3. Click **Add**.
 4. Click **Study**.
 5. In the **Select study** tree, select **Preset Studies>Stationary**.
 6. Click **Done**.

Geometry 1

1. In the **Model Builder** window, under **Component 1 (comp1)** click **Geometry 1**.
2. In the **Settings** window for **Geometry**, locate the **Units** section.
3. From the **Length unit** list, choose **m**.

Circle 1

1. Right-click **Component 1> Geometry 1** and choose **Circle**.
2. In the **Settings** window for **Circle**, locate the **Size and Shape** section.
3. In the **Radius** text field, type 0.000018.
4. Locate the **Position** section.
5. In **Y** text field type 0.000258.

6. Locate the **Position** section. From the **Base** list, choose **Center**.

Circle 2

1. Right-click **Component 1> Geometry 1** and choose **Circle**.
2. In the Settings window for **Circle**, locate the **Size and Shape** section.
3. In the **Radius** text field, type 0.000018.
4. Locate the **Position** section.
5. In **X** text field type 0.000079.
6. In **Y** text field type 0.000258.
7. Locate the **Position** section. From the **Base** list, choose **Center**.

Circle 3

1. Right-click **Component 1> Geometry 1** and choose **Circle**.
2. In the Settings window for **Circle**, locate the **Size and Shape** section.
3. In the **Radius** text field, type 0.000018.
4. Locate the **Position** section.
5. In **X** text field type -0.000079.
6. In **Y** text field type 0.000258.
7. Locate the **Position** section. From the **Base** list, choose **Center**.

Repeat these steps till you construct 256 circles taking in consideration the spacing between each circle with is 79 μm .

Rectangle 1

1. Right-click **Component 1> Geometry 1** and choose **Rectangle**.
2. In the Settings window for **Rectangle**, locate the **Size and Shape** section.

3. In the **Width** text field, type 0.03.
4. In the **Height** text field, type 0.053.
5. Locate the **Position** section.
6. In **X** text field type - 0.015.
7. Locate the **Position** section. From the **Base** list, choose **Center**.

Rectangle 2

1. Right-click **Component 1 > Geometry 1** and choose **Rectangle**.
2. In the Settings window for **Rectangle**, locate the **Size and Shape** section.
3. In the **Width** text field, type 0.02.
4. In the **Height** text field, type 0.00017.
5. Locate the **Position** section.
6. In **X** text field type - 0.01.
7. Locate the **Position** section. From the **Base** list, choose **Center**.

Rectangle 3

1. Right-click **Component 1 > Geometry 1** and choose **Rectangle**.
2. In the Settings window for **Rectangle**, locate the **Size and Shape** section.
3. In the **Width** text field, type 0.0005.
4. In the **Height** text field, type 0.0005.
5. Locate the **Position** section.
6. In **X** text field type - 0.00055.
7. In **Y** text field type - 0.0525.
8. Locate the **Position** section. From the **Base** list, choose **Center**.
9. Click the **Build All Objects** button.

Difference 1

1. Right-click **Component 1 > Geometry 1 > Booleans and partitions** and choose **Difference**.
2. In the Settings window for **Difference**, locate the **Difference** section.
3. In **Objects to add** field select **Rectangle 1**.
4. In **Objects to subtract** field select **Rectangle 2, Rectangle 3,** and select **Circle 1** to **Circle 256**.
5. Click the **Build All Objects** button.

After the last step, the setup should look like Figure A.1.

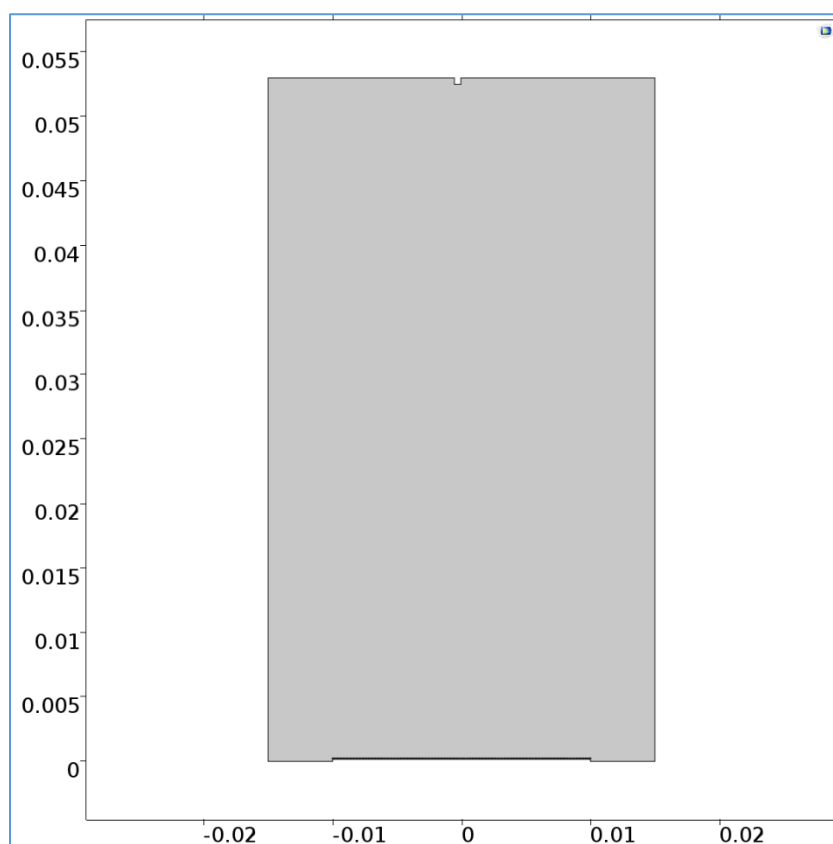


Figure A.1: Electro spray setup with the same experimental setup dimensions.

Definitions

Explicit 1

1. On the **Definitions** toolbar, click **Explicit**.
2. In the Settings window for **Explicit 1**, locate the **label** text field and type Air Domain.
3. In **Geometric entity level** section, select **Domain** from the menu then click on **Rectangle 1** in the graphics window only.

Explicit 2

1. On the **Definitions** toolbar, click **Explicit**.
2. In the Settings window for **Explicit 2**, locate the **label** text field and type Mesh.
3. In **Geometric entity level** section, select **Boundary** from the menu then click on **Circle 1 to Circle 256** in the graphics window only.

Explicit 3

1. On the **Definitions** toolbar, click **Explicit**.
2. In the Settings window for **Explicit 3**, locate the **label** text field and type Substrate.
3. In **Geometric entity level** section, select **Domain** from the menu then click on **Rectangle 2** in the graphics window only.

Explicit 4

1. On the **Definitions** toolbar, click **Explicit**.
2. In the Settings window for **Explicit 4**, locate the **label** text field and type Needle.
3. In **Geometric entity level** section, select **Domain** from the menu then click on **Rectangle 3** in the graphics window only.

MATERIALS

1. In **Model Builder** window, under **Component 1** right-click **Materials** and choose **Add Material**.
2. In **Add Material** window, locate the Build-In menu then select Air.
3. In **Model Builder** window, under **Component 1 > Materials > Air** locate the **Material Contents** section.
4. In **Relative permittivity** type 1 in **Value** text field.

Electrostatics

Ground 1

1. On **Physics** toolbar, click **Boundaries** and choose **Ground**.
2. Select boundary 5 only (the substrate).

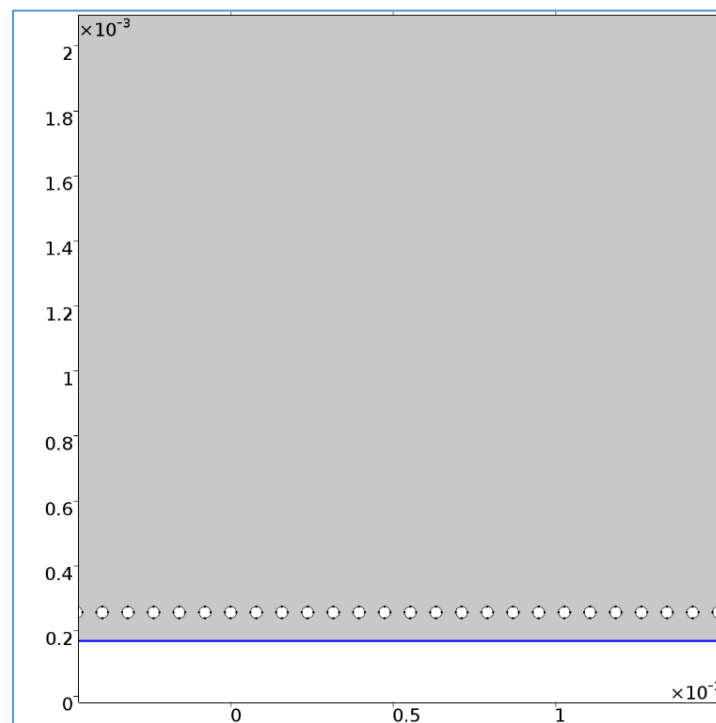


Figure A.2: Grounded substrate.

Electric Potential 1

1. On **Physics** toolbar, click **Boundaries** and choose **Electric Potential**.
2. In **Model Builder** window, under **Component 1** > **Electrostatic (es)** > **Electric Potential**
1 select **Boundary 5**.
3. Locate the **Electric Potential** section.
4. In **Electric Potential** text field type 10000.

Electric Potential 2

1. On **Physics** toolbar, click **Boundaries** and choose **Electric Potential**.
2. In **Model Builder** window, under **Component 1** > **Electrostatic (es)** > **Electric Potential**
2 select **Circle 1** to **Circle 256**.
3. Locate the **Electric Potential** section.
4. In **Electric Potential** text field type 2000.

Mesh 1

1. In **Model Builder** window, under **Component 1** right-click **Mesh 1**.
2. In **Mesh 1** setting window, locate the **Mesh Settings** section.
3. In **Element size** menu choose **Extremely fine**.
4. Click **Build All** button. (See Fig. A.3 below).

Study 1

On the **Study** toolbar, click **Compute**.

Results

Next, add a contour plot showing the electric potential.

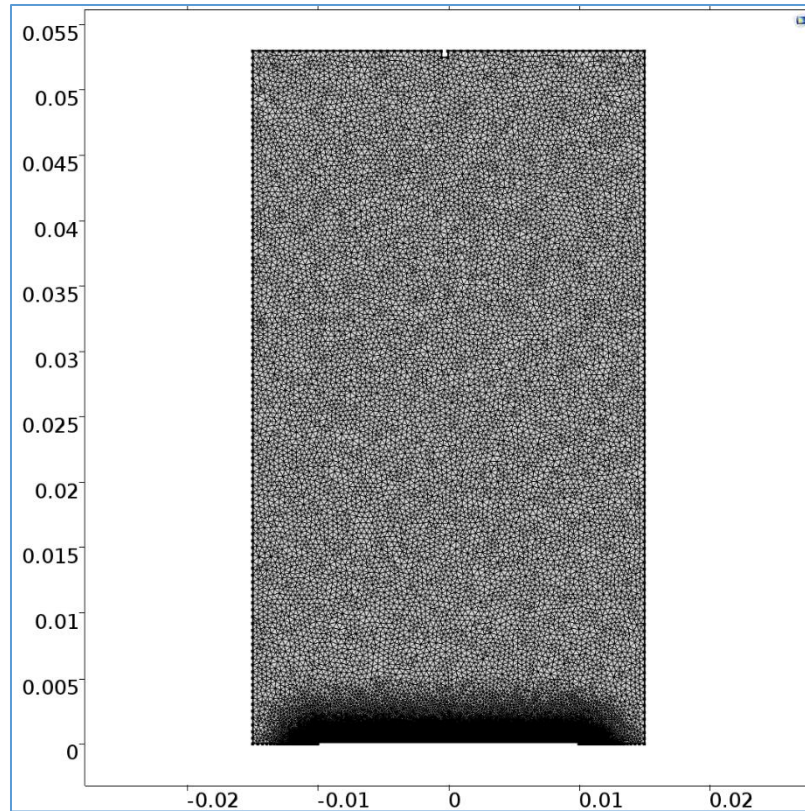


Figure A.3: Meshing the calculation domain.

1. In the **Model Builder** window, under **Results** right-click **Electric Potential (ec)** and choose **Surface 1**.
2. In the setting window of the **Streamline**, click **Expression** in the upper-right corner of the **Expression** section. From the menu choose **Component 1 > Electrostatics > Electric > es.normE – Electric field norm**.
3. Locate the **Coloring and Style** section. From the **Color table** list, choose **GrayPrint**.
4. Clear the **Color legend** check box.
5. Select the **Reverse color table** check box.
6. In the **Model Builder** window, under **Results** right-click **Electric Potential (ec)** and choose **Streamline**.

7. In the setting window of the **Contour**, click **Expression** in the upper-right corner of the **Expression** section. From the menu choose **Component 1 > Electrostatics > Electric > es.Ex, es.Ey – Electric Field**.
8. Locate the **Streamline Positioning** section. From the **Positioning** list, choose **Uniform Density**.
9. Locate the **Coloring and Style** section. From Separating distance text field type 0.0008.
10. From the **Line type** menu choose **Line** and from the **Color table** list, choose **Blue**.
11. Click **Plot** button.

Modeling instructions for simulating particle trajectories

From the **File** menu, choose **New**.

NEW

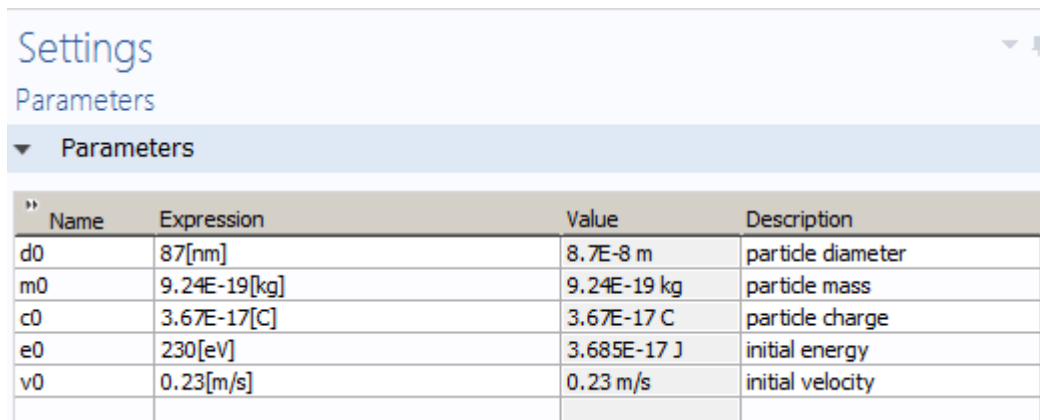
MODEL WIZARD

1. In the **New** window, click **Model Wizard**.
 1. In the **Model Wizard** window, click **2D**.
 2. In the **Select physics** tree, select **AC/DC>Electrostatics (ec)**.
 3. Click **Add**.
 4. Click **Study**.
 5. In the **Select study** tree, select **Preset Studies>Stationary**.
 6. Click **Done**.

Global Definition

Parameters

1. On the **Home** toolbar, click **Parameters**.
2. In the **settings** window for Parameters, locate the **Parameters** section.
3. In the table enter the following settings:



Name	Expression	Value	Description
d0	87[nm]	8.7E-8 m	particle diameter
m0	9.24E-19[kg]	9.24E-19 kg	particle mass
c0	3.67E-17[C]	3.67E-17 C	particle charge
e0	230[eV]	3.685E-17 J	initial energy
v0	0.23[m/s]	0.23 m/s	initial velocity

Geometry 1

1. In the **Model Builder** window, under **Component 1 (comp1)** click **Geometry 1**.
2. In the **Settings** window for Geometry, locate the **Units** section.
3. From the **Length unit** list, choose **m**.

Circle 1

1. Right-click **Component 1 > Geometry 1** and choose **Circle**.
2. In the Settings window for **Circle**, locate the **Size and Shape** section.
3. In the **Radius** text field, type 0.000018.
4. Locate the **Position** section.
5. In **Y** text field type 0.000258.

6. Locate the **Position** section. From the **Base** list, choose **Center**.

Circle 2

1. Right-click **Component 1> Geometry 1** and choose **Circle**.
2. In the Settings window for **Circle**, locate the **Size and Shape** section.
3. In the **Radius** text field, type 0.000018.
4. Locate the **Position** section.
5. In **X** text field type 0.000079.
6. In **Y** text field type 0.000258.
7. Locate the **Position** section. From the **Base** list, choose **Center**.

Circle 3

1. Right-click **Component 1> Geometry 1** and choose **Circle**.
2. In the Settings window for **Circle**, locate the **Size and Shape** section.
3. In the **Radius** text field, type 0.000018.
4. Locate the **Position** section.
5. In **X** text field type -0.000079.
6. In **Y** text field type 0.000258.
7. Locate the **Position** section. From the **Base** list, choose **Center**.

Repeat these steps till you construct 15 circles taking in consideration the spacing between each circle with is $79 \mu\text{m}$.

Rectangle 1

1. Right-click **Component 1> Geometry 1** and choose **Rectangle**.
2. In the Settings window for **Rectangle**, locate the **Size and Shape** section.

3. In the **Width** text field, type 0.02.
4. In the **Height** text field, type 0.02.
5. Locate the **Position** section.
6. In **X** text field type - 0.01.
7. Locate the **Position** section. From the **Base** list, choose **Center**.

Rectangle 2

1. Right-click **Component 1> Geometry 1** and choose **Rectangle**.
2. In the Settings window for **Rectangle**, locate the **Size and Shape** section.
3. In the **Width** text field, type 0.0012.
4. In the **Height** text field, type 0.00017.
5. Locate the **Position** section.
6. In **X** text field type -0.0006.
7. Locate the **Position** section. From the **Base** list, choose **Center**.
8. Click the **Build All Objects** button.

Difference 1

1. Right-click **Component 1> Geometry 1> Booleans and partitions** and choose **Difference**.
2. In the Settings window for **Difference**, locate the **Difference** section.
3. In **Objects to add** field select **Rectangle 1**.
4. In **Objects to subtract** field select **Rectangle 2** and select **Circle 1** to **Circle 15**.
5. Click the **Build All Objects** button.

After the last step, the setup should look like Figure A.4.

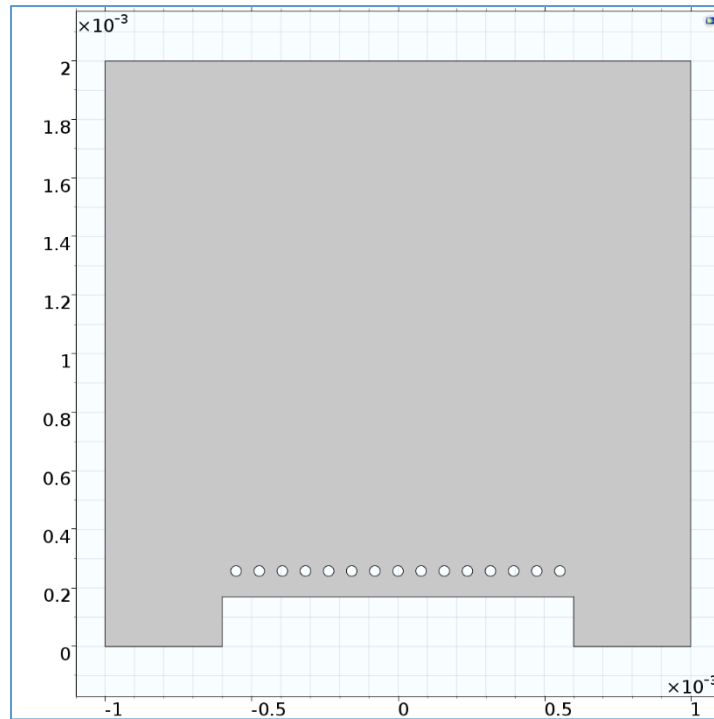


Figure A.4: Electro spray setup with 2 mm x 2 mm calculation domain.

Definitions

Explicit 1

1. On the **Definitions** toolbar, click **Explicit**.
2. In the Settings window for **Explicit 1**, locate the **label** text field and type Air Domain.
3. In **Geometric entity level** section, select **Domain** from the menu then click on **Rectangle 1** in the graphics window only.

Explicit 2

1. On the **Definitions** toolbar, click **Explicit**.
2. In the Settings window for **Explicit 2**, locate the **label** text field and type Mesh.

3. In **Geometric entity level** section, select **Boundary** from the menu then click on **Circle 1 to Circle 15** in the graphics window only.

Explicit 3

1. On the **Definitions** toolbar, click **Explicit**.
2. In the Settings window for **Explicit 3**, locate the **label** text field and type Substrate.
3. In **Geometric entity level** section, select **Domain** from the menu then click on **Rectangle 2** in the graphics window only.

Electrostatics

Ground 1

1. On **Physics** toolbar, click **Boundaries** and choose **Ground**.
2. Select boundary 5 only (the substrate).

Electric Potential 1

1. On **Physics** toolbar, click **Boundaries** and choose **Electric Potential**.
2. In **Model Builder** window, under **Component 1 > Electrostatic (es) > Electric Potential 1** select Boundary 5.
3. Locate the **Electric Potential** section.
4. In **Electric Potential** text field type 10000.

Electric Potential 2

1. On **Physics** toolbar, click **Boundaries** and choose **Electric Potential**.
2. In **Model Builder** window, under **Component 1 > Electrostatic (es) > Electric Potential 2** select **Circle 1 to Circle 256**.
3. Locate the **Electric Potential** section.

4. In **Electric Potential** text field type 2000.

Particle Tracing for Fluid Flow

1. Right-click on **Component 1 > Add Physics**.
2. In the **Add Physics** window, click on **Fluid Flow > Particle Tracing > Particle Tracing for Fluid Flow (ftp)**.
3. Locate the **Physics interfaces in study** and select **Study 2** only.
4. In **Model Builder** window, under **Component 1 > Particle Tracing for Fluid Flow (ftp)**, locate the Domain Selection section.
5. Select Boundary 1 only (the Air Domain).
6. Locate the Equation section in the settings window of the **Particle Tracing for Fluid Flow (ftp)**. From **Equation form** menu, select the **Time dependent**.
7. Locate the **Formulation** section and select **Newtonian**.
8. Locate the **Wall accuracy order** section and select **2**.
9. Locate the **Arguments for random number generation** section and select **Generate unique arguments**.
10. Locate the **Advanced Settings** and select **Include rarefaction effects**
11. Locate the **Maximum number of secondary particles** and type 0 in the text field.
12. In **Component 1 > Particle Tracing for Fluid Flow (ftp)**, click on **Wall**.
13. In **Wall** settings window, locate **Wall conditions** section.
14. In **Wall conditions** menu, select **Freeze**.
15. In **Component 1 > Particle Tracing for Fluid Flow (ftp)**, click on **Particle Properties 1**.
16. In **Particle Properties 1** settings window, locate the **Particle property** section.

17. In **Particle property** section, locate the **Particle property specification** menu and select **Specify particle mass and diameter**.
18. Locate the **Particle mass** text field and type m0.
19. Locate the **Particle diameter** text field and type d0.
20. In the **Particle type** menu, select **Solid particles**.
21. Locate the **Charge Number** section.
22. In **Charge number** text field type 230.

Inlet 1

1. Right-click on **Component 1 > Particle Tracing for Fluid Flow (ftp)** and select **Inlet**.
2. In **Component 1 > Particle Tracing for Fluid Flow (ftp) > Inlet 1**, locate the **Boundary Selection** section and select Boundary 3 only.
3. Locate the **Initial Position** section.
4. In **Initial Position** section, select **Uniform distribution**.
5. In the same section, type 10000 in the **Number of particles per release** text field.
6. Locate the **Initial Velocity** section, and select Expression from the **Initial velocity** menu.
7. In the same section, choose **User defined** in the **Velocity field** menu and type $-v0$ in **y** text field.

Outlet 1

1. Right-click on **Component 1 > Particle Tracing for Fluid Flow (ftp)** and select **Outlet**.
2. In **Component 1 > Particle Tracing for Fluid Flow (ftp) > Outlet 1**, locate the **Boundary Selection** section and select Boundary 5 only.
3. In the **Outlet** settings window, locate the **Outlet** section.
4. Select **Freeze**.

Electric Force 1

1. Right-click on **Component 1 > Particle Tracing for Fluid Flow (ftp) > Forces** and select **Electric Force**.
2. In **Electric Force 1** settings window, locate the **Domain Selection**.
3. Select Boundary 1 only.
4. Locate the **Electric Force** section. From the **Specify force using** menu, select **Electric potential**.
5. In the same section, select the **Electric potential (es)** from the **Electric potential** menu.
6. Locate the **Advanced Settings** section and check the **Use piecewise polynomial recovery on field**.

Drag Force 1

1. Right-click on **Component 1 > Particle Tracing for Fluid Flow (ftp) > Forces** and select **Drag Force**.
2. In **Drag Force 1** settings window, locate the **Domain Selection**.
3. Select Boundary 1 only.
4. Locate the **Drag Force** section and select **Stokes** from **Drag law** menu.
5. In the same section, in **Velocity field** menu select **user defined** and type $-v0$ in **y** text field.
6. Locate the **Rarefaction Effects** section. From the **Rarefaction effects** menu select **Cunningham-Millikan-Davies**.
7. In the same section and from the **Mean free path calculation** select **Ideal gas, hard sphere collisions**.

8. In the same section make the CMD coefficients C_1 , C_2 , and C_3 equal to 1.142, 0.558, 0.999 respectively.

Particle-Particle Interaction 1

1. Right-click on **Component 1 > Particle Tracing for Fluid Flow (ftp) > Forces** and select **Drag Force**.
2. In **Drag Force 1** settings window, locate the **Domain Selection**.
3. Select Boundary 1 only.
4. Locate the **Force** section, then from the **Interaction force** menu select **Coulomb**.
5. Locate the Advanced Settings section and check the Exclude Jacobian contribution for particle-particle interaction.

Brownian Force 1

1. Right-click on **Component 1 > Particle Tracing for Fluid Flow (ftp) > Forces** and select **Brownian force**.
2. In **Drag Force 1** settings window, locate the **Domain Selection**.
3. Select Boundary 1 only.

Mesh 1

1. In **Model Builder** window, under **Component 1** right-click **Mesh 1**.
2. In **Mesh 1** setting window, locate the **Mesh Settings** section.
3. In **Element size** menu choose **Extremely fine**.

4. Click **Build All** button. (See Fig. A.5 below).

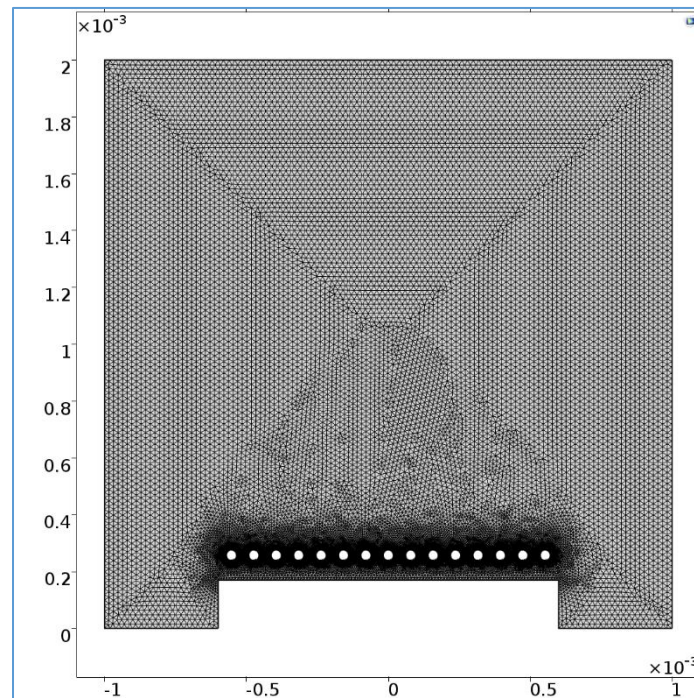


Figure A.5: Meshing the calculation domain.

Study 1

1. In **Model Builder** window, under **Component 1 > Study 1 > Step 1 Stationary** uncheck the **Particle Tracing for Fluid Flow (ftp)** in the **Physics and Variables Selection** section.
2. Click the **Compute** button.

Study 2

1. In **Model Builder** window, under **Component 1 > Study 1 > Step 1 Stationary** uncheck the **Electrostatics (es)** in the **Physics and Variables Selection** section.
2. Locate the Values of Dependent Variables section and adjust the settings as the following

Values of Dependent Variables

Initial values of variables solved for

Settings: User controlled

Method: Initial expression

Study: Zero solution

Values of variables not solved for

Settings: User controlled

Method: Solution

Study: Study 1, Stationary

Selection: Automatic

Store fields in output

Settings: All

3. Locate the Study Settings section, then from the Time unit menu select μs .
4. In the **Time** text field type range (0,150/169,150) or click on the range button then from **Entry method** menu select **Number of values** and set the **Start** 0, **Stop** 150, and the **Number of values** 170 then click **Replace**.
5. Click the **Compute** button.

Results

Next, add a contour plot showing the electric potential.

1. In the **Model Builder** window, under **Results** right-click **Electric Potential (ec)** and choose **Surface 1**.
2. In the setting window of the **Contour**, click **Expression** in the upper-right corner of the **Expression** section. From the menu choose **Component 1 > Electrostatics > Electric > es.normE – Electric field norm**.
3. Locate the **Coloring and Style** section. From the **Color table** list, choose **GrayPrint**.
4. Clear the **Color legend** check box.
5. Select the **Reverse color table** check box.

6. In the **Model Builder** window, under **Results** right-click **Electric Potential (ec)** and choose **Streamline**.
7. In the setting window of the **Streamline**, click **Expression** in the upper-right corner of the **Expression** section. From the menu choose **Component 1 > Electrostatics > Electric > es.Ex, es.Ey – Electric Field**.
8. Locate the **Streamline Positioning** section. From the **Positioning** list, choose **Uniform Density**.
9. Locate the **Coloring and Style** section. From Separating distance text field type 0.0008.
10. From the **Line type** menu choose **Line** and from the **Color table** list, choose **Blue**.
11. Click **Plot** button.
12. In the **Model Builder** window, under **Results > Data Sets** right-click on **Particle 2** and select **Duplicate**.
13. In the **Model Builder** window, under **Results > Data Sets** right-click on **Derived Values** and select **Global Evaluation**.
14. In **Global Evaluation 1** settings window, locate **Expression** section and select the **Total number of particles in selection** as the picture below.

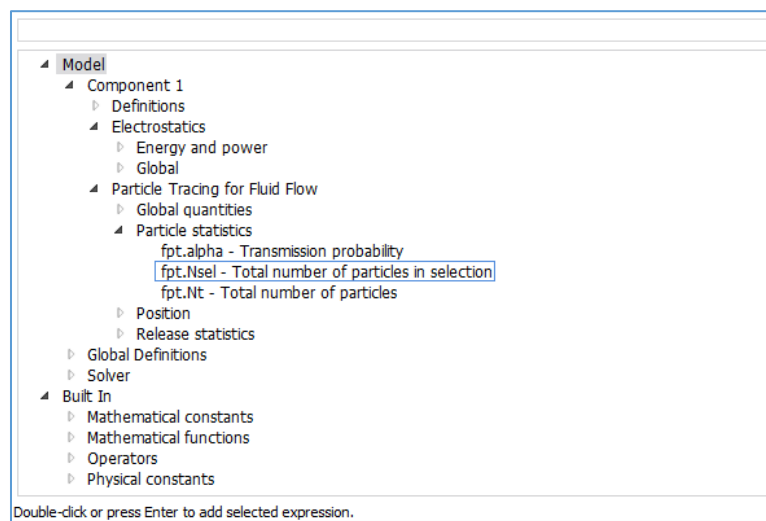


Figure A.6: Particle counting settings.

15. In the **Global Evaluation 1** settings window, locate the **Data** section, then from the **Data set** menu select **Particle 2**

16. Click **Evaluate** button

The results in Table 1 indicate the total number of particles deposited on the substrate.

17. In the **Model Builder** window, under **Results > Data Sets** right-click on **Derived Values** and select **Global Evaluation**.

18. In **Global Evaluation 2** settings window, locate **Expression** section and select the **Total number of particles in selection** as shown in Figure A.6.

19. In the **Global Evaluation 2** settings window, locate the **Data** section, then from the **Data set** menu select **Particle 3**.

20. Click **Evaluate** button.

The results in Table 2 represent the total number of particles deposited on the mesh.

Particle Trajectories (fpt)

1. In the **Model Builder** window, under **Results** select **Particle Trajectories**.
2. In the **Particle Trajectories** settings window, locate the **Data** section in which choose from **Data set** menu **Particle 1**.
3. In the same section choose from **Time (μs)** menu **180**.
4. Locate the **Color Legend** section and check the **Show legends**.
5. In the **Model Builder** window, under **Results > Particle Trajectories** select **Particle Trajectories 1**.
6. In **Particle Trajectories 1** settings window, locate **Coloring and Style** section.
7. In **Coloring and Style** section, locate the **Type** menu and select **Point**.

8. In the same section, locate the **Point radius expression** text field and type 0.003.
9. In the same section, check the **Radius scale factor** and type 0.002.
10. Click **Plot** button.

The results should look like Figure A.7.

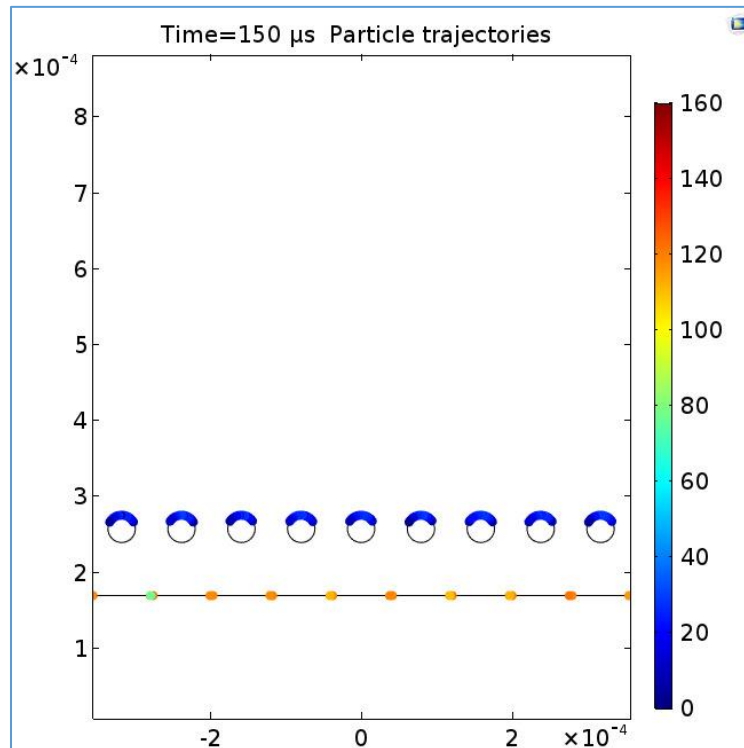


Figure A.7: The particle trajectory of 70 μm mesh gap at 150 μs calculation time.

Appendix B: Vita

108 E. Grace St. /Apt 201 • Richmond, VA 23219 • (804) 501-6874 • Email:

almilajkn@mymail.vcu.edu

LinkedIn: www.linkedin.com/in/karamalmilaji

Education:

Master of Mechanical and Nuclear Engineering August 2016
Virginia Commonwealth University, Richmond, VA GPA 3.85

Bachelor of Refrigeration and Air Conditioning Engineering July 2007
Technical College of Mosul, Iraq
Graduated first in class of 57

Presentations: Fabricating Superoleophobic and Superhydrophobic Surfaces with Multi-Roughness
Using Airbrush and Electrospray.
Virginia Soft Matter Workshop/ University of Virginia Nov 14, 2015

Qualification/Technical Proficiencies:

- Analytical and creative thinking
- Project planning and management
- Solid engineering background
- 8 years of experience in Refrigeration and Air Conditioning Engineering
- Self-motivated and ability to multi-task, working under pressure to strict deadlines
- Ability to use Microsoft suit, MATLAB, AutoCAD, and COMSOL.

Relevant Experience: Ability to use SEM, AFM, LSM, Goniometer, Profilometer, and Rheometer

Language Skills: Fluent in Arabic and English

Relevant Coursework: Thermodynamics, Heat Transfer, Fluid Mechanics, Refrigeration and Air Conditioning, Electrical and Electronic Engineering, Mechanical Design, Drawing of Refrigeration and Air Conditioning systems, Steam Engineering, Refrigeration Systems, Air Conditioning Systems, Renewable Energy, Control Circuits.

Professional Experience:

Maintenance Engineer of Air Conditioning Systems at Oil Distribution Company.

Nov 2010 – Dec 2013

- Installed and maintained domestic refrigeration and air conditioning systems e.g., split unit and window type air conditioners, water coolers, and refrigerators.

Maintenance Engineer of HVAC Systems at Midland Refineries Company (MRC).

Feb 2008 – Nov 2010

- Installed and maintained all types of air conditioning e.g., VRF systems, air and water Chillers, air handling units, package systems, split units, and window type units.

Achievements: Installation of two VRF units type FUJITSU for two distillation units in MRC.

Activities: Member in ASHRAE student chapter

Dec 2014 – Present